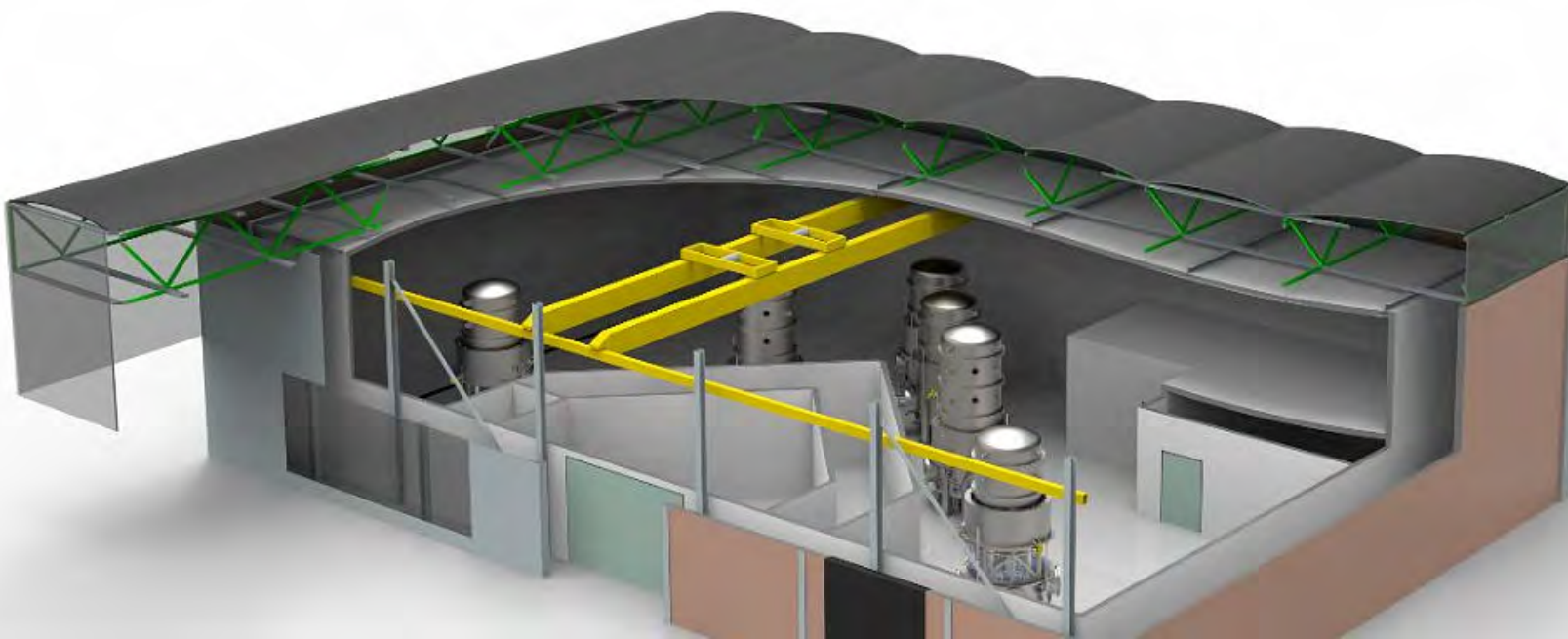


ETpathfinder

DESIGN REPORT

The ETpathfinder Team*

*Nikhef, Maastricht University, University of Antwerp, Ghent University,
Katholieke Universiteit Leuven, Université Catholique de Louvain, Hasselt
University, Vrije Universiteit Brussel, Fraunhofer Institute for Laser Technology,
RWTH Aachen, University of Twente, Eindhoven University of Technology,
Liege Université, VITO, TNO.



This is the public version of the ETpathfinder design document. In order to be complaint with certain legal aspects, such as for instance European tendering rules, in this version of the document 3 appendices on project management details ('Detailed Budget', 'Timelines', 'Required Person Power') are removed. We apologies to the reader for any broken links present in the document resulting from this.

ETPATHFINDER TEAM
URL: www.ETpathfinder.eu
Contact: s.hild@nikhef.nl

24th of January 2020



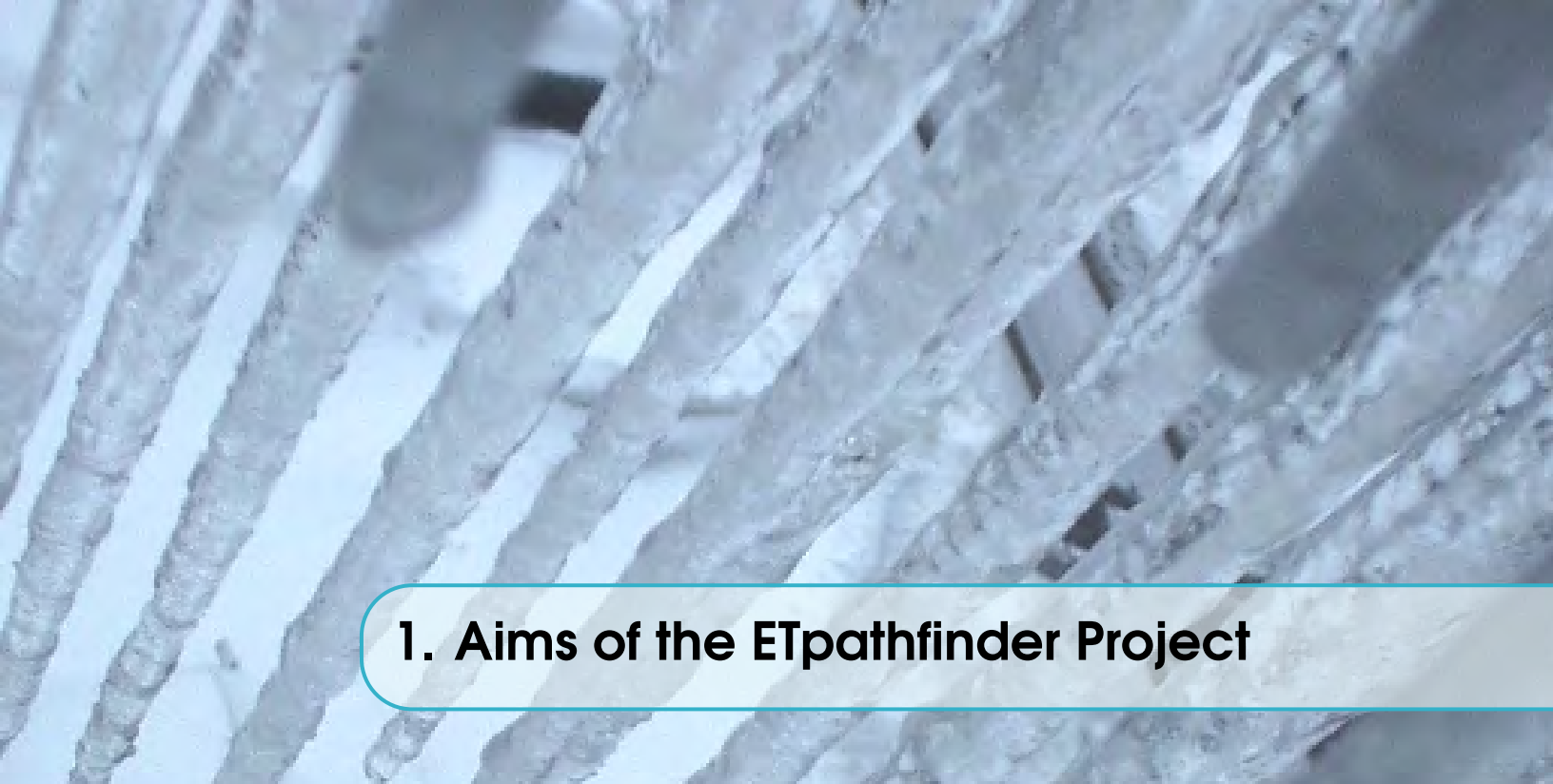
Contents

1	Aims of the ETPathfinder Project	7
1.1	Top-Level Research Goals of ETPathfinder	7
1.2	ETPathfinder Stages and Timeline	8
1.2.1	Phase 1	8
1.2.2	Phase 2	10
1.2.3	R&D beyond initial ET	10
1.3	Workpackages of ETPathfinder	10
1.4	How to Read This Document	10
2	Hall Requirements	13
2.1	Introduction	13
2.2	Floorplan	13
2.2.1	Routes for Equipment into the ETPathfinder Cleanroom	14
2.3	Foundation and Floors	15
2.4	Technical Specifications	16
2.5	Budget	16
3	WP3: Cleanroom	17
3.1	Layout of the clean room	17
3.1.1	Outer structure	17
3.1.2	Crane	18

3.1.3	Experiment area	18
3.1.4	Cleaning area	19
3.1.5	Space for noisy equipment	19
3.1.6	Services	19
3.1.7	Access	20
3.2	Specification summary	21
3.3	Work Break Down Structure of the cleanroom WP	21
4	WP4: Vacuum and Cryogenics	23
4.1	Overview of the Vacuum and Cryogenics WP	23
4.2	System requirements	24
4.2.1	Vacuum requirements	24
4.2.2	Requirements on the cryogenic system	28
4.3	Vacuum and Cryogenic Design	29
4.3.1	Model calculations	29
4.3.2	Vacuum System	31
4.3.3	Cryogenics	39
4.3.4	Thermal links	52
4.3.5	Initial Cool-down calculations	55
4.4	Work Break Down Structure of the vacuum and cryogenics WP	60
4.5	Detailed Budget for the vacuum and cryogenics WP	61
5	WP5: Seismic Isolation	63
5.1	Overview	63
5.2	Technology background	63
5.2.1	Inverted pendulum	65
5.2.2	Geometric anti-spring (GAS) filters	67
5.3	Seismic isolation for the arm-cavity mirrors	69
5.3.1	Mechanics: pre-isolation platform	69
5.3.2	Mechanics: seismic attenuator	71
5.3.3	Passive seismic attenuation performance	74
5.3.4	Controls	74
5.4	Cryogenic payload	77
5.4.1	123 K payload	77
5.4.2	Controls	79
5.4.3	10 K payload development	81
5.5	Seismic isolation for the optical benches	84
5.5.1	Mechanics	84
5.5.2	Controls	84
5.5.3	Table-top suspensions	87

5.6	WP5 risk mitigation strategy	87
5.7	WP5 work breakdown structure	88
5.8	WP5 budget	88
6	WP6: Optics	89
6.1	Overview of the Optics WP	89
6.2	Pre-stabilized Laser	90
6.3	Input and Output Optics	90
6.3.1	Injection Optics	91
6.3.2	Input Mode-Cleaner	92
6.3.3	In-Vacuum Modulation Bench	93
6.3.4	Detection Bench and Output Mode Cleaner	93
6.4	Main Interferometers	93
6.4.1	Main Mirror Substrates	93
6.4.2	Main Mirror Coatings	99
6.4.3	Coating Uniformity	102
6.5	Novel Mirror Coating Development	102
6.5.1	Main Activities	102
6.5.2	Infrastructure components	106
6.5.3	Experimental setup	114
6.6	ETpathfinder Auxiliary Optics and related Infrastructure	114
6.6.1	Optical Tables	114
6.6.2	Clean Workspaces	114
6.6.3	Viewports	114
7	WP7: Controls	117
7.1	Overview of the Control WP	117
7.2	Introduction	117
7.3	Control system components and requirements	117
7.3.1	Control loop hierarchy	117
7.3.2	Local control	119
7.3.3	Global control	120
7.3.4	Intermezzo: Photodiode demodulation	120
7.3.5	Fast dedicated loops	122
7.3.6	Real-time communication	122
7.3.7	Timing and local oscillator distribution	122
7.3.8	Slow control and automation	123
7.3.9	Safety systems	123
7.3.10	Interfacing with other hardware	124
7.3.11	List of control loops	124

7.4	Implementation details	126
7.4.1	Choice of control ecosystem	126
7.4.2	Timing and local oscillator distribution	127
7.4.3	Control and DAQ room	127
7.4.4	Suspension transducers	128
7.4.5	Environmental probes and actuators	128
7.4.6	Photodiodes and quadrant photodiodes	129
7.4.7	Small suspensions	129
7.4.8	Beam monitoring cameras	130
7.4.9	Racks	130
7.4.10	Cabling	130
7.5	Interfaces	131
7.6	Planning and Work Break Down structure	131
8	Budget Summary	133
9	Health and Safety	135
9.1	Health and Safety Overview for ETpathfinder	135
10	Organisational Overview of ETpathfinder	137
	Bibliography	138
	Nomenclature	145



1. Aims of the ETPathfinder Project

1.1 Top-Level Research Goals of ETPathfinder

The designs suggested for third generation (3G) laser-interferometric gravitational wave (GW) observatories differ in several aspects and technologies strongly from the currently operating GW detectors Advanced LIGO, Advanced Virgo and KAGRA. Advanced Virgo and Advanced LIGO operate based on fused silica mirrors at room temperature and a laser wavelength of 1064 nm. KAGRA (sometimes referred to as detector of generation 2.5) operates with cryogenic, sapphire mirrors, which allows to stay at 1064 nm laser wavelength. In contrast, both the Einstein Telescope (ET) and Cosmic Explorer (CE) plan to operate cryogenic mirrors made from silicon and read out by lasers with wavelength further into the infrared (about 1550 nm to about 2100 nm).¹

In order to inform and de-risk the design efforts for 3G detectors, and to develop, test and qualify their technologies, new test facilities are required, providing an ultra-low noise test bed in a 3G-like environment. ETPathfinder strives to serve this purpose. It will provide a new facility to *holistically prototype* the following aspects:

- **New Temperature, i.e. Cryogenics:** Cryogenic temperature of the main test masses (120 K and 15 K); low-noise cryo-coolers, decoupling of cryo-coolers from test masses while providing sufficient cooling power, cryo-shields etc;
- **New Mirror Material, i.e. Silicon:** Changing from fused silica (amorphous material, electrically insulating) to silicon (crystalline semi-conductor) will be a major change with many implications for optical aspects, polishing, coatings etc as well as mechanical aspects.
- **New Wavelength, i.e. 1550 - 2100 nm:** Moving to silicon as test mass material requires to go to longer laser wavelength to reduce optical absorption. Lasers, optical and electro-optical components (such as high-efficiency photo detectors) need to be developed and qualified for GW detector relevant aspects. Laser stabilisation loops (power, frequency, jitter, etc) need to

¹The desire to go to cryogenic operating temperature is driven by reduced Brownian noise in the mirrors, their coatings and the suspensions. Fused silica has been found to have a high mechanical loss at low temperatures and is therefore not a suitable material for cryogenic operation. Silicon offers a promising alternative, but requires a change of the laser wavelength to minimise optical absorption in the substrate and associated noise and heating effects.

be developed.

- **Advanced Quantum Noise Reduction Techniques:** Innovative QND schemes have been suggested to realise the ambitious low-frequency sensitivity goals of 3G observatories. These need to be tested in conjunction with the points above.

All four of these strands are interlinked and ultimately need to be tested altogether in the same system AND at displacement sensitivity not too dissimilar to a the Einstein Telescope. Note that we expect (and actually rely on) that many individual aspects (e.g. optical parameters of a new coating, cooling down of a mirror blank, laser stabilisation at 1550 nm etc) will be tested in table top experiments or small cryostats around the world. **The task for ETPathfinder is to scale everything up to 3G dimensions and sensitivity levels in order to a) demonstrate the benefit of the new technologies and their compatibility with the targeted 3G sensitivity and b) develop these techniques at systems level with all their cross-compatibility requirements.**

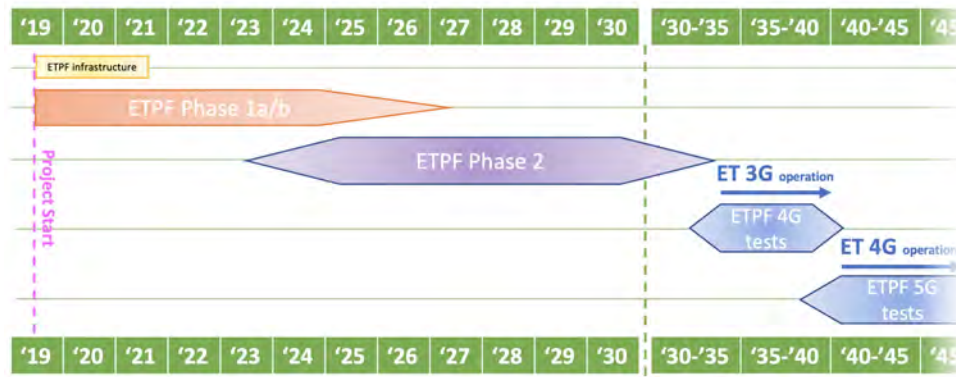


Figure 1.1: Rough overview of the estimated ETPathfinder timelines. The yellow box 'ETPF infrastructure' indicates the target for completion of the hall reconstruction, the cleanroom construction and the installation of the vacuum systems. After completion of Phase 1 and Phase 2 (see description in text), it is anticipated that while ET is running in observation mode with generation X technology, ETPathfinder will contribute to prototyping generation X + 1 technologies. (Note: There is no official timeline yet for ET observation runs. So the shown observation periods are for illustration only.)

1.2 ETPathfinder Stages and Timeline

ETPathfinder is planned to have several staged development periods. These are referred to as:

1.2.1 Phase 1

In order to explore the full temperature (120 K vs 15 K) and wavelength (1550 nm vs about 2000 nm) matrix, covering the parameter space currently suggested for 3G observatories (i.e. ET and CE), we will set up two separate Fabry-Perot Michelson interferometers using small sized mirrors (i.e. 15 cm diameter, weight of 3 kg). Two independent laser, injection and detection systems for 1550 nm and about 2 micrometer wavelengths will be designed and constructed. Phase 1 will be completed around 2025.

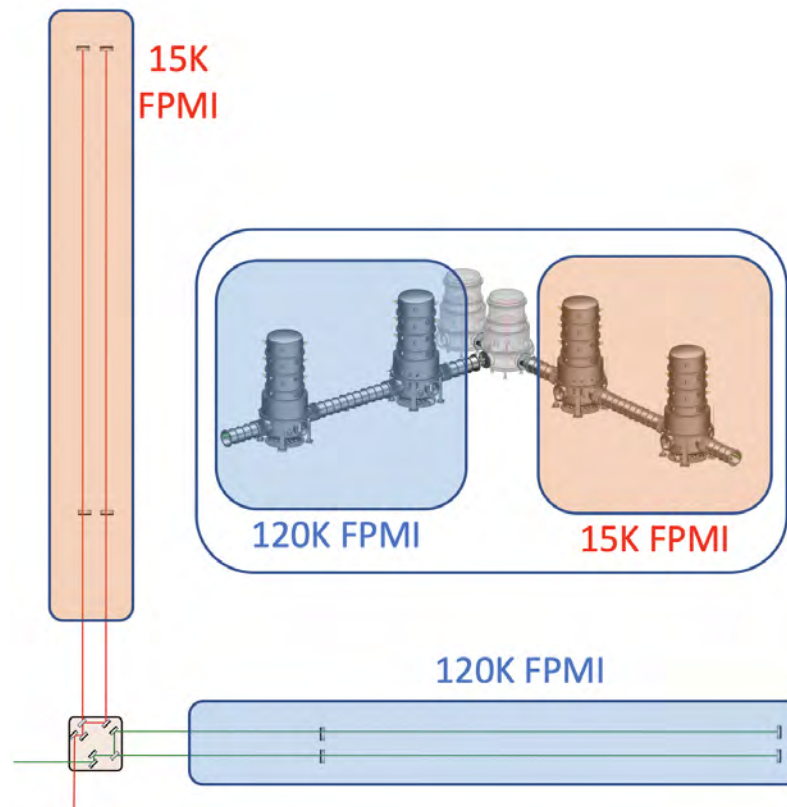


Figure 1.2: Simplified sketch of the ETpathfinder Phase 1. The cryostats will hold each 2 main test masses and hence allow for the construction of two separate Fabry-Perot Michelson (FPMI) interferometers. If one choose to arrange these 2 FPMI not in L-shape, but with parallel arms, then it is possible to install two independent FPMI, i.e. one FPMI per arm. This will allow us to run in parallel 2 FPMI with different test mass temperature (120 K and 15 K) and laser wavelengths (1550 nm and around 2 micrometers).

1.2.2 Phase 2

Based on the outcomes from Phase 1, in Phase 2 we will down-select to a single operating temperature and laser wavelength and build up a Fabry-Perot Michelson interferometer with ET-like testmasses, i.e. diameter of 35 to 45 cm with a mass of the order 10^2 kg. Phase 2 will be completed around 2028-2030 in order to help informing the final design of the initial ET configuration.

1.2.3 R&D beyond initial ET

Once Phase 2 has been completed and hardware for the initial ET is produced and installed, ETpathfinder can start to investigate upgrades to ET to be installed after a few years of observation with the initial configuration. Note, that the timelines indicated in Fig.1.1 are just for illustration and will be adopted over the coming years to match the ET timelines once these becomes clearer. Obviously, it is too early right now to speculate about the relevant technologies and concepts to be tested. However, we believe that the ETpathfinder infrastructure (e.g. vacuum system, cryostats, cooling infrastructure etc) is designed in a way to give sufficient flexibility and is compatible with a wide range of future concepts and technologies.

1.3 Workpackages of ETpathfinder

In this document the chapters follow the same structure as the work packages stated in the ETpathfinder Interreg proposal:

- WP3: Cleanroom
- WP4: Vacuum and Cryogenics
- WP5: Seismic Isolation
- WP6: Optics
- WP7: Controls

In addition in Chapter 2 a brief overview is given of the construction and refurbishment of the hall that will house the ETpathfinder clean room. Note that the costs for the hall are covered by Maastricht University via a separate budget and are outside the 14.5 million Euro covered by the Interreg grant. At the end of this document we will give a brief summary of the overall budget and we conclude this document with a general outline on the Health and Safety philosophy for ETpathfinder.

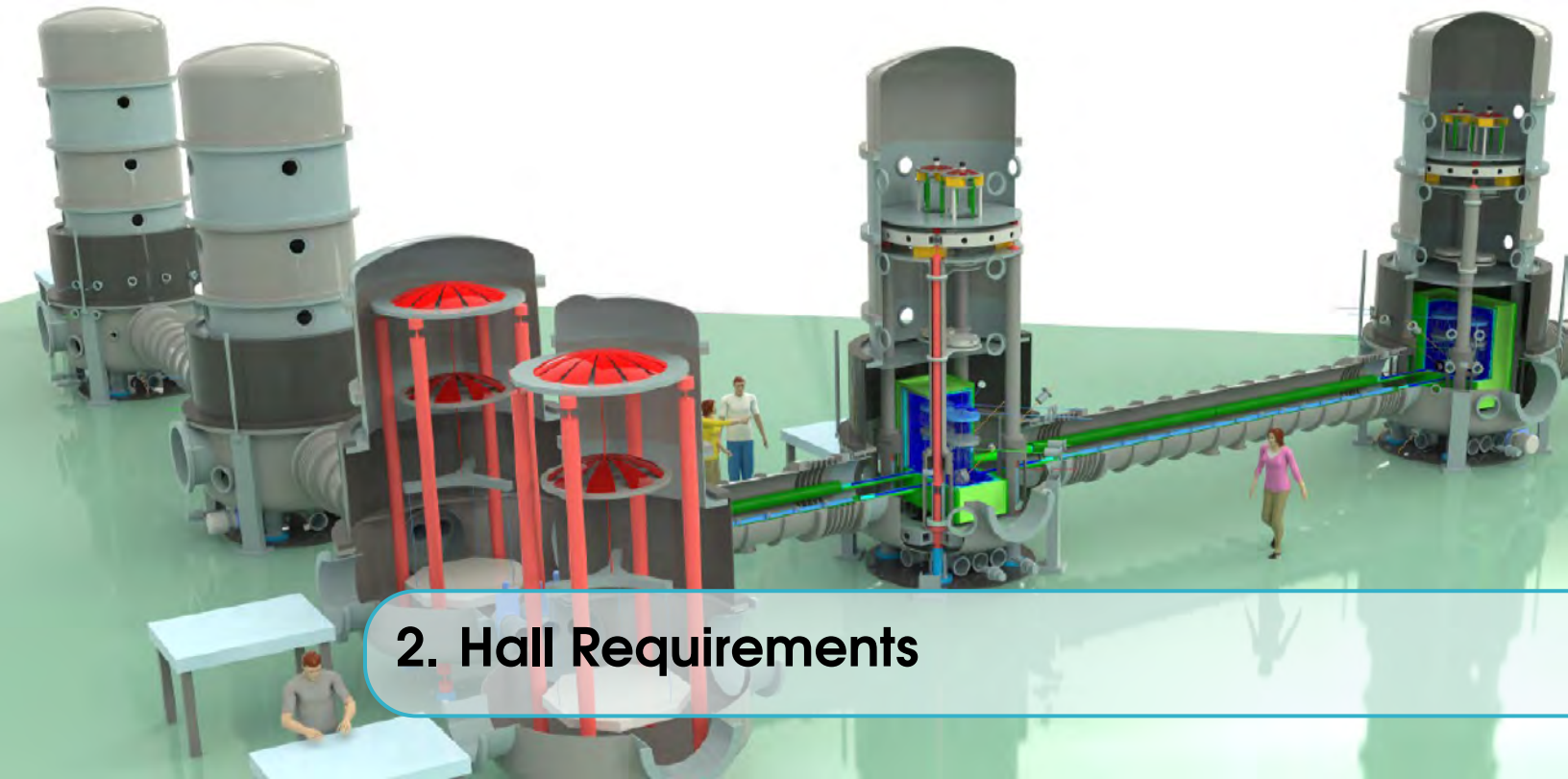
1.4 How to Read This Document

The currently awarded Interreg grant provides capital funding of 14.5 million Euros (consisting of contributions from ERDF, the Dutch Government, the Flemish Government, several Dutch and Belgian provinces, and co-funding from the ETpathfinder partner institutions) is supposed to directly cover the implementation of infrastructure for Phase 1.² As ETpathfinder is aimed to become a long-term R&D infrastructure, we should make sure right from the beginning that high-price tag items, such as the hall itself, the cleanroom, the vacuum systems etc are compatible (or up-gradable with moderate funds) to host *Phase 2* and *R&D beyond initial ET* and hence enable an operation time far beyond the initially funded 3 years.

²Note that the 14.5 million Euros of the Interreg grant can only cover capital investment (i.e. equipment) and does not include any labor or running costs. All personnel for ETpathfinder activities (including design, construction, installation and commissioning of ETpathfinder) has to be contributed by the 15 ETpathfinder partner institutions.

As a consequence of this and also taking into account the current stage of the project, the reader will find the workpackage descriptions in this design document to differ in terms of level of detail and maturity. In general the ETpathfinder team has focussed its attention so far mainly on all subsystems and items with big cost (i.e. 'you have to get it right the first time'), long lead times and which sit on or close to the critical path. The designs of such items are well developed and often go beyond a conceptual design level. Examples in this category include the cleanroom, the vacuum system and parts of the seismic isolation and the cryogenic infrastructure.

On the other end of the spectrum there are subsystems and items requiring less innovation and are of lower cost, shorter delivery time and which are further down the project timeline. Those items and subsystems are far less developed at this stage of the project and they are currently not even close to the conceptual design stage. These include for instance parts of the optical configuration, the optical layout, interferometer control and some mechanical aspects such as the small suspensions used on the in-vacuum tables. It should however be noted that all these less developed topics focus on existing technologies and we assume no or very little development is need to implement them in ETpathfinder. For instance for the optical configuration we assume to start with simple Fabry-Perot Michelson interferometers without any recycling techniques. This is a fairly simple and well studied configuration and for which much experience exists in the GW community. As another example, for the small suspensions of auxiliary optics, we assume to adopt existing suspension designs (e.g. AEI-10m, LIGO tip-tilt, ERC speedmeter etc) to the ETpathfinder needs.



2. Hall Requirements

2.1 Introduction

ETpathfinder will be situated in an existing hall of a University owned building (Dubiosdomein 30) in Maastricht. The rough dimensions of the inside of the hall are 37 m by 25 m and with a clear height of 8 m.

2.2 Floorplan

The hall will need to provide various functional spaces which are detailed in Fig. 2.1:

- A central clean room area for the hosting the ETpathfinder vacuum system, the main optical benches and systems, space for preassembly of subsystem components etc. (red). This area will sit on its own reinforced floor, which is separated by a cut from the other areas of the floor and hence the red floor area will be decoupled from the walls of the hall and the walls of the cleanroom itself;
- Enclosed spaces for noisy equipment, such as pulse tube coolers or vacuum pumps (green);
- Changing room and cleanroom locks for personnel to enter and leave the ETpathfinder cleanroom (orange);
- Cleaning facilities including large ultrasonic bath, ovens, flow-boxes, storage of cleaned parts etc (yellow area in the lower right corner); heavy goods lock for transferring big and heavy items, such as the vacuum system parts, into the cleanroom (yellow area in the middle of the left side);
- Service area: Between the outside wall of the cleanroom and the outside wall of the hall there will be a service corridor of about 1.7 m width (blue). Relevant services include air conditioning, electric power distribution, safety and security. The ground level of this 8 m high corridor should stay mostly free to allow access to the aforementioned services, but also to serve as escape route. In addition in this corridor will be used for installation of the mechanical support structure (20 cm away from the edge of the outer floor) for the cleanroom roof and the rails for the crane which will be inside the cleanroom (see also Fig. 3.1).

In addition there will be an control room for ETpathfinder (not shown in Fig. 2.1), but adjacent to the ETpathfinder hall in the existing printing hall. Also we plan to have a visitor gallery above the changing room and the cleaning facilities.

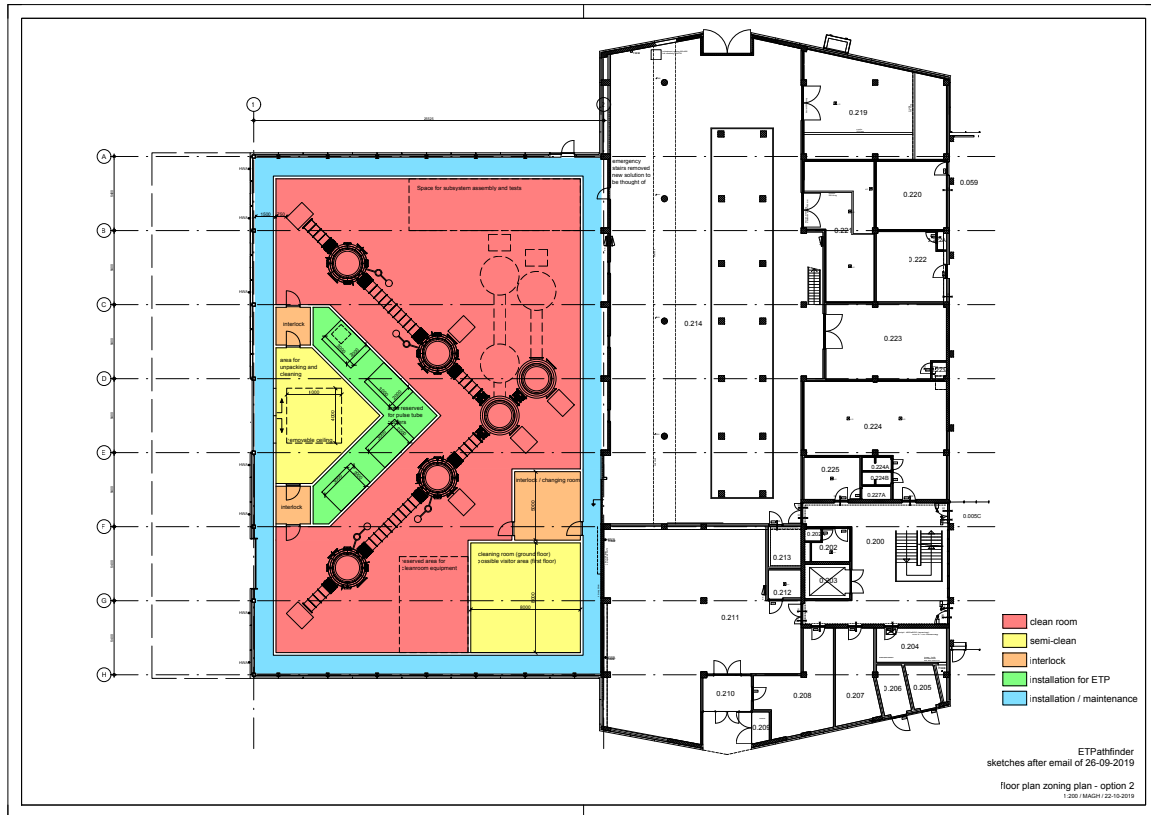


Figure 2.1: Overview of the floorplan of the ETpathfinder hall. The main cleanroom is shown in red, separately isolated space for noisy equipment (e.g. cryo-coolers and vacuum pumps) is shown green, changing rooms and cleanroom locks are shown in orange, semi-cleanrooms for cleaning of parts and transferring equipment are shown in yellow and the blue area surrounding the entire cleanroom is a service space containing for instance air ducts etc. The ETpathfinder vacuum system is indicated by black solid lines, while potential future extensions are indicated by dashed lines. The main route for humans and easily portable parts and materials is via old printing hall (right b/w building) and the service corridor into the cleaning facilities (yellow) and cleanroom lock (orange) on the lower right corner of the hall. All heavy parts and mayor equipment will enter via the equipment lock (yellow triangle on the left side of the hall). The top of the figure is roughly orientated towards North.

2.2.1 Routes for Equipment into the ETpathfinder Cleanroom

In order to allow the transfer of main equipment items of ETpathfinder (e.g. vacuum tanks etc) into the main ETpathfinder cleanroom, we decided on a 2-stage process in order to keep the overpressure in the cleanroom at all times. Equipment will arrive via lorry on the carpark west of the hall. The equipment will then loaded of via a hire mobile crane onto a thin heavy-duty sledge (design TBD) which allows to move the parts into the equipment lock (triangular yellow area on the left of Fig. 2.1). The heaviest parts will be tank bases with a bit over 3 m diameter, nearly 2 m height and a weight of

of the cleanroom to be separated from the outside walls of the hall, in order to decouple the floor from wind-induced vibrations and tilts of the floor. The proposed geometry of the cut in the floor corresponds to the red area in Fig. 2.1. This geometry will also ensure that the noisy equipment such as pulsetube coolers etc will sit on a different foundation than the main ETpathfinder vacuum system. The gap between adjacent concrete floor slabs should be about 2 cm wide with a rubber cover on top.

2.4 Technical Specifications

The main technical specifications of the ETpathfinder hall are driven by providing the space and required services for housing the ETpathfinder cleanroom:

- In the service corridor around the clean room the temperature extremes have to be decreased in order to reduce requirements on the thermal insulation of the cleanroom itself and to reduce the load on the aircondition system of the main cleanroom. So the space around the cleanroom will be held in the temperature range between 10 and 30°C.
- Humidity will not be controlled.
- Electrical power connectivity for at least 200 kW to run all of the ETpathfinder equipment (does not include air conditioning unit for the cleanroom).
- Chilled water power of 150 kW for cooling of pulsetube coolers, electronics racks etc (does not include air conditioning unit for the cleanroom)

Water chilling facilities and electric transformers etc are already available in adjacent parts of the ETpathfinder building (i.e. separate from the ETpathfinder hall). A clean air handling facility will be installed under the 7 m wide roof overhang towards the west side of the ETpathfinder hall. Also liquid nitrogen tanks (15 cubic meters capacity) will be installed adjacent to the hall.

2.5 Budget

The budget for the hall modifications detailed in this chapter are outside the 14.5 million Euros of the ETpathfinder Interreg budget and will be covered by University of Maastricht.



3. WP3: Cleanroom

3.1 Layout of the clean room

3.1.1 Outer structure

The outer structure provides a stable and clean working environment for the interferometer area and various other working spaces (see following sections). It also provides the infrastructure for the experiments, such as the distribution of power, Nitrogen and cooling water. The design of the clean room (placement of the walls, capacity of the air conditioning, feedthroughs, etc.) is strongly dependent on the cryogenics and vacuum design.

The clean room will be built inside the hall described in chapter 2. For a 3D sketch of the cleanroom configuration see Fig. 3.1. The inside of the cleanroom will cover an area of 22.0 m by

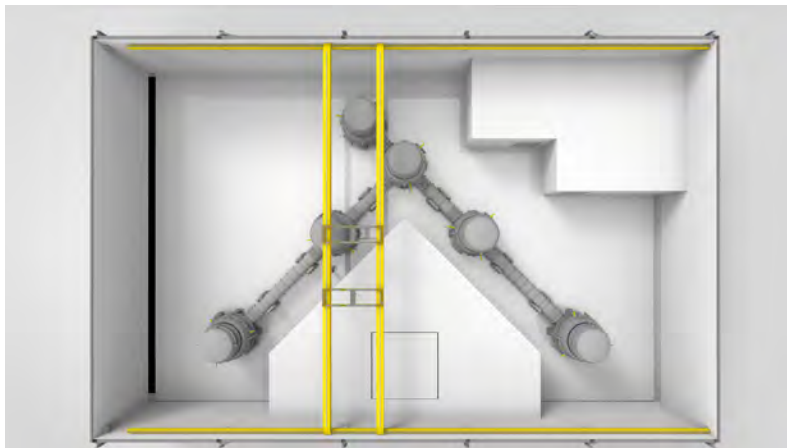


Figure 3.1: Overview of the cleanroom and the various compartments within it. The interferometer rests on a separate floor which is isolated from the building to avoid vibrations. The compartments and the crane are described in the text.

34.3 m at an height of about 8 m. The floor plan of the cleanroom is shown in Fig. 2.1. In the main clean room the full height of the clean room will be available. The semi-cleanrooms and the area for noisy equipment will be covered by a roof, separating them from the main cleanroom. The air flow through these compartments will be designed for a lower pressure than the main cleanroom to ensure nominal operating conditions in the main clean room at all times. See also section 2.

The outer wall of the cleanroom will be placed on the floor section connected to the outer wall of the building. The hall will provide the infrastructure (electricity, water) while the cleanroom will provide the temperature, humidity, cleanliness and internal infrastructure required for the experiments. Above the 8 m height of the clean room itself there is some space in between and below the curved roof of the hall for the air ducts of the air conditioning system. However, the hall itself has only a limited environmental control, e.g. the temperature can fluctuate between 10 °C and 30 °C and the humidity will be similar to outside conditions. The cleanroom walls will provide sufficient thermal insulation to guarantee the operational conditions inside the experiment area. There is a risk of condensation and water leakage from the gutter in the roof and therefore the roof of the clean room and the installation on top have to be made waterproof.

The roof of the cleanroom and its outer walls will be supported by external steel beams on the floor section connected to the building. These beams are located at 20 cm from the edge of the building floor section, leaving sufficient space for the walls. The weight of the roof, including lighting and filters is estimated at 100 kg/m². To allow for personnel on top of the roof the strength of the support is designed corresponding a maximum load of 150 kg/m² plus the weight of the crane and its maximum load.

As described in Chapter 2 the foundation of the central part of the floor is separated from the building. This part of the floor space in the hall will be used for the optical experiments. The floor section connected to the outer wall of the hall will be used for other activities. These areas are enclosed by internal walls to separate them from the experiment area.

3.1.2 Crane

Movement of large objects will be supported by a crane. The crane can move within the entire outer structure. Access to the loading area is possible through a hatch in the roof of that compartments, see section 3.1.7. The crane will be supported by rails attached to the metal beam supports that also support the wall and roof of the cleanroom. Because the full height of the cleanroom is required for setting up the towers the two pulleys and hooks of the crane will have to move in between the support beams. This crane must be able to lift a weight of 2000 kg per pulley, for a total load of 4000 kg. This will be sufficient to lift the largest components of the vacuum system. The two pulleys can be controlled separately as well as synchronously on order to be able level the vacuum parts during installation.

3.1.3 Experiment area

The main compartment of the clean room will house the interferometer. This compartment will be kept at over pressure with respect to the other compartments in order to maintain a maximally clean environment. In addition it is foreseen to do subsystem assembly and test in this area, see Figure 2.1. When working on the main optics it is foreseen to build a temporary enclosure (pop-up cleanroom) around the tower for an ultra clean environment for these rare occasions. This allows to keep the requirements for the large clean room relatively modest.

The experiment area will be ISO 14644-1 class 8¹ with at least 10 air changes/hr consisting of 10 % fresh air. The required temperature is $(20.0 \pm 1.0) ^\circ\text{C}$. The relative humidity must be $(50 \pm 15) \% \text{RH}$. The installation should be as quiet as possible since excessive noise may dominate the vibration noise of the laser bench or the injection bench. A sound insulating pop-up structure may be set up around a table in the rare occasions that acoustic noise is problematic.

It may be necessary to switch off the air conditioning system for a short time during experiments in order to minimize the acoustic noise during diagnostic measurements (quiet runs). Therefore the entire structure must be sufficiently air tight to maintain over pressure for at least 5 minutes when the air conditioning system is shut down. In addition, the users will be informed by an audible and visible alarm in case the specified temperature, humidity and over pressure are no longer maintained. The air locks and work procedures for bringing in or taking out equipment will ensure a stable environment under normal working conditions.

3.1.4 Cleaning area

The cleaning area, connected to the office building though an air lock will be used to clean and test small equipment before bringing it into the main experiment area. It will contain different sizes of ultrasonic cleaning baths and an oven for baking out as well as equipment for drying and wrapping cleaned parts. The air pressure in this compartment will not exceed that of the experimental area but the air flow will be sufficient to maintain ISO 14644-1 class 8 and proper working conditions.

3.1.5 Space for noisy equipment

All forepumps for the vacuum system are located outside the clean room in the space for noisy equipment, see Figure 4.7 and section 4.3. The electrical power and cooling water for these pumps will be connected through the walls of this compartment. Pulse tube coolers will also be placed here. The large diameter vacuum line connecting to the vacuum vessels will be fed through the walls of this compartment directly into the cleanroom. In addition, the electrical power and cooling lines for the electronics racks can be distributed from this area, avoiding long lines through the experiment area.

3.1.6 Services

The air conditioning system itself will be located outside the hall, on the loading platform. The controls for the air conditioning system and its diagnostic information have to be accessible to the user from the main control room. In case the specified environmental conditions cannot be maintained an audible and visible alarm must alert the user in the main control room. The cold water and electricity required by the air conditioning will be provided by the university separated from the infrastructure for the other services. The cooling and heating power of the system depends mainly on the insulation used and the conditions inside the hall.

The water cooling of the equipment inside the hall will be controlled by a cooling plant located in the printing hall outside the cleanroom. All equipment will be cooled locally, using water cooling, in order to keep the requirements for the air conditioning system at a reasonable level, to avoid hot spots and to reduce uncontrolled air turbulence to a minimum. Therefore the total water cooling power required is 140 kW, corresponding to the maximum expected dissipation in the aforementioned equipment. A primary circuit supplying water of $6 ^\circ\text{C}$ and a return temperature of $12 ^\circ\text{C}$ will provide

¹equivalent to US FED STD 209E class 100.000

this cooling power. Separate cooling circuits will be used for the laser, the pumps and the electronics. Each cooling circuit will have its own pressure and temperature regulation system and will provide interlock signals to be used for the protection of the corresponding systems. The cooling lines inside the clean room will be insulated to avoid condensation. Routing of the cooling water and electrical power lines inside the hall will be done above ground. Feed throughs in the walls of the cleanroom for cooling water will be on the side of the office building. Electrical power distribution will be partly done outside the clean room, originating from the central 400 V switch board in the hall.

Liquid nitrogen will be provided from a 15 m³ tank located on the south side of the building. The foreseen average flow rate is about 580 Ld⁻¹ with peak flow rates during cool down of the cryogenic system, see section 4. A feed through for liquid nitrogen will be placed on the south side of the building. There will be many connections for the vacuum system and cooling lines between the area for noisy equipment (see section 3.1.5) and the experiment area.

Maintenance to the clean room itself will be mostly done from the inside and it is essential that the lighting and the roofs of the enclosed compartments are reachable with a sky jack. Therefore, the routing of the cables and tubes must be compatible with the passage of a sky jack.

3.1.7 Access

Large objects

Large objects, such as the parts of the towers and the vacuum tubes, will be brought in from the loading platform in front of the building through the building door and an additional door in the clean room itself. For moving the heavy parts of the vacuum system from the delivery truck into the building an electrically propelled cart will be used. The objects will then be unpacked inside the unloading area inside the building and prepared for installation. Movement to any of the other areas is foreseen through the roof of this compartment, using the cleanroom crane. A 4 m by 4 m hatch in the roof of the loading area will allow the crane access this area. The loading area will inevitably be less clean than the main area so contamination of the main area will be prevented by strict working procedures. The roof and the door will never be opened at the same time and the the equipment as well as the entrance area will be cleaned before equipment is transferred to the main area. The air flow in this section of the clean room will be designed to control the flow between the different compartments such that the experimental area conditions will not be compromised. Access to this area is preferentially directly from outside the building.

Small equipment and people

Small equipment and people can be brought into the clean room through air locks that prevent loss of air pressure in the experiment area. The experiment area is connected to the office building by an air lock that also connects to the cleaning area. This will be the main access route for personnel to work on the experiments. Each airlock will provide adequate safety equipment and cleaning material as well as personal cleanroom suites, shoes and other material needed to guarantee the cleanliness of the area.

Two additional airlocks provide access to the noisy equipment area from the experiment area. Through these air locks also the loading area can be reached but the recommended access to the loading area will be from outside the building, see section 3.1.7

Area	22 m × 34.3 m
Height	8 m
Class	ISO 8
Temperature	(20 ± 1) degC
Humidity	(50 ± 15) %RH
Ventilation	10 changes/hr
Air recycling	90 % recycled
Air cooling power	TBD kW
Electrical power for air conditioning	TBD kW
Electrical power for equipment	140 kW
Water cooling power	140 kW

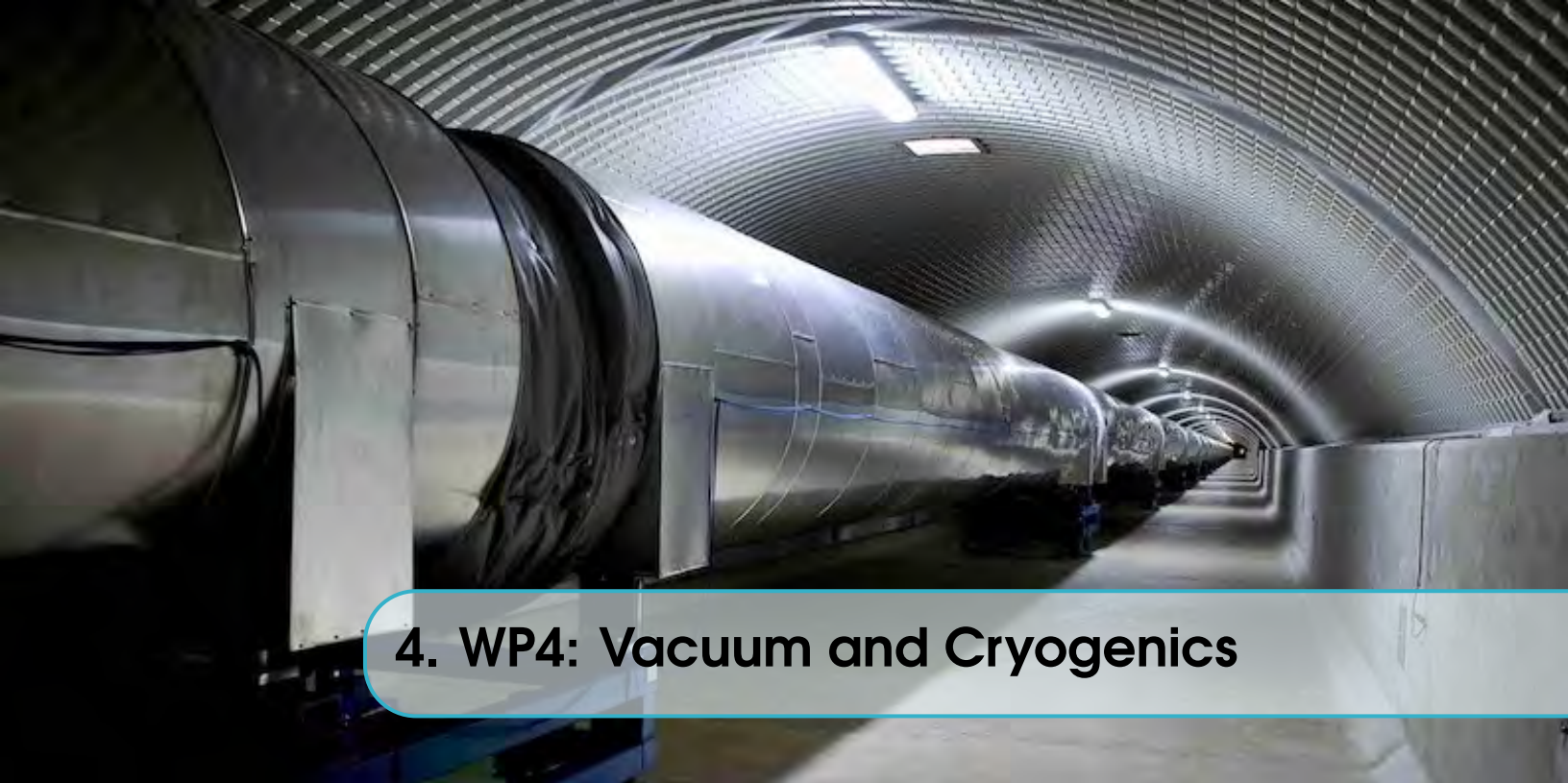
Table 3.1: Specification of main parameters of the cleanroom

3.2 Specification summary

3.3 Work Break Down Structure of the cleanroom WP

description	Start	End	Remarks
Tender procedure	1-3-2020	1-9-2020	Detailed tech specs, call, selection
Detailed design	1-9-2020	15-10-2020	with selected cleanroom builder
Implementation	15-10-2020	15-1-2021	by cleanroom builder

Table 3.2: Work breakdown for the realisation of the cleanroom facility



4. WP4: Vacuum and Cryogenics

4.1 Overview of the Vacuum and Cryogenics WP

In order to obtain a highly sensitive laser interferometer, it is crucial to install the main optics inside an ultra-high vacuum system. Even at room temperature, this system needs to be well-designed to meet the vacuum requirements (partial and total pressures, safety) and ease of operation: interventions are unavoidable and one has to make sure that vacuum can be breached in a safe manner without polluting the system; that all required optical and electronic view ports and feedthroughs are available and at the right place, that all interferometer components can be installed and reached, and that the system does not introduce excessive vibrational noise (that may impact the interferometer via scattered light and via coupling through the suspensions). When one also wants to cool down the main optics, these requirements only grow more stringent: one must be able to avoid water freezing on the mirrors and one needs to be able to reach good vacuum around the mirrors that will be enclosed by thermal radiation shields, both for cryogenic operation and at room temperature. The presence of the radiation shields will lead to lower vacuum conductance and more outgassing at room temperature. Therefore, the design of the cryogenic cooling and vacuum system are strongly interwoven and for ETpathfinder we describe the system in a single work package.

In section 4.2 the requirements that we place on the vacuum and cryogenics system are described. Section 4.3 gives an overview of the integrated system, section 4.3.2 describes the vacuum system and the mechanics, and section 4.3.3 describes the cryogenic system.

Obviously, the vacuum and cryogenics work package has a strong interface with WP5 since the seismic isolation system is enclosed inside the vacuum towers and mechanical and thermal transfer functions need to be specified, especially vibrations introduced via the cooling system to the suspended mirrors. Also, the dimensions of the beam pipes, view ports, thermal shields, baffles etc. are driven by the optical layout; especially scattered light has an impact. There is also a strong interface with WP3 (clean room); vibrating systems may be placed on regions of the floor (i.e. with a separate foundation); the cryogenic system needs the most power and cooling water of all components in the ETpathfinder facility and places hence the strongest constraints on the air conditioning of the clean room. The placement of critical components must be optimized; pump

outlets must be connected to hoses leading outside the air-conditioned region of the clean room (and when possible, pumps should be placed outside the clean room wall), and in general feedthroughs for gases, power, and cooling water are needed through the clean room walls. Therefore, the design of the clean room (placement of the walls, capacity of the air conditioning, feedthroughs, etc.) is strongly dependent on the cryogenics and vacuum design. Finally, the vacuum and cryogenics system needs to be controlled. For safety reasons, it is necessary to have a PLC control system, a fail-safe state machine, so that in case of power failure or compressed air failure the correct actions are taken (stopping the liquid Nitrogen flow, closing valves, etc). Also, we want to avoid human errors in manually venting, evacuating and cooling down/heating up; that should be done via the PLC-control system. It is foreseen that this control is dedicated for WP4, and separate from the ETpathfinder slow control (WP7), but that necessary signals needed to operate, control and monitor the laser interferometer are duplicated/ monitored by the slow control part of WP7.

4.2 System requirements

The ETpathfinder facility aims to develop and demonstrate techniques that can be used in future, third-generation, cryogenic gravitational-wave interferometers. As such, we want to operate a Michelson interferometer in which the input and end mirrors of the Fabry-Perot cavities in the two arms are cooled to reduce fundamental thermal noise, and in which these mirror surfaces are freely floating. For the maximal level of vibrational noise on the mirror surfaces we aim for an amplitude spectral density of less than 10^{-18} m/ $\sqrt{\text{Hz}}$ at 10 Hz, and well below that at higher frequencies. We want to be able to operate the interferometer at mirror temperatures around 123K and around 10 K. Around 123 K, the coefficient of expansion of Silicon equals zero, so thermo-elastic noise does not couple to thermally excited mechanical vibrational modes of the mirror. At 10 K, all the thermal noise (also broadband noise from the suspension, Brownian motion, and the noise in the mirror coatings) is reduced since there is less thermal energy to be dissipated.

The requirements on the vacuum and cryogenic system are determined by these considerations: We want to be able to operate the interferometer at room temperature (around 300 K), at 123 K and at 10-20 K. We must be able to monitor, control and stabilize the mirror at these temperatures. The residual gas pressure in the vacuum system must be low enough to avoid excess noise limiting the displacement sensitivity of the interferometer at any of these working point temperatures. Both the vacuum and cryogenic system should not limit the noise budget in any way: neither via mechanical vibrations introduced via the mirror suspensions nor via scattered light. Finally, water freezing on the mirror surface (as well as carbohydrates in the vacuum) should be avoided. The system should be relatively easy to operate; especially in the central tower that hosts an optical bench with many elements that may need tuning, access should be possible on a daily basis, meaning that we want to be able to vent and re-evacuate that tower in less than 1 day of time.

4.2.1 Vacuum requirements

Noise induced by residual gas

A good vacuum is needed to optimize the sensitivity and enable working with cold mirrors. The residual gas in the system impacts the sensitivity in two manners: It causes optical path-length changes and rescattering of the beam in the arms and it causes fluctuations by impinging on the mirrors of the Fabry-Perot cavities. For the advanced GW detectors, the contribution from the arms typically dominates. The power spectral density of the optical-path length noise in the arms scales

with the pressure, the arm length, and molecular polarizability squared; dedicated measurements to validate this model and determine the expected noise for different rest gases have been presented by Whitcomb and Zucker in 1994 ([1]); the detection sensitivity of phase noise scales with the square root of the stored laser power in the arm. For Advanced Virgo, the goal is to obtain a residual gas pressure in the arms of 10^{-10} mbar. Since the pressure in the towers containing the end mirrors is substantially above that, cryolinks were installed to capture the water vapor leaving the towers containing the end mirrors and protecting the vacuum around the 3-km long beam line in the arms. For ETpathfinder, which operates at a much shorter arm lengths and at lower stored power, we are not dominated by optical path length changes due to residual gas in the arms as long as the pressure in the arms is below 10^{-7} mbar. However, the residual gas around the end mirrors have a much higher impact than in gravitational-wave observatories, due to the lighter mirrors we use. For the advanced GW detectors, the mirrors are much larger than for the (relatively) small optics in the starting phase (Phase 1) of ETpathfinder (mirror radius 75 mm, mirror mass 3.3 kg). The force exerted on the mirror is given by the product of the pressure and surface area of the mirror; fluctuations in it scale with the square root of these. However, the acceleration of the mirror is inversely proportional to the mass of the mirror. Overall, the acceleration noise scales as $1/D^2$ with D the dimension of the mirror. So where the Advanced LIGO and Virgo experiments up till now could cope with pressures around 10^{-6} mbar around the mirrors in the Fabry-Perot end towers, that is not the case for ETpathfinder (and also Virgo is currently trying to improve the vacuum for the next science run: it is starting to limit the sensitivity curve in certain regions).

From gas kinetics, one can derive that the impingement rate of gas molecules (for an ideal gas) on a surface equals

$$J = \frac{1}{4}\rho \langle v \rangle = \frac{N}{4V} \sqrt{8 \frac{k_b T}{\pi m}} = \frac{P}{\sqrt{2\pi m k_b T}}.$$

with J the impingement rate, ρ the density of the gas, k_b Boltzmann's constant, T the temperature, m the mass of the molecule, and P the pressure. For residual H_2O gas at a temperature of 300 K and a pressure of 1 Pa (10^{-2} mbar) this rate equals 3.59×10^{22} molecules/m²/s. Similarly, the momentum transfer delivered by these molecules are on average twice the momentum perpendicular to the surface, which turns out to be 2.79×10^{-23} kg m/s (and of course the product of these numbers add up to $1 \text{ N/m}^2 = 1 \text{ Pa}$). Assuming elastic scattering of the molecules, the fluctuations in the mirror position are caused by fluctuations in the amount of molecules that hit the mirror on the front or back side and is given by the square root of $2JA$ with A the area of the mirror (and the factor 2 comes from the fact that the mirror has a front side and a back side). A better calculation can be done, using the Energy Fluctuation Dissipation theorem and taking into account obstructions close by the mirror [2, 3]. One may consider additional noise from molecules trapped between the mirror and close-by objects, such as the reaction mass. The Brownian noise of the mirror can easily double in the presence of small gaps between the mirror and neighboring objects. Also, inelastic scattering can be taken into account; the molecules stick for a short time to the mirror surface and then leave. In such a calculation for inelastic scattering, the factor 2 obtained from elastic scattering is replaced by a factor $(1.5 + \pi/4)$ for a cylinder with a thickness equal to the radius [3]. Following Cavalleri *et al.* [3], one would arrive for the amplitude spectral density of the force from residual gas noise in ETpathfinder (mirror radius 75 mm, thickness 80 mm, and weight 3.25 kg) at

$$S_f = \sqrt{p \sqrt{\frac{128}{\pi} m k_b T [\pi R^2 (1 + h/2R + \pi/4)]}} \text{ [N}/\sqrt{\text{Hz}}] =$$

$$\sqrt{7.1 \times 10^{-23} [\pi R^2 (1.5 + \pi/4)] p} = 1.7 \times 10^{-12} \sqrt{[P/[1\text{Pa}]} \text{ N}/\sqrt{\text{Hz}}$$

An amplitude spectral displacement density below $10^{-18} \text{m}/\sqrt{\text{Hz}}$ for frequencies above 10 Hz would require pressures below $58 \mu\text{Pa}$ or $6 \times 10^{-7} \text{mbar}$ (effects from molecule trapping between mirror and baffle/reaction mass not included; for small gaps the residual gas noise can increase considerably).

For ETpathfinder the strongest constraint on the vacuum performance come from residual gas impact on the cavity mirrors, not from optical path-length fluctuations in the beamline. The vacuum system needs to be good enough to reach pressures below 10^{-7}mbar around the Fabry-Perot mirrors, also when operating at room temperature (where the residual gas pressure will be higher since the cryogenic shields do not pump water vapor in this case).

Water vapor

A second vacuum concern is the cleanliness of the system. The optics need to be kept clean and for that reason one wants to limit lubricants and use oil-free pumps as much as possible. Indeed, in the ET CDR [4] a partial pressure of $< 10^{-14} \text{mbar}$ for CH (hydrocarbons) at the mirrors was mentioned, since these molecules may undergo strong chemisorption at the mirror coating surfaces and destroy the mirror. For Advanced LIGO a more specific limit was given as a function of the mass of the hydrocarbon molecules; for fragments lighter than 100 amu the allowed partial CH pressure amounted to $1 \times 10^{-12} \text{mbar}$ [5]. To obtain such low pressures is very challenging; we will limit the amount of CH-molecules as much as possible by not using MLI (multi-layer superinsulation) inside the primary vacuum, use oil-free pumps, and limit the amount of Kapton and Teflon inside the primary vacuum around the mirrors much as possible.

Less destructive, but still a major concern, is water vapor. Water binds strongly to metal surfaces, with binding energies of 95-105 kJ/mole for a mono-layer of water on stainless steel or aluminum (see e.g. [6]) (chemisorption). This implies that the dwell time of water molecules on the metal surface at room temperature is in the order of hours; whereas the dwell time for a noble gas would be in the order of 10^{-13} seconds. The binding energy of water on water is much lower, in the order of 25 kJ/mole. The sticking time on the surface follows from Boltzmann statistics, $T = T_0 e^{E_b/k_b T}$ with E_b the binding energy per molecule. For the physisorbed multi-layers of water (bound on water), the dwell times are in the order of microseconds. One can also define a sticking coefficient, which describes the probability that an impinging molecule will find a free site on the surface lattice and sticks to it. For clean surfaces (after baking your vacuum system) these sticking coefficients are high, in the order of 0.2-0.5. For surfaces after a vacuum breach there are typically tens to hundreds of water layers present during initial pumpdown, and the sticking coefficients are much lower (0.01 or lower) since most lattice sites are occupied already.

A mono-layer of water on a metal surface contains in the order of $2 - 5 \times 10^{19}$ molecules, depending on the surface roughness (it is very high for anodized Aluminum; that is not compatible with our design. If optically black Aluminum surfaces are needed, e.g. to reduce scattered light, then these surfaces need to be treated with a UHV vacuum-compatible coating). It is good to realize that at a partial water vapor pressure of 10^{-6}mbar , a mono-layer on a fresh metal surface builds up in only a few seconds of time. Clearly, operating the mirrors under cryogenic conditions needs a strategy to avoid building up thick layers of ice. The partial pressure of water vapor directly around the mirror should be very low, below 10^{-10}mbar , when the mirror is cooled to cryogenic temperatures.

When pumping down a vacuum system, the pressure typically decreases very rapidly to the 10^{-5}mbar range, at which time the surfaces of the vacuum system contain a saturated mono-layer of water

and the other residual gas (air and the outer water layers) has been pumped out already. At that time, the pressure inside the vacuum system is determined by the amount of water vapor coming from the walls. If the resident time of a water molecule on the metal walls equals T_s seconds and one needs on average N_b wall bounces before the water molecule is removed by the pump then the pressure decreases as $e^{-t/(N_b T_s)}$. Typically, the pressure decays a power $1/t$ with t the time that the system is pumped on. In the simple model with 1 binding energy for all sites, that $1/t$ dependence is due to the variation of the sticking probability, that rises when the monolayer is depleted and more sites for binding water are available. Alternative descriptions use a range of different binding energies for different sites on the metal; then also the first part of the mono-layer is pumped more quickly (due to smaller binding energy) than the last part. Typically, after about 10 hours of pumping the outgassing of water vapor amounts to about 3×10^{-9} mbar l/s /cm² (see e.g. [7]) at room temperature (consistent with about 10^{12} molecules/s/cm² leaving the surface, and a full mono-layer sticking time of a few thousand seconds).

At room temperature, for our case, the average residence time for water molecules is in the order of 10000 seconds with a sticking coefficient of 0.2, and we need on average in the order of 20000 wall bounces before the molecule passes the pump aperture; it would take years to reduce the pressure of the water vapor by a decade under these circumstances. However, the sticking time reduces exponentially with temperature; if one raises the temperature even moderately (from 20 to 65 deg. C) then a factor of about 300 is gained in pump-down time. In our design, we can reduce the residual gas pressure by several orders of magnitude by baking for two weeks. One needs to heat all surfaces exposed to the vacuum to this 65 degrees however; when part of the surface remains cold then that part will keep a fully saturated mono-layer of water, that slowly comes off after baking has terminated.

Baking the system is the only practical way in which the water vapor can be removed from the vacuum system and the possibility to bake may be required also when regeneration of thermal shields/water traps are necessary. We will design the system in such a way that we can bake out at 65 deg. C when necessary. However, baking out a system is a major operation. The full vacuum system has to be heated to 65 degrees for two weeks. The alternative to avoid ice build-up on the mirror is to freeze the water on a cryolink around the mirror (in our design that is an outer thermal shield, cooled by liquid Nitrogen).

In our design, the end mirrors are surrounded by 2 cryogenic shields (necessary to reduce the heat load from thermal radiation). We plan to first cool down the outer shield to liquid Nitrogen temperature while maintaining the inner shield at room temperature or above. When these outer shields are cold, water vapor will freeze on it; the shields act as a cryo pump with very high pumping speed (~ 150000 l/s/m²), so all water vapor inside the vacuum system will freeze on this shield within a few days of time (on average, far less wall bounces are needed to hit a shield than to pass through the aperture of a turbo pump). Some water will still come off the shields at 80 K; the sticking time of the water on the shield depends on the thickness of the layer of ice on it and on the temperature of the shield. Nevertheless, the partial pressure for water around the mirror can be reduced by ~ 4 orders of magnitude by cooling the outer shield and we expect that this is sufficient for ETpathfinder operations.

Note, that in order to avoid water freezing on the mirror, one needs to be able to either bake the full system so all water inside the vacuum vessels is removed, or to be able to construct a cryotrap on which all water freezes, while keeping the mirror (and the rest of the vacuum system) warm: separate cooling systems are needed for the mirror and for the shields around the mirror. Therefore we chose

not to use conventional refrigeration schemes in which the first stage of a cooler is connected to the (outer) cryogenic shield and the second stage to the inner cryogenic parts.

Water vapor dominates the partial residual gas pressure in a stainless-steel vacuum chamber down to below 10^{-9} mbar; at lower pressures ($10^{-10} - 10^{-12}$ mbar), hydrogen and carbon monoxide molecules start dominating. These atoms and molecules slowly diffuse out of the stainless steel. We do not try to remove these components; that would require baking to well above 250 degrees of C and we do not aim for final pressures below the 10^{-9} mbar range. Hydrocarbons might also give large partial pressures in this range, depending on the materials inside the vacuum system and the types of pumps applied.

Vacuum Considerations: Thermal Shields

As will be discussed in the next section, thermal radiation shields around the mirror are required in order to reduce the heat load from thermal radiation. The requirements on these shields are that they allow for optical view apertures, that they have high enough vacuum conductance to meet the vacuum requirements, and that they do not limit the noise budget due to scattered light contributions.

Surface treatment

The thermal emissivity of the inner surface of the vacuum vessel, the amount of water molecules in a mono-layer, and their binding energy depend on the surface treatment. From the vacuum and thermal radiation perspective, it would be optimal to electropolish these surfaces. However that would be very expensive, and render the inside of the vacuum vessel shiny and mirror-like, which is very disadvantageous from a scattered light perspective (stray light will keep bouncing inside the vacuum system instead of being absorbed). A cheaper technique would be to treat the surfaces with glass pebble impingement; this is demonstrated to reduce the binding of water to the surface and leaves the surface optically diffuse (instead of mirror-like) (See e.g. [8]). Sometimes, one anodizes aluminum to get optically black surfaces. This is a nightmare from vacuum perspective and should be avoided; surfaces that need high emissivity in the infrared spectrum (black surfaces), need to be coated with an UHV-consistent coating (for instance available from Acktar, "<https://www.acktar.com>"). Dedicated beam dumps that should absorb scattered light (the baffles around the beam) may be coated with anti-reflective coatings at the frequency of the infrared laser light. In the calculations in this report, it is assumed that those coatings also have high emissivity at the wavelengths of thermal radiation (around $10 \mu\text{m}$).

4.2.2 Requirements on the cryogenic system

The ETpathfinder facility should be able to operate at room temperature, at 123 K, and at temperatures around 10 K. The cryogenic system should not introduce vibrational noise above $10^{-18} \text{m}/\sqrt{\text{Hz}}$ at frequencies above 10 Hz. The mirror temperature needs to be monitored and controlled with precision at these temperatures. Also, thermal shields must not block the beam or the optical levers needed to read out the position and orientation of the mirrors and marionettes. We meet these requirements by having a hybrid cooling system; a liquid Nitrogen system for rapid and powerful cooling (hundreds of Watts) to 80-100 K, and a Helium sorption cooling to temperatures of 10-20 K. Possibly, intermediate temperature reservoirs will be used too.

Multi-layer superinsulation

As already mentioned in the previous section, the use of MLI superinsulation inside the vacuum around the mirror is highly undesirable. In cryogenic experiments one generally wraps the cryogenic

piece of equipment and the heat links towards that object in many layers of superinsulation to reduce the thermal radiation load of the warm environment on the test object. However, it is difficult to evacuate these layers since pumping speed between the layers is small. The layers will also be saturated with water vapor, that will slowly dissipate into the primary vacuum system and spoil the vacuum for a long time (centuries).

In many cryogenic experiments, one is not concerned with the water vapor on the MLI foils, since when the target is cooled, the water on the cold inner MLI layers will be frozen. In our experiment however we have many view ports for the beams and optical levers, and whereas the water will be frozen on the inner layers close to the mirror, it will not be frozen on the layers facing the room temperature environment so water will keep coming off the MLI foils. Furthermore, it will be impossible to pump off all the water from the MLI foil surfaces when operating the facility at room temperature.

Also, given the extremely low limits of hydrocarbons that are allowed in the Einstein Telescope (partial pressure below 10^{-14} mbar [4]), use of MLI foils would probably not be compliant with future generation gravitational-wave interferometers, thus we will avoid these materials in ETpathfinder too.

Using superinsulation would require packing stacks of foils in vacuum-tight and sealed enclosures and mounting these sealed stacks into the primary vacuum chamber; although that may be required in future, large-scaled facilities, we deem such a scheme impractical for ETpathfinder, since we have very little space around mirrors and marionettes and we need many view ports for beams and optical levers around the mirrors in the end towers; we cannot waste time on investigating complicated schemes that require vacuum-tight packaging of MLI foils around the mirrors.

4.3 Vacuum and Cryogenic Design

4.3.1 Model calculations

In order to design the vacuum system and the cryogenic system, a simulation package has been written. This package can track rays (either molecular flow of atoms or electromagnetic radiation) through the system. The inside of the vacuum towers and optical components are described in terms of elements of rectangular blocks, cylinders, disks, spheres and cones. More complicated structures are constructed from combinations of these base elements.

Each structure can have cylindrical holes inside (or rectangular holes). Each surface of these structures (e.g. inside/outside/top and bottom rim of a cylinder) and the rims of the holes can have different optical properties: the emissivity can be set and for electromagnetic radiation, the scattering may be specular (angle of incidence equals angle of reflection) or diffuse (homogeneous), or a combination of these two.

We need baffles for stray light absorption and thermal radiation absorption in our facility. We assume either disk-shaped baffles, mounted e.g. on the reaction masses around the mirrors, or conical baffles, where the latter shape can be mounted inside a cylindrical tube. In our simulation, a conical baffle has a flat base and a top rim that is perpendicular to the conical inside/outside, see Fig. 4.1. This shape is used in the simulations in this report. The tubes around the beam pipe contain threads; we can replace baffles at the ends of the tubes without modifying the tubes. In that manner, we can design baffles with different apertures, different shapes, and different absorptive coatings, and replace baffles when needed.

For the calculations presented in this section, a few billion ray trajectories have been traced (taking a day of CPU-time on an iCore-7 machine running Ubuntu).

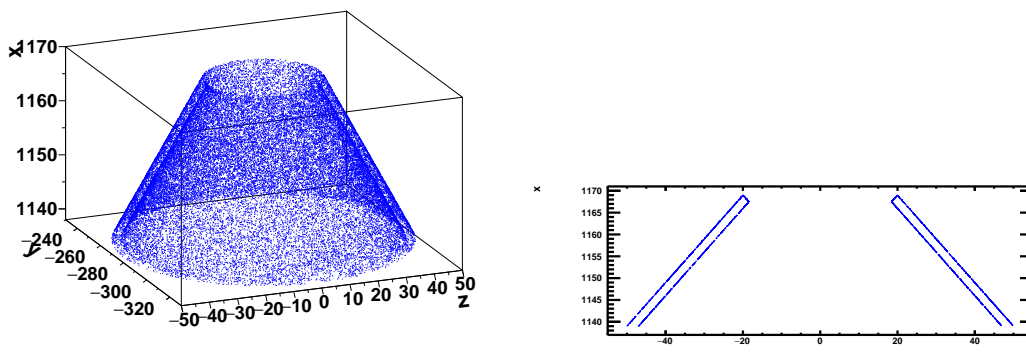


Figure 4.1: Left: Start points of traces coming from one of the conical baffles that are used as element in the simulation. Right: cross section around the beam axis for the same traces. The top rim of the cone is perpendicular to the sides of the cone.

In case of vacuum simulations, the aim was to specify the conductance in molecular flow regime from the different parts of the system to the pumps. Combined with models describing the binding of the mono-layer of water, pressure curves and pump-down times could be simulated for different thermal shield configurations and different placements/sizes of the pumps.

In case of cryogenics, the aim was to calculate the radiative and conductive heat transfer between all different elements in the setup. Since in equilibrium, the dominant heat loads on the mirror come from thermal radiation, the design of the thermal shields is crucial. The shields need to have enough holes for vacuum conductance but also need to stop and reflect thermal radiation. Therefore, the placement of the holes and the emissivity of different surfaces should be optimized. (One usually makes thermal shields highly reflective. However, in our case the outer thermal shields need to absorb or reflect outwards more than 99.5 percent of the room temperature thermal radiation; less than 0.5 percent may be transmitted through holes. At higher percentiles, the room-temperature thermal radiation from the tower walls will be the dominant contribution to the heat load on the inner cryogenic shields, instead of the thermal radiation coming off the outer cryogenic shields).

For the thermal calculations, thermal radiation was tracked through the system until it is absorbed, and the thermal radiation loads of each surface to all other surfaces were calculated using the simulation package. Also conductive heat flow from each element to its neighbours was calculated using known thermal temperature-dependent conductivities and cross-sectional areas between the centers of the elements. The temperatures of the elements are varied until equilibrium is achieved. This defines the end temperatures of the floating shields (radiative equilibrium) and the cooling powers needed for the cryocoolers to maintain this equilibrium (thus the radiative heat flow is the opposite of the conductive heat flow for all elements except the heat sources (tower walls) and sinks (cryocooler heat exchanger). Just in January 2020, the code has been modified to also describe the cool-down times (masses and specific heats are added and the coupled differential set of equations is evolved in time, tracking the stored heat in all elements as well as the heat currents). This was numerically challenging, since especially the conductivity of the monolithic suspensions far exceeds the stored heat in these suspensions; the conductivity exceeds $10 \text{ kWm}^{-1}\text{K}^{-1}$ at 10-20 K whereas

the stored heat is less than a mJ. It took several code revisions and algorithm optimizations to be able to accurately evolve the coupled differential equations with small numerical errors for our setup, and at the time of writing this design report only a single time-dependent heat transfer calculation has been performed.

4.3.2 Vacuum System

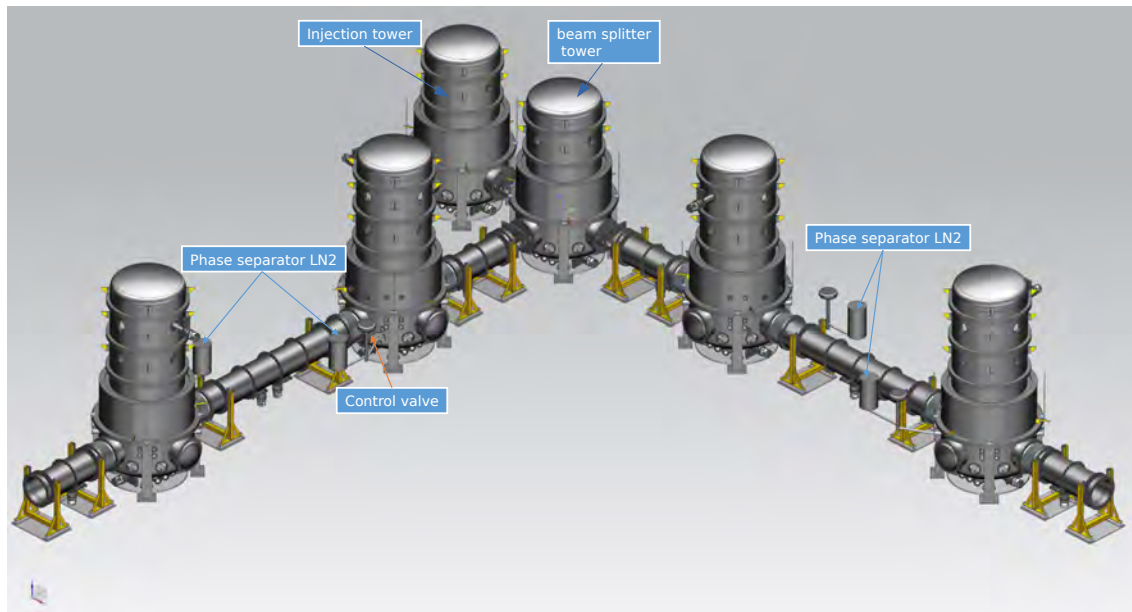


Figure 4.2: Overview of the vacuum towers containing the optics. The distance from the beam splitter tower to the end of the arms equals 19.5 m, the distance between towers in the arms hosting the Fabry-Perot cavities equals 9.3 m. Diameter of the beam pipes in the arms equals 0.8 m. Lifting ears and supports are indicated in yellow. Location of the liquid nitrogen phase separators and flow control valves are also indicated.

Fig. 4.2 gives an overview of the mechanics of the vacuum system in ETpathfinder. The bench containing the laser will be located in air and is not shown; the laser light will be transported to the injection bench located in the injection tower. Mode cleaners etc. can be placed on this bench and between the injection tower and the bench in the beam splitter tower, the central tower in this scheme. The beam splitter tower is connected to 2 arms, hosting the Fabry-Perot cavities. Using small optics, two Fabry-Perot cavities can be folded in a single arm; in that case the beams are parallel and separated by 550 mm.

The ETpathfinder facility is also capable of hosting large optics, at the scale of Einstein Telescope (mirrors in excess of 200 kg). In that case, the beams will travel in the center of the arms and each arm hosts a single Fabry-Perot cavity.

The height of a tower equals 6.1 m; the diameter 2.8 m. The tower segments fit in between the beams of the crane so the height of the hall can be maximally exploited.

The arm length (the distance between the end mirrors of the Fabry-Perot cavities) equals 9.3 m. The beam sizes are of the order of a few millimeters only, so in principle it would have been possible to use a small diameter beam pipe (e.g. 100 mm diameter). However, that would impact the

flexibility of the facility. We want to maintain flexibility to choose different beam paths inside the arms, maybe for a ring cavity or additional cavities for squeezing or other future experiments, and to use space for extended cryogenic shields of larger dimensions. Therefore, the beam pipe between the arms have an inner diameter of 800 mm, to allow for future modifications and operations.

A gate valve closing an 800mm-diameter pipe would have massive dimensions (several meters high) and be very expensive (a few hundred k€ per gate valve); we deem such valves not practical for the ETpathfinder facility. However, we do not want to be forced to vent all six towers for every intervention. Especially when the interferometer is operated cryogenically, we want to be able to separate the vacuum system of the cryogenic arm from the vacuum system of the beam splitter tower, so that the arm can remain cold. Therefore, a manifold consisting of 200-mm diameter pipes with 3 gate valves is inserted between the beam splitter tower and the arms. The vacuum vessels of all towers are equal; the towers have 800-mm flanges. Therefore, this manifold can be removed if we need the full 800-mm opening in some future scheme (large optics); but then obviously we cannot separately evacuate the arms and the central towers, so interventions should be limited during cryogenic operations (max about 2 shutdowns with vacuum breach per year).

The wish to support 800-mm diameter beam lines raises the height of the rim of the tower base to 1750 mm above floor level; the rim of the base of the towers in the arms has to be above the top of the 800-mm flange connecting the tower to the arm. The beam line is at a height of 1200 mm above floor level (same as at Virgo).

The base of the tower is the heaviest individual part that needs to be lifted inside the ETpathfinder facility, it weighs about 3500 kg. The tower base contains four 800-mm openings under 90 degrees; for the beam splitter tower 3 of these are connecting to neighboring towers and for the towers in the arms 2 ports are connected to beam pipes, whereas the other 2 flanges can be used for access to the tower. The base also supports four 300-mm CF flanges that can be sealed with ConFlat metal seals. In the current design, 1 or 2 of these 300-mm ports are used for mounting turbo pumps, 1 port is used for cryogenic feedthroughs, and the other ports can be used for signal feedthroughs. Furthermore there are smaller ports and flanges for the optical levers and at the bottom there are more flanges, connected to 200-mm cylindrical pipes, to be used for the vacuum system, for cryogenic feedthroughs, and for signal and control cables. Fig. 4.3 shows a drawing of the tower base with the openings for access.

The towers comprise separate segments that fit in between the beams of the crane so the height of the hall is maximally exploited (a higher tower could not be installed in this hall). The segment directly above the tower base (starting 1750 mm above floor level) is wider than the segments above it and can be lifted to access the optics and equipment inside the tower. It will be placed on metal feet during installation activities. This is shown in Fig. 4.3. Production drawings for the towers commenced in September 2019 and the assumption in this section is that the majority of these drawings are used in our final design.

A more detailed description of the mechanical design of the vacuum vessel is beyond the scope of this design report; There are many details already worked out in the design. Here, we want to mention that care has been taken to ensure that one can install and reach all parts. A 3-D model of the tower and suspension system has been made, a 3-D virtual reality system to examine the ETpathfinder facility and the towers has been created, a wooden mock tower base has been produced, and some procedures for mounting the optics, the cryogenic shields, etc. have been worked out. On the right side of Fig. 4.3 several drawings with technicians working inside the tower are shown to give an impression. Also, some stress calculations have been performed (see Figs. 4.4, 4.5, and 4.6)

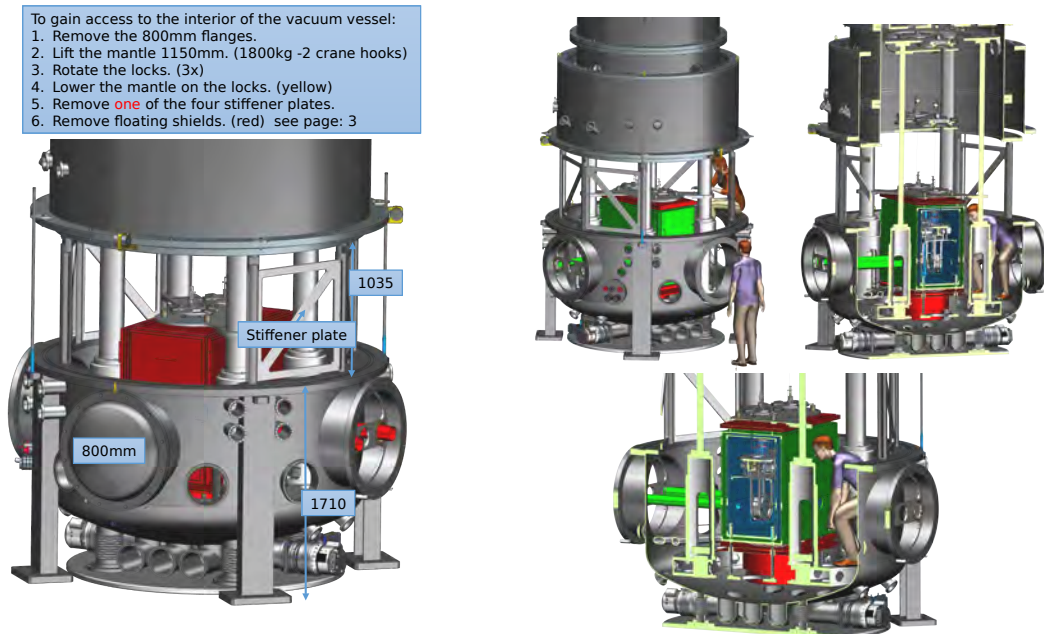


Figure 4.3: The lower part of the vacuum tower is shown with its ports for access. Dimensions are indicated. The segment directly above the the base is wider than the top segments of the tower and can be lifted 1105 mm upwards and placed on locks (indicated in yellow). The modeled personnel on the right side of this figure give an impression of the dimensions, accessibility and work conditions.

and the mechanical integrity and safety issues will be externally reviewed by an industrial partner, i.e. the Settles Savenije engineering company.

The mirror package can be mounted via rails located inside the cold screens; parts of the tooling for transportation and mounting/installing the mirrors must still be designed.

To seal the segments of the tower for vacuum, Viton O-rings are selected. All-metal helicoflex seals of such size would be impractical (due to the difficulty to get a tight connection), very expensive, and maybe unobtainable. In order to limit leakage, all seals consist of double O-rings, with in-between a pump feedthrough to evacuate the space between the O-rings to better than 1 mbar. For Viton rings the leak rate (dominated by water) equals $Q = 4 \times 10^{-10} A/d\Delta p$ l/s with Δp the pressure difference and A and d the exposed area and thickness of the Viton ring (compressed) in cm; in our case about 10^{-6} mbar l/s per seal. Since we foresee more than 5000 l/s pumping speed per tower, the ultimate end pressure that can be obtained due to this leak rate is around 10^{-9} mbar. Without differential pumping between the seals it would be impossible to reach our design goal for vacuum pressure, we would be limited to 10^{-6} mbar. We also intend to pre-bake the Viton seals before installing in the ETpathfinder facility; un-baked O-rings can contain a lot of moisture that slowly enters the vacuum. Baking the O-rings in a separate vacuum vessel before installing the inner O-ring will reduce the water load substantially.

A schematic layout of the vacuum system is shown in Fig. 4.7. We plan to use one large screw pump with high pump speed at atmospheric pressure to evacuate the full system to 1 Pa. Such a large pump is noisy (70 dB(A)) and uses a lot of electrical power (15 kW) and cooling water (20 l/s cooling water required); therefore we want to place this pump outside the conditioned area of

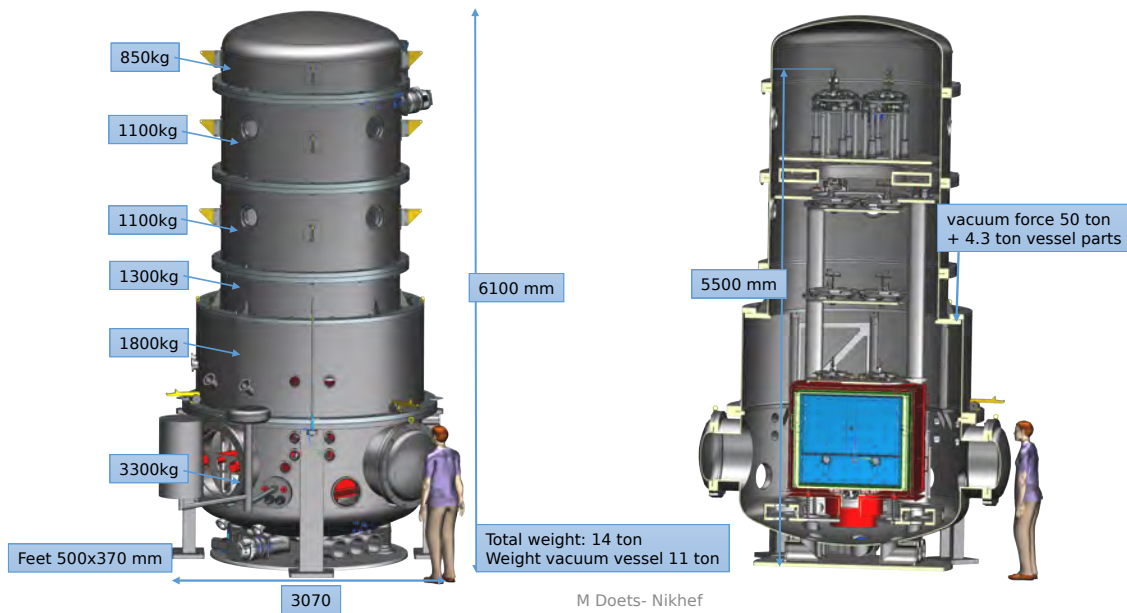


Figure 4.4: Side view of an arm tower. The weights of the individual parts are indicated. Maximal force is exerted on the rim of the tower base under vacuum (0.44 MN).

FEA model Stress (half symmetric model)

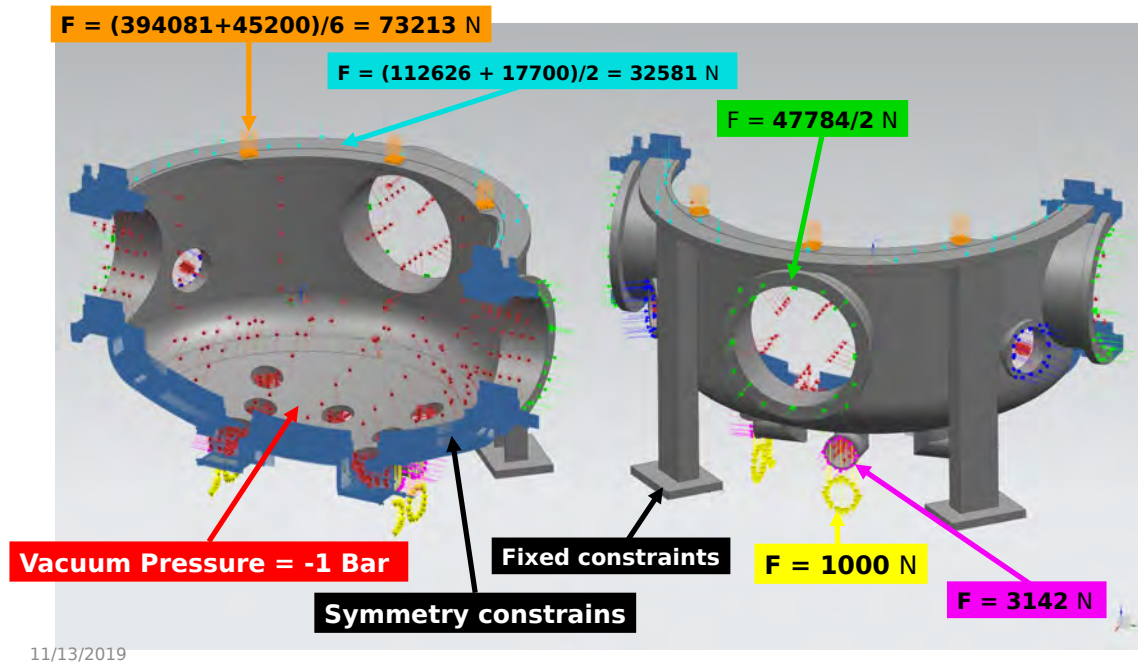


Figure 4.5: Stresses and forces calculated in a FEM model of the tower.

Results Stress / deformation

Yield Stainless(304) 210MPa

Global stress 0-100 MPa; Peak 184 MPa very local in weld connection to stand, not a dangerous place
 Deformation of 0.4mm at connection to top vessel has to take into account for the vacuum connections

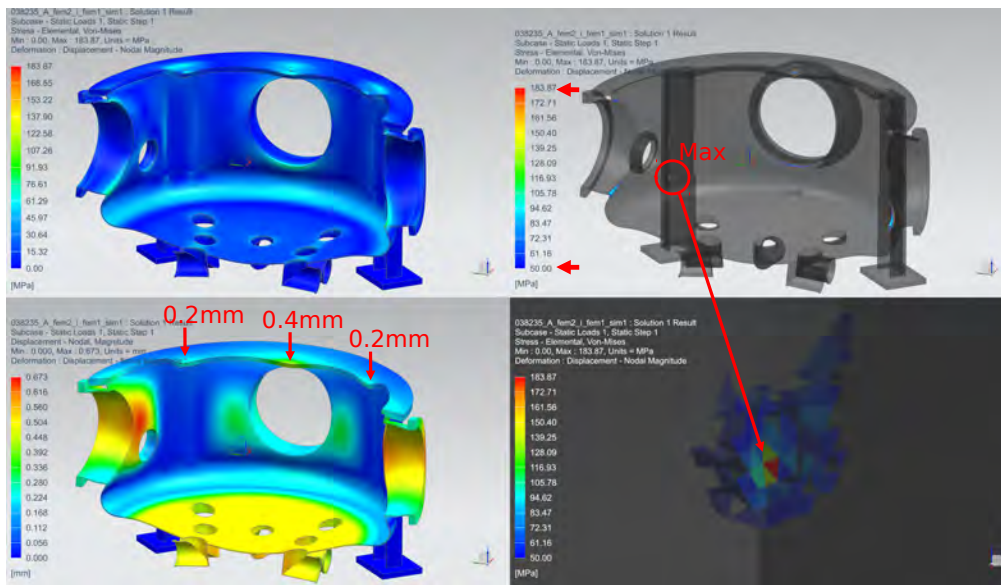


Figure 4.6: Stresses and deformations under vacuum of the tower.

the clean room. In order to not limit the pumping speed too much, a 100-mm diameter manifold connects the screw pump with the 3 vacuum systems (the X-arm, the Y-arm, and the BS/injection towers, indicated in blue, green, pink).

UHV is obtained by using turbo-drag pumps with magnetic bearings; these pumps induce much less vibrational and acoustic noise than cryo pumps, whereas alternatively getter pumps are not suitable for systems that are regularly vented, and also might pollute the environment (via sputtering). In the current design, 5 turbo pumps are connected to each arm (1 per tower and 3 in the arm sections) and 4 to the injection/beam splitter vacuum system (all to the towers). Hence, failure of a single turbo pump can be mitigated by using the other pumps, at a cost of 20-25 percent pump speed for the involved section. We chose large turbo pumps (pump speed 3200 l/s for water) since the largest alternative that we could fit below the tower (using ISO-CF 200 flanges) had half the pump speed but were less cost-efficient (about 90 percent of the price) in the quotations that we got. We also feel that it is advantageous to have only one type of turbo-pump for ease of maintenance, spares, etc.

Since during science runs we want to minimize noise and thermal excursions, we want to back up the turbo pumps by multi-stage roots pumps and turn off the screw pump when a base pressure of 10^{-3} mbar is reached. The roots pumps have lower pump speed (especially at 1 bar) but can reach a lower fore-vacuum pressure, consume less power, and produce less acoustic and vibrational noise. We chose to have 3 of these roots pumps for backing the turbo pumps, one roots pump per vacuum system (the X-arm, the Y-arm, and the beam splitter/injection tower). Using a manifold, each roots pump can also evacuate the other systems, so in case of failure one could continue operation with 2 (or even 1) roots backing pump. The capacity of the roots pump is large enough for such operation. To simplify the system and facilitate venting of the three primary systems individually, we

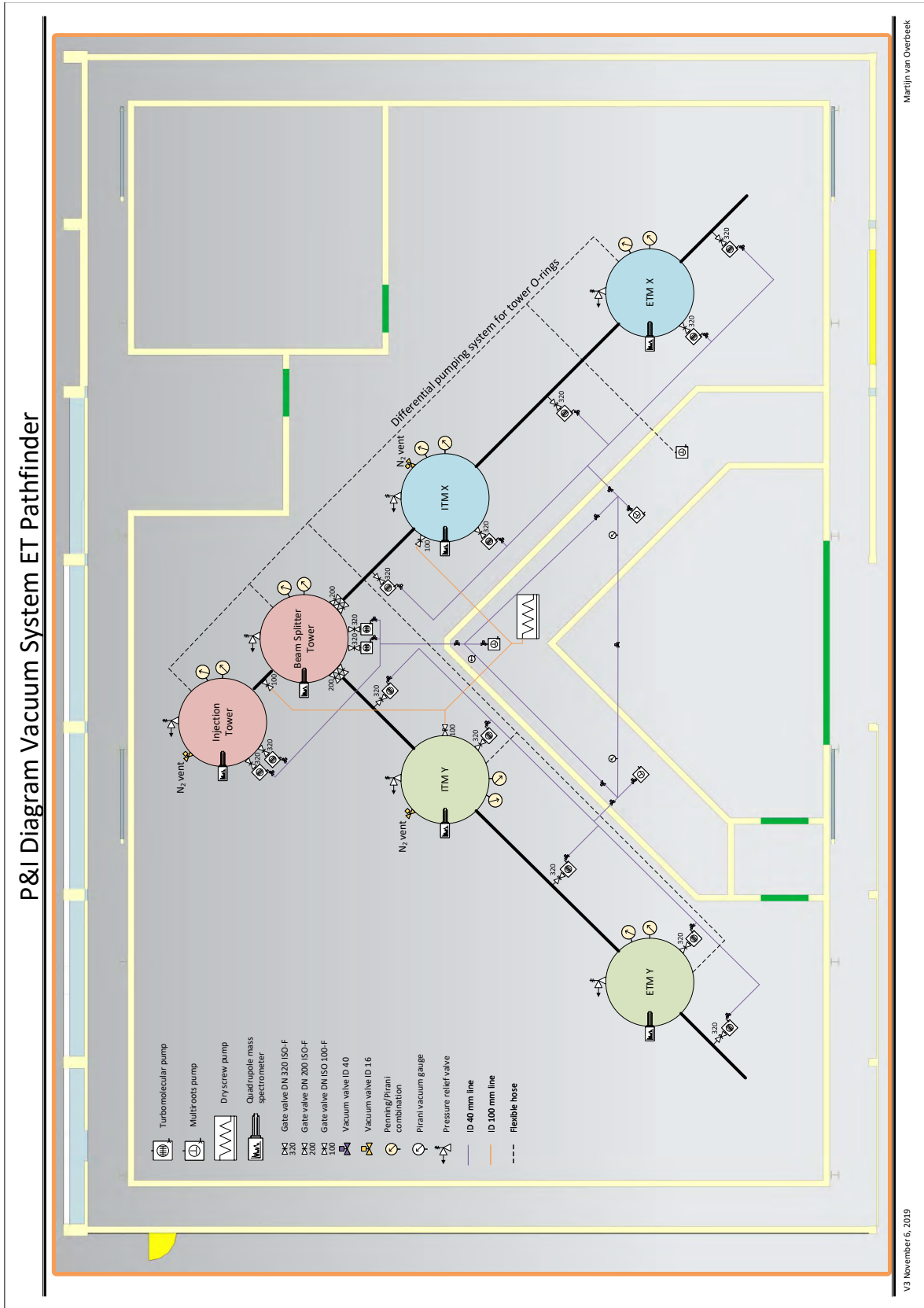


Figure 4.7: Schematic layout of the vacuum system.

separate the fore-vacuum beam lines for the turbodrag pumps and for the tower; for the screw pump we need a 100-mm diameter pipe whereas for backing the turbo pumps 40 mm seems sufficient. The advantage of using a smaller diameter pipe for the multi-roots manifold lays in the price of the valves; we save about 60 k€ on valves alone using smaller diameter pipelines. A fourth multi-roots pump is used to pump on the O-rings; we do not want to spoil the fore-vacuum of the turbo pumps by the gas load that we expect from the O-rings, and the extra pump makes partial venting (only one arm) easier. All forepumps are located outside the clean room in the yellow corridor in Fig. 4.7 (corresponding to the green area in Fig. 2.1); this helps for the room conditioning (especially the screw pump needs a lot of cooling power and produces acoustic noise). The connections between the flanges in between the O-rings and the manifold connected to the roots pump are constructed with flexible hosing; we investigate whether that also is desirable for the connection between the turbo pumps and the roots pumps or whether to use stainless-steel bellows. For pumping on the O-rings, the vacuum requirements are not as strict as for our primary vacuum. We need to disconnect all vacuum lines to the O-ring seals when a tower is opened. The turbo pumps are in the current design connected to the base of the tower or to the 800-mm arm sections, hence these connections can stay in place when the tower is opened.

Since for our application it is crucial to inspect the water vapor pressure, we also foresee one quadrupole mass spectrometer per tower. We need information on the partial water pressure to see when we need to regenerate the cryogenic shields and it is also very convenient to have these spectrometers in place for leak chasing and during bake-out. The vacuum system is so large and there are so many feedthroughs that it is desirable to have one quadrupole mass spectrometer present per tower, so that we can inspect the origin of leaks easily.

A breakdown of the costs of the main vacuum components is given in Table ???. This table does not contain the costs for services (cooling water, compressed air, power); that is considered part of the facility and comes from other funding. However, the costs for scaffolding and installing work platforms around the towers, which are needed for access to the equipment during installation and commissioning activities, are included.

The costs in Table ?? are estimated based on quotations from Pfeiffer and catalogues from VAT, and by scaling the production costs for the SBE- and the cryolink systems at Virgo and the multiSAS tower at Nikhef. For the mechanics and vacuum equipment, a EU-wide tender is required so the actual costs may obviously deviate, depending on the outcome of the tender. In this table, value-added taxes (21 %) is specified at the bottom.

Pump-down time and water vapor

For the layout described in this section, the predicted pump-down times have been calculated using the model of subsection 4.3.1. For laminar flow, the pump speed was determined by the volume of the system and the HEPTA screw pumping curve. For pressures below 1 Pa (10^{-2} mbar, the pumping speed has been calculated using molecular flow and the turbo pump outlets. The turbo pump has been modeled as an aperture with 75 mm radius, corresponding to about 2400 l/s pumping speed for water at room temperature. Molecules are generated at the walls of the vacuum system and are tracked until they pass a "turbo pump" hole. We assume 5 turbo pumps per arm and we modeled half an arm plus 1 end tower. Since we are interested in water buildup at the mirror and the vacuum conductance of the planned thermal shields, the vacuum system is split into 5 regions: region 1 is the region around the mirror and marionette inside the inner shield. Region 2 is in between the walls of the inner cryogenic shield. Region 3 is between the inner and outer cryogenic shields. Region

4 is between the walls of the outer cryogenic shield, and region 5 contains the full volume outside the outer (liquid nitrogen) cryogenic shield. The calculations start with saturated walls; the full mono-layer sticking to the surface needs to be pumped off. For the water mono-layer, we assume an average sticking time of 10000 seconds and a sticking probability of 0.2 for a depleted layer and 0.01 for a fully-occupied mono-layer. These numbers are consistent with 3×10^{-9} mbar l/s/cm² for initial pumping on a mono-layer. Also models with a range of binding energies for different sites on the lattice will lead to similar pump-down curves.

Fig. 4.8 shows the number of wall bounces for molecules from generation till hitting the pump. The average number of wall bounces equals 10,200 for molecules originating in volume 5 (the tower) and up about 11,800 bounces for molecules starting from in between the walls of the inner shield. Only 20 percent of the particles starting from the tower walls fly into the pump without crossing the thermal shields; those particles need on average only 1565 bounces. The average distance traveled by the molecules equals 10.8 km (an average flight time of about 18 seconds for water at room temperature). According to the simulation, the conductance from volume 5 to volume 4 is much larger than from volume 5 to the pumps, it is in the order of 20,000 l/s. This helps a lot in pumping down the water content from the mirror surroundings; the obstructions from the surrounding shields are not restricting the flow too much. When the thermal shields are cooled to liquid Nitrogen temperature or below, the shields act as a cryopump for water with a pumping speed in the order of 10^6 l/s. The vast majority of water vapor coming from the tower walls will freeze on the shields and does not reach the turbo pumps (or the mirrors).

Fig. 4.9 shows the pressure as function of time for pumping down this system, using the model for the mono-layer of water as described above. Note, that not all components inside the vacuum have been included in the simulation; the top stage, inverted pendulum, and part of the cryogenic leads were not modeled. Also, extra load from outgassing of cables etc inside the vacuum vessel was not taken into account, but water leaking through the Viton O-rings is included. A conservative total amount of 3×10^{19} H₂O molecules per m² for the full mono-layer was considered; a well-treated surface may contain less water. As can be seen, the screw pump can evacuate the tower to 0.1 mbar in about 1.5 hours, at which moment in the simulation the turbo pumps are added. The rapid decrease to 10^{-6} mbar then takes only a few minutes, at which time in our simulation the mono-layer of water is dominating the gas load. (In reality the decay will be somewhat more gradual since the transition from many water layers to a full mono-layer is more gradual than assumed here; in the simulation only the mono-layer has high binding energy. Nevertheless, experience shows that the evacuation between 1 mbar and 10^{-5} mbar with turbo pumps is indeed rapid; minutes not hours). At that time, in the simulation the temperature of the tower is gradually increased from 20 to 65 deg. C and the pressure rises since more water is coming off the wall. After about 9 days of pumping, the mono-layer of water is depleted by 3 orders of magnitude, the partial water pressure is below 3×10^{-8} mbar at 65 deg. C, and the heating is switched off, after which the remaining partial water pressure decreases with several orders of magnitude (since the sticking time to the walls increases) and the final pressure decreases to below 10^{-9} mbar when the tower is cooled down to 20 deg. C.

As can be seen in Fig. 4.9, without baking the partial water pressure will stay above 10^{-7} mbar for months and above 10^{-8} mbar for years.

As soon as the cryogenic shields are cooled down, the remaining water vapor will be collected on those shields and ice layers will build up; the first layer in a matter of minutes. After a month of cryogenic operation almost all water will have been collected on the cryogenic shields (since the pumping speed of the shields exceeds that of the turbo pumps, they will collect the water faster). The

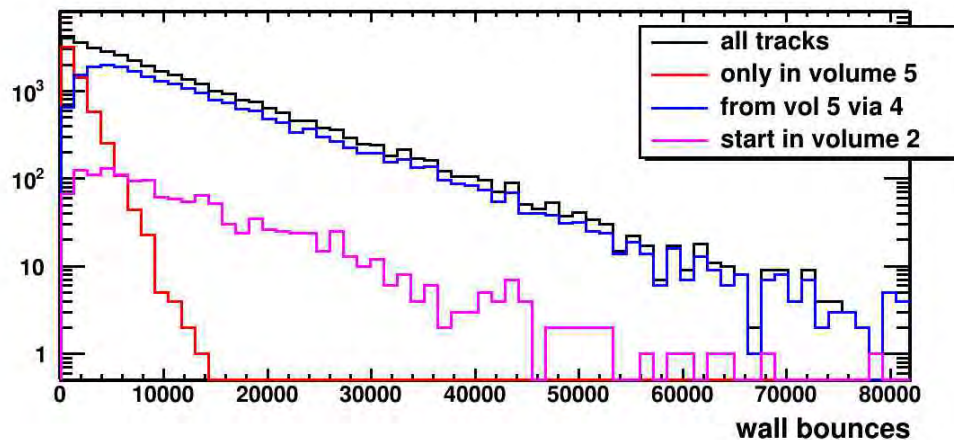


Figure 4.8: Distribution of the number of wall bounces for molecules coming off the walls inside the vacuum vessel (black). Subsets of the total are shown also: particles starting from outside the LN2 shield that do not pass the first wall (red), and that do pass the first wall (blue), and particles starting from the inner cryogenic shield (pink).

surface area of these shields amounts to about 10 m^2 , or about 5 percent of the surface area of the injection/beamsplitter towers.

For cryogenic operations, it is important to limit the amount of vacuum breaches; one can consider to bake the central towers every time after opening up, or one can hope that most of the ice buildup will be on the outer liquid nitrogen shield (but part of the ballistic flow will hit the mirror). A rough estimate would give that for every time opening up, about 30 layers of water will be grown on the liquid-nitrogen shield and about 1 layer on the mirror (from ballistic flow and from released water from the shields, which will bind the water less strongly for thicker layers of ice). Although the ice build-up after a vacuum breach is highly undesirable, we expect that the impact on the performance of the interferometer is manageable, since the speed of this build-up will be far below the conditions in KAGRA (see [9]; at KAGRA the partial water pressure at start cool-down equalled 7.9×10^{-6} mbar, whereas we aim for at least 100 times lower partial pressures around the cryogenic mirrors).

To reduce the amount of water collected by the towers after venting, one can consider venting with dry air or an inert gas; indicated in Fig. 4.7 are the venting valves. We would need about 8 50-liter bottles (200 bar) to vent 2 towers once, therefore currently we plan to use dry Nitrogen gas from the liquid Nitrogen storage tank at the facility; we should have ample gas there. The venting strategy still has to be designed and risk studies have to be evaluated; we currently assume that the volume of the clean room is large enough to accommodate opening the towers when they are filled with Nitrogen instead of air; oxygen levels may decrease by one percent or so.

4.3.3 Cryogenics

In our facility, we want to operate the mirrors at cryogenic temperatures. Initially we start at room temperature, then we aim for 123 K (Phase 1a), where the thermal expansion coefficient of Silicon equals 0. In the next step (Phase 1b), we will operate at temperatures below 20 K, where the dominant coating noise of the mirrors is reduced substantially. Cooling in the temperature range around 10

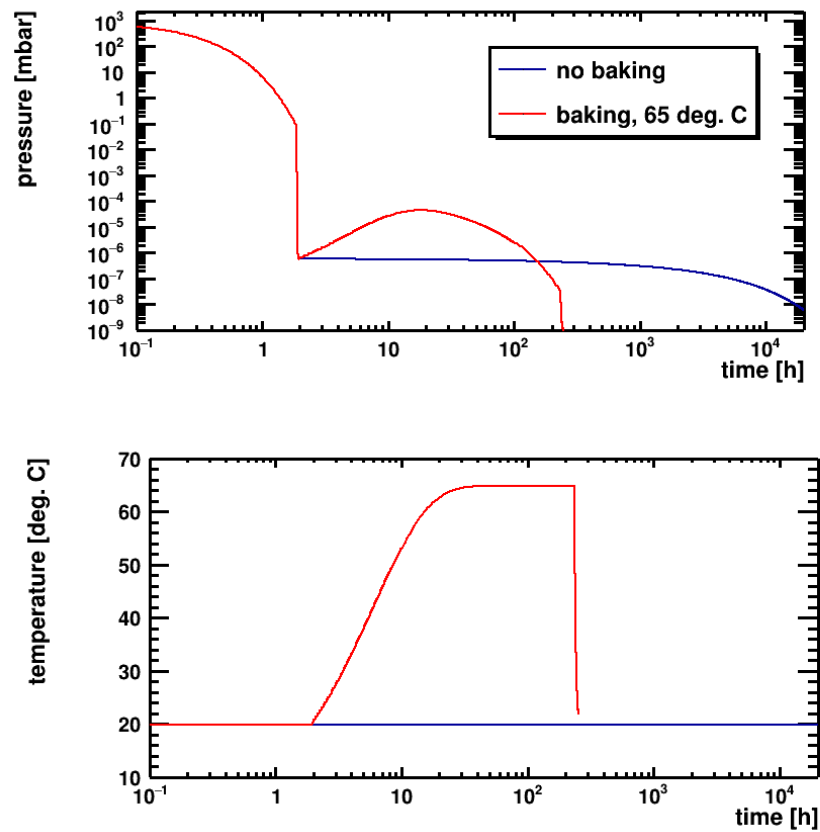


Figure 4.9: Pressure (top) and temperature (bottom) as a function of time after the start of evacuation, with baking (red) and without baking (blue).

K obviously requires He as a cooling agent, whereas cooling to 123 K can be obtained in many ways. Inside the vacuum vessel, the main heat loads come from thermal radiation. At an ambient temperature of 300 K, infrared wavelength of the radiation peaks at 10 μm and the incident power per square meter amounts to 460 W. The Carnot limit for an ideal cooling refrigerator determines the optimal limit for the ratio of effective cooling power dQ/dt and input power at the high stage as $\frac{dQ/dt}{P_{in}} = \frac{T_L}{T_h - T_L}$, or 0.015 for $T_h = 300$ K, $T_L = 4.5$ K; but in practice the best commercially available 2-stage pulse tube coolers need about 12 kW input power for a cooling power around 2W at 4.5 K (and around 60 W at 40 K in the first stage) and the efficiency is about two orders of magnitude lower. It is clear that radiation shields are needed; the thermal radiation on the mirror, marionette, and reaction masses without shields would exceed 100 W. Thermal radiation increases with the fourth power of temperature, so surrounding the mirrors by an outer cryogenic shield cooled to 80 K would reduce the heat load on the cryogenic parts inside this shield by more than a factor of 100. Also, using shields with low emissivity reduces the thermal radiation exchange between surrounding and shields. For an outer shield, cooled to about 80 K, we opt for a liquid Nitrogen cooling scheme. We have experience with similar systems (Nikhef designed and produced the Virgo cryotrap [10]) and liquid Nitrogen is very suitable to cool the massive amounts of heat. In equilibrium, the required cooling power at 80K equals about 200 W; that can be obtained by evaporating 4 liters of liquid N per hour. (Note, that we also use 2 passive radiative shields with low emissivity around the 80-K shields to reduce the thermal radiation load; in absence of these shields we would need about 500 W cooling power in equilibrium). Alternatively, a scheme with a cryorefrigerator *outside* the primary vacuum, and extracting heat via conduction, seems impractical for our facility. One of the best conductors, Copper, has a heat conductivity coefficient of $k = 400 \text{ Wm}^{-1}\text{K}^{-1}$, which implies that if one wants to extract 200 W via a 2-meter long Copper braids with a total mass of 200 kg, from the inside of the vacuum system to outside the tower, the temperature difference over the braid would amount to 89 K for our shields. One could try more complicated schemes incorporating heat links crossing the vacuum vessel, such as vacuum-sealed carbon fibers or heat pipes. Heat pipes may be a viable option but we did not have time to further explore that.

The thermal radiation from the liquid Nitrogen shield is still quite intense and it is desirable to have a lower ambient temperature around the mirror. A second thermal shield around the mirror is required to lower the ambient temperature around the mirror; this inner cryogenic shield could for instance be operated at 40 K. For a surrounding temperature of 40 K, the thermal radiation power in the enclosed volume equals only 0.14 W/m^2 and this can be considered a moderate heat load requiring moderate cooling power. Also, when the facility is operated at a mirror temperature of 123 K, the cooling can be provided by the outer 80-K shield and the inner shield can be heated and used to control the temperature of the mirror. When the liquid Nitrogen shield is cold, only a few Watt of heating power on the inner shields suffices to maintain the ambient mirror temperature at 123 K (and thus the liquid Nitrogen consumption does not rise noticeably due to this strategy).

Thermal Shields

Fig. 4.10 depicts the thermal shields around the mirror. Each shield is double-walled and contains holes to allow pumping. The holes are staggered, no direct line of sight through the holes is present. Of course, the laser beam, the marionette suspension wires, and the optical lever view ports require holes in the shields that give a direct line of sight to the room-temperature environment. It is imperative to limit the solid angle of these holes as much as possible. For the Einstein Telescope, which needs clearances of 0.5 m or more around the beam, thermal shields around the beam with a

length of about 50 m are foreseen (at both sides of the mirror). Here, we have much smaller beams and we can live with thermal shields around the beam with lengths in the order of 1 m. (these tubes are shown in Fig. 4.10). The amount of thermal radiation directly passing a cylindrical aperture of length l and inner diameter d scales as d^4/l^2 , so baffles are placed at the ends of the tubes with small diameter holes. Also, the emissivity of the shields is important. As mentioned, if the shields have an emissivity of 0, then all thermal radiation is reflected and in principle no cooling power is needed to maintain low temperature (the radiative heat input is zero). However, in that scenario also all radiation entering the holes can pass all through all walls via multiple reflections. Intuitively, it is clear that at least the baffles around the laser beam must be optically black at the wavelength of the laser; one wants to absorb any stray light around the beam. Here, we assume that these baffles also have high emissivity in the far infrared. Whether it is better to have parts of the shields also blackened (either for stray light or for absorption of thermal radiation), or whether one of the 2 walls of the inner or outer shield needs to be floating (thus not conductively cooled) is an open question that we want to answer by using model simulations (see Sec.4.3.1).

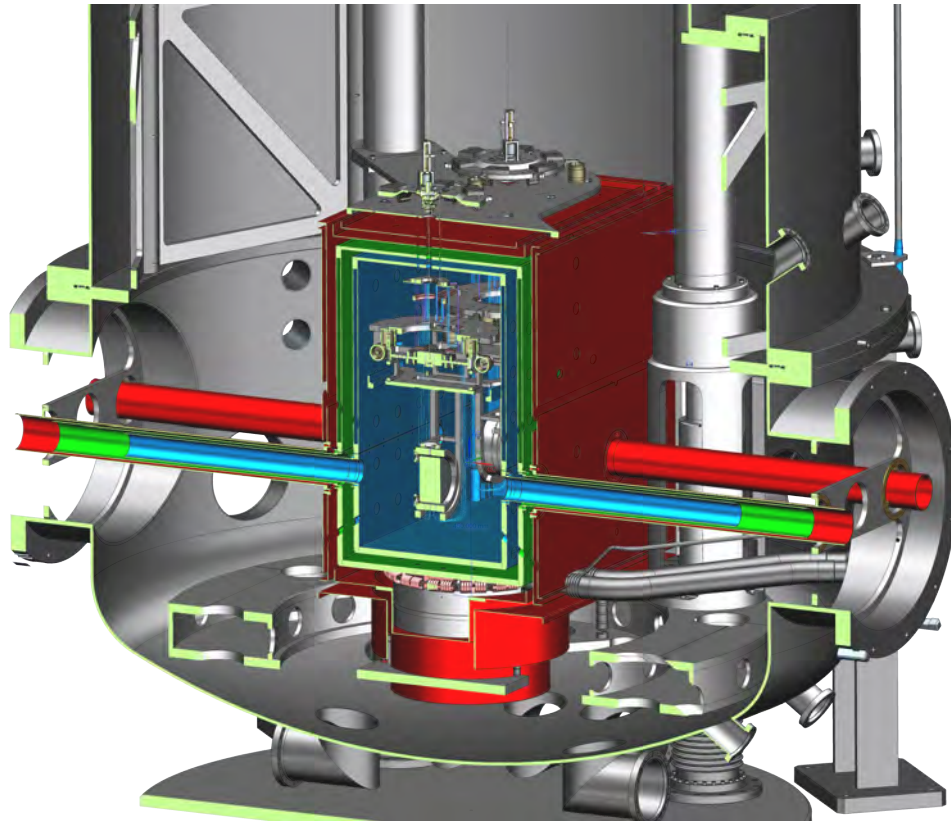


Figure 4.10: Cross section of a tower hosting the cryogenic Fabry-Perot cavity end mirrors. To cool the mirrors, marionettes, and reaction masses at the end of the inverted pendulum chain, three double-walled thermal radiation shields enclose the test masses. The inner shield (~ 30 K) is indicated in blue, the liquid N shield in green, and the outer floating shields in red. The tubes, extending from the shields around the laser beam, are connected to the shields and contain conical baffles (not shown) to block thermal radiation.

First calculations have been done, in which the thermal loads are calculated in equilibrium. In these calculations, it was assumed that the bottom of the 80-K cryogenic shield is kept to 85 K, that

the tower walls are kept to 300 K, that the bottom of the inner cryogenic shield is cooled to 30 K and the cold finger that cools the mirrors and marionettes to 12 K. We used baffles with an inner diameter of 30 mm inside the tubes around the beam line, and also baffles mounted on the reaction mass in front and behind the mirror. In this simulation, all Aluminum surfaces had an emissivity of 0.1, all stainless-steel surfaces 0.3, and the baffles 0.95. We also added baffles mounted on the reaction mass around the mirrors. The results of this particular simulation are shown in Fig. 4.11; in equilibrium, the heat load on the liquid Nitrogen sink equals 180 W, and the end temperature of the bottom of the shield (closest to the liquid Nitrogen vessel) is kept at 85K. Each tube connected to the liquid Nitrogen shield experiences a net heat input of 7 W, most coming from the baffle at the end. (Actually, the tube is cooled from the inside due to the colder inner cryogenic shield). The wall thickness of these tubes were chosen to be 2 mm, and the temperature gradient is sizeable. Also the thermal loads on the outer and inner walls of the liquid nitrogen shields is quite different. The liquid N shields and the inner shields are mounted on a frame with 4 rectangular support beams each with a cross-sectional area of 2500 mm²; still the top of the liquid Nitrogen shield reaches an equilibrium temperature of 117 K in this simulation.

The temperature gradients on the inner shield are much lower; mainly because the heat load is much lower. In total, the heat load on the inner shield equals 3.1 W in this calculation when the bottom is kept at 30 K, and the heat load on the cold finger equals 0.05 W at 12 K. The heat load on the mirror amounts to only a few mW; in equilibrium the temperatures of the mirrors, marionettes, and reaction masses are very close to the temperature of the cold finger. According to this simulation, shortening the inner tubes around the laser beam helps a lot in reducing the total radiative load on the inner thermal shields; about 0.7 W can be gained by such a simple measure.

These are very preliminary results. We used these results to design the Liquid Nitrogen cooling, necessary in the first stage of ETpathfinder, and to get an estimate of the cooling power needed for operation in steady state with mirror temperatures around 10-20 K in the second stage. The simulation package has only recently been upgraded to also simulate the time-dependent heat transfers and cooling powers and now, many more calculations are needed to optimize the design for the second stage of ETpathfinder, where the interferometer will be operated with test masses cooled to 10-20 K.

Liquid Nitrogen

The ET pathfinder facility will host a 15,000 l liquid Nitrogen vessel that can be filled on a weekly basis. This is part of the facility infrastructure and is not described in this section. Liquid Nitrogen can be transported into the clean hall towards a phase separator that is located in close approximation to the tower that hosts the cryogenic shield. This phase separator is used to lower the level of the liquid; the boiling temperature depends strongly on the pressure and a high column of liquid leads to a high boiling temperature at the bottom. We assume that heat leaks in the transportation from the outside to the phase separator lead to a consumption of 1 l of liquid Nitrogen per hour. The phase separator, that cools the liquid to the boiling point at atmospheric pressure, also consumes about 1 l of liquid N per hour. We assume that the shields consume about 4 l/h, for an effective cooling power of 200 W at 80K on the liquid N shield.

The total mass (inner and outer shields, payloads) that need to be cooled down from 300 K to 80 K amounts to about 350 kg (almost all aluminum), so about 60 MJ of heat needs to be cooled away; this is equivalent to the latent vaporization heat of 300 kg (400 l) of liquid Nitrogen. Therefore, during equilibrium we foresee a liquid Nitrogen consumption of about 6 l/h per cryogenic tower, so for 2 cryogenic arms about 580 l/day. For initial cooldown we need more cooling power, an

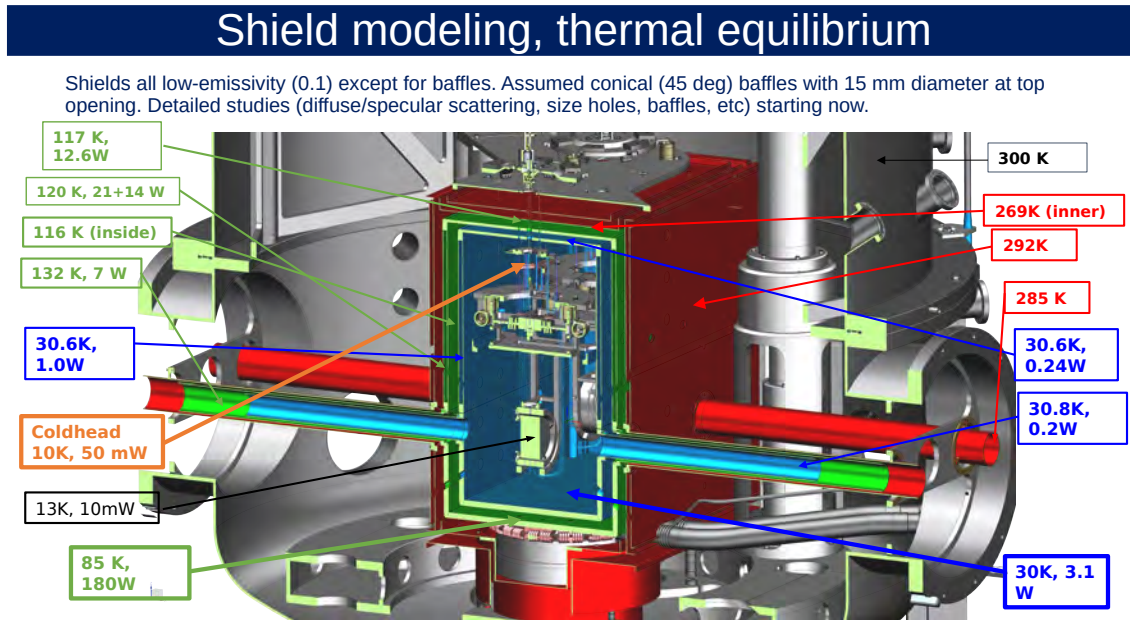


Figure 4.11: Preliminary results on the temperatures and heat loads in thermal equilibrium. Red: floating shields. Green: liquid nitrogen system. Blue: inner, He-cooled system (30K) Gold: cold finger, heat sink at 10 K.

additional 2000 l of liquid Nitrogen is needed to cool down the shields, the LN2 vessels, and the cryogenic test masses from 300 K to 80 K. The storage vessel will have some losses too, typically 0.5 percent per day. A 15,000 l storage vessel should be sufficient to last 1 week between refills (with a safety margin of a factor of 3).

Although we have ample experience with liquid N from the Virgo cryolinks, there are a few techniques that we want to test for ET pathfinder before finalizing the cryogenic design. One idea is to coat the vessel on the inside with Teflon, that should reduce bubble formation at the walls. Another idea is to cool the liquid N inside the vessel to below boiling point, by immersing a spiral with a small aperture and pumping on it. The evaporation then takes place in the spiral and the liquid is cooled via heat exchange with the spiral. Both these techniques would lead to less vibrations than an uncoated bubbling vessel but we need measurements to verify our expectations and also to monitor and demonstrate the actual cool-down curves. However, we cannot delay the ETpathfinder timeline for ordering the mechanics until after we produced test results for the liquid Nitrogen cooling scheme.

We expect that the current design of the vessel already to reduce vibration levels already to far below the ETpathfinder noise curve, since we expect little mechanical coupling and little scattered-light contributions from the LN2 shields. Fig. 4.12 shows the design of the LN2 vessel. The vessel will be made of Aluminum 6063, which has a high thermal conductivity (about $250 \text{ Wm}^{-1}\text{K}^{-1}$ at 100K). The density of liquid Nitrogen is 693 times higher than the density of the gas at room temperature. Therefore, we need wide outlets. In front of the outlet a sintered bronze vapor limiter is positioned; we want to avoid liquid droplets being sucked into the exhaust. The total volume of the vessel equals 40 l (but typically we want to operate with a low level of liquid, to reduce noise from bubbling). Nevertheless, the vessel must be able to withstand 700 bar pressure and for that reason it

is bulky and will be machined from a block of aluminum. We do not think it likely that a condition can occur in which the liquid nitrogen flow is blocked and pressures of several hundred bar build up inside the vessel. Even so, if all the liquid Nitrogen is evaporated and released inside the tower/arm, the pressure in the tower could increase by about 0.4 bar. The tower contains pressure relieve valves (that protect against unforeseen mistakes during venting the system) but will also contain rupture disks, as (redundant) fail-save safety procedure.

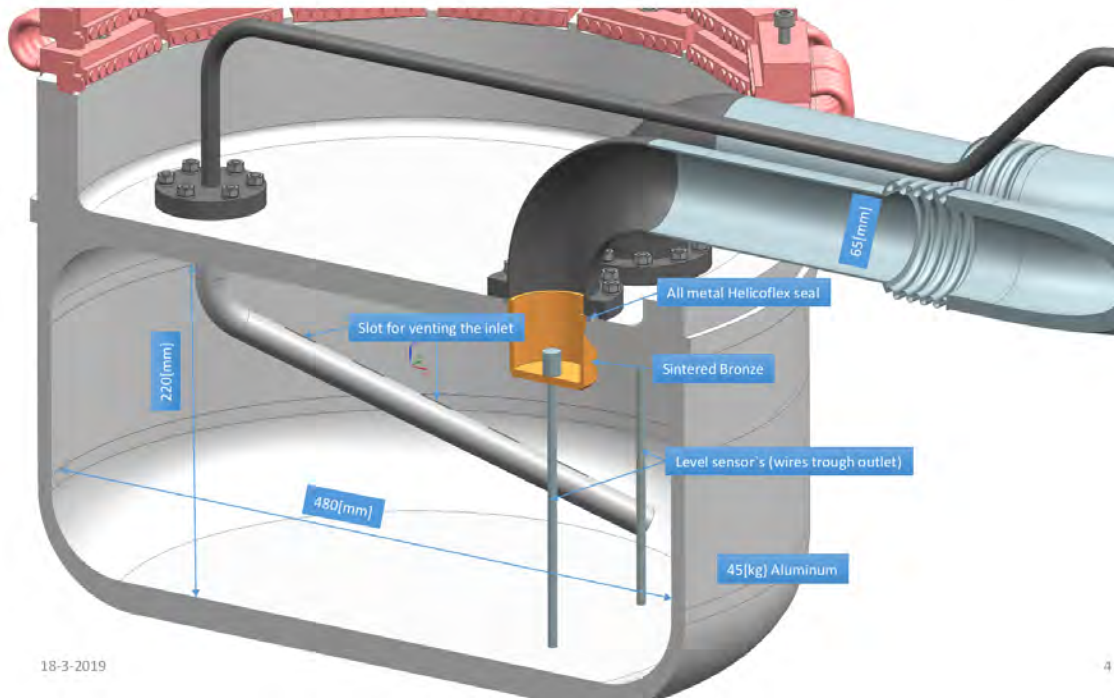


Figure 4.12: The liquid Nitrogen vessel that cools the cryogenic shields.

The inlet LN₂-transfer line contains slots at the top, so that when part of the liquid is evaporated by heat input in the transfer line, the excess gas can escape to the part of the vessel that is above the liquid level; no pressure can build up in the transfer line and no bubbles will travel through the transfer line. We plan to connect the LN₂ vessel directly to the bottom of the thermal shield (via an Indium contact). The top part of the vessel can be bolted off, so we can at a later stage change heat exchangers or level sensors if needed.

When cooling down, the shields will shrink several mm. Flextures are needed to compensate that movement. Details of the flextures on which the cryogenic shields rest are shown in Fig. 4.13.

Note, that we assume that the cryogenic shields are well outside the acceptance of the beam. We foresee baffles stopping the thermal radiation with apertures more than 10 times the radius of the beam. Also the minimal angle for scattered light that hits these apertures exceeds 1 mrad, 10 times larger than for the baffles at Virgo and LIGO. Since for small scattering angles θ , the probability density function for scattered light increases as $(1/\theta^2)\sin\theta d\theta$, we expect much less scattered light contributions from the shield in ETpathfinder than from the baffles at LIGO/Virgo. Therefore, we do not try to seismically isolate the shields from the ground.

In this design, we transport cryogenic liquids and gases from outside the towers hosting the FP-

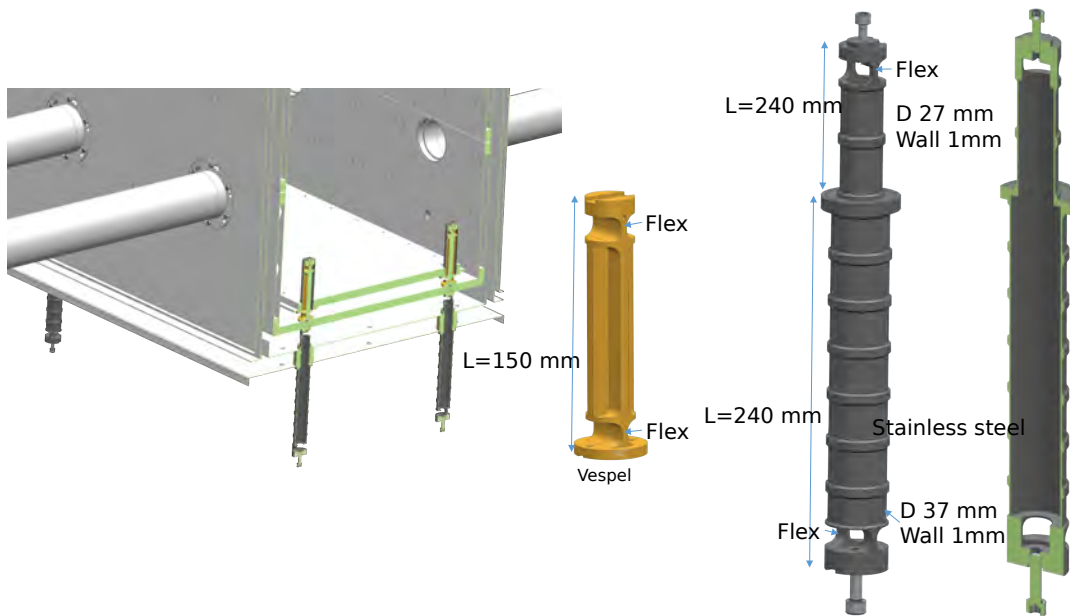


Figure 4.13: The flexures that support the cryogenic shields and allow for shrinkage. The flexures are oriented perpendicular towards the center of the base plates of the shields. The shields are mounted to the floor of the tower.

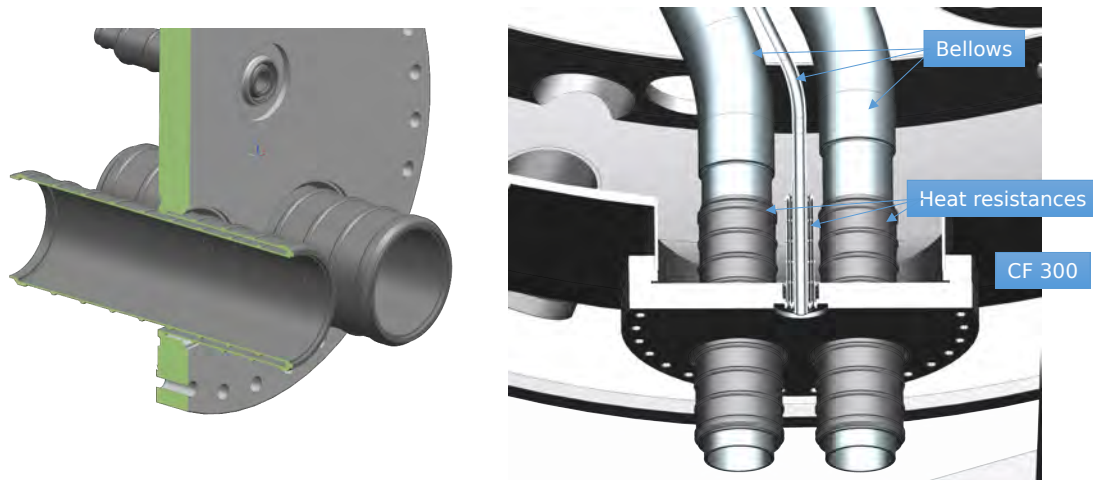


Figure 4.14: The 300-mm iso-CF flange for the inlet and outlet of the Nitrogen through the vacuum tower wall. The double-walled stainless-steel bellows are used as heat resistance.

cavity to inside the tower. Thermal conduction to the tower walls need to be minimized. Therefore, we use long bellows of stainless steel, as shown in Fig. 4.14. In case of the inner cryogenic He shields, double-walled pipes are used in which the high-pressure inlet is inside the low-pressure, cold outlet. In all cases, we can use MLI foil around the cooling-agent leads that enter from outside, as long as these foils are shielded from the primary vacuum (i.e. they are wrapped around tubes but sit inside a bellows, inside the secondary vacuum of the cryogenic cooler and not in contact with the primary vacuum surrounding the mirror).

Fig. 4.15 schematically shows the liquid Nitrogen levels. If the level of the liquid Nitrogen in the storage vessel outside the building is much higher (e.g. 10 m above the suspended mirrors) then the pressure exerted by the column of liquid increases the boiling temperature of the liquid Nitrogen at the bottom of the vessel by a large amount (in the order of 10 K). The phase separator tank provides a local storage of liquid next to the tower with a lower level; the liquid is cooled to 77 K inside the phase separator (the boiling point at 1 bar pressure) and the vibrations involved in this cool-down take place in the phase separator instead of in the vessel in the tower. For the cryolinks at Virgo, the phase separator consumes 1l/h of liquid Nitrogen, whereas the cryolinks have a cooling power of about 300 W. We will use cryolinks and heat exchangers of similar capacity in ETpathfinder.

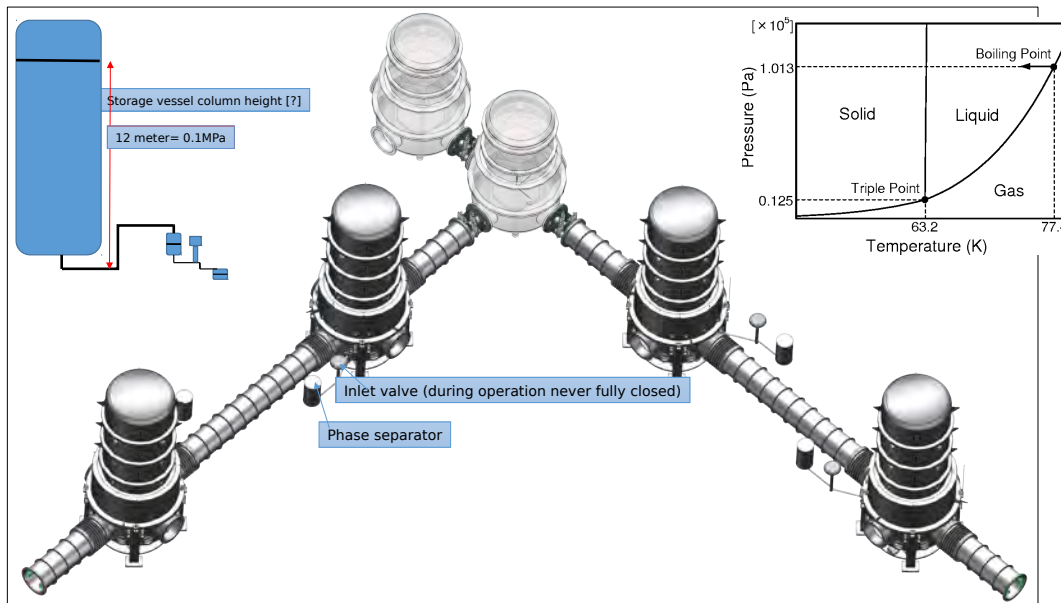


Figure 4.15: Overview of the liquid Nitrogen levels in the external storage and phase separators. The inset shows the phase diagram relating the boiling point temperatures and pressures.

For the liquid Nitrogen part of the ETpathfinder project, we want to test the amount of vibrational noise induced by the vessel, we want to test the Teflon coating inside the vessel, and the use of a spiral as heat exchanger. This is a project that we will conduct in collaboration with the university of Twente, but for which both funding and Ph. D.-student manpower still have to be found. Currently we consider Nikhef, Maastricht, or Twente as the host of the prototype; we still need to locate funding and lab space for a prototype setup. This prototype is quite essential; we also need it to measure the performance of the inner cryogenic cooling system and measure the temperature of the

mirrors and marionette, etc. We cannot mount a temperature sensor on the mirror or marionette in the ETpathfinder facility, as it would induce extra noise, so we want to be able to test and measure these parameters using a dummy mirror in a test setup.

Cooling below 70 K

The design for the cooling of the inner shield and the mirrors and marionette's is only in a conceptual stage. We aim to avoid using pulse tube coolers (or even worse, Stirling coolers) since they exhibit spikes in the gas pressure in the order of 20 bars during the cycle, at a repetition rate of 1-2 Hz (or even higher).

The KAGRA collaboration completed first successful cryogenic operations last year [11]. They developed, together with Hitachi, a pulse tube cooler that shows minimal vibrations (see [12], [13], [14]), by having a long duct. Still, the higher harmonics of the vibrational peaks at the frequency of the cooler cycle limit the operation of the facility (see the projected noise in Ref. [15]) and KAGRA currently tries to include better heat links to shield from this noise. Furthermore, we want to avoid ice build-up on the mirror, that is hampering KAGRA [9]. Therefore, we need a design that avoids MLI foil around the mirror region and that does not use a multistage cryocooler in which the first stage cools the thermal shield and the second stage the cryogenic test mass; we wish to keep the mirror warm during cool-down of the thermal shields.

Our proposed alternative is based on sorption coolers. The Energy, Materials and Systems (EMS) group of ter Brake at University Twente produced sorption coolers for many experiments, including the infrared camera's in the Darwin space telescope mission [16] and the METIS instrument at the E-LT telescope in Chile [17, 18]; this last experiment is resembling our cooling needs closely.

For the Darwin mission, a cooler has been produced that keeps the temperature stable (at 4.500 K) within better than 1 mK over hours of time, whereas the pressure ripple on the high pressure inlet (at 16.5 bar) was smaller than 0.01 bar, with a cycle period of about 10 minutes. The sorption cooler produced forces on the test mass with an amplitude spectral density of less than $1 \mu\text{N}/\sqrt{\text{Hz}}$. In this experiment, the temperature stability of the infrared camera was of paramount importance; so that was the parameter that was stabilized.

For the ground-based METIS instrument at the E-LT telescope facility, the requirements are that the LM-band imagers need to be operated at 40 K (cooling power 1.4 W), the N-band imager at 25 K (cooling power 1.1 W), and the N-band detector at 8 K (cooling power 0.4 W). These requirements are in the same range as the requirements for ETpathfinder, so we believe that a similar sorption cooler would be the optimal cryostat for gravitational-wave interferometers.

The proposal to use sorption cooling for the Einstein Telescope was presented by M. ter Brake at the Einstein Telescope conference in Hannover in 2013 [19], the description and principles are given in this presentation. We adopted this proposal and want to develop a sorption cooler for ETpathfinder.

In a sorption-based cooling cycle, the gas is adsorbed in an atomic roster, in our case Carbon. At low temperatures, graphite can absorb enormous quantities of He gas (close to fluid density). In the sorption cells of EMS-Twente (Fig. 4.16, courtesy of M. ter Brake), graphite pills are stored in a cylindrical gas reservoir. Inside the cylinder, graphite pills are stacked around a heating wire. The heat sink is made of a copper block around the gas reservoir; the block and reservoir are separated by a small volume in which gas can be pumped in and out; in this manner a switchable heat link between reservoir and sink can be made. The storage cell is connected via one-way microvalves that open if the pressure is above the switch point.

At the start of the cycle, the storage cell is cooled and the gas is adsorbed in the Carbon; the

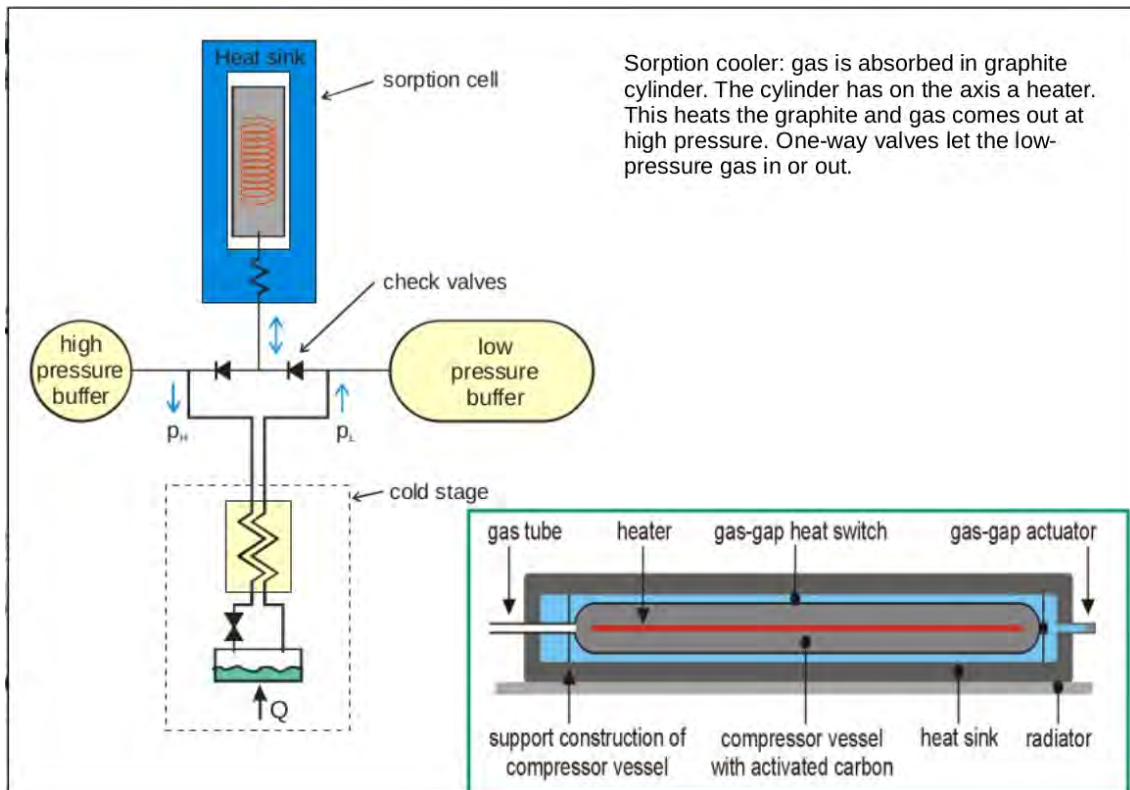


Figure 4.16: Scheme of a sorption-cell compressor. Courtesy to H.J.M. ter Brake [19].

pressure drops. The valve connected to the low-pressure reservoir opens and the storage cell is filled. When enough gas has been buffered, the thermal switch is closed (the gas between the heat sink around the storage cell is pumped off) and the central heating wire is activated. The temperature in the Carbon rises and the He gas is pushed out. Since the heat from the wire is slowly traveling outwards in the carbon, the He-gas pressure build-up is gradual. When the pressure in the cell is above the high switch point, the microvalve to the high-pressure reservoir opens and the gas is flowing from the storage cell into the high-pressure transport line towards the Joule-Thomson restriction where the test mass is cooled down. When the storage cell is getting empty and the pressure in the storage cell drops below the high-pressure setpoint, the one-way valve at the high-pressure side closes, the thermal switch is activated, the storage cell is cooled and the next cycle starts with intaking gas from the low-pressure side. Typically a cycle lasts for 100 seconds or so; having several cells operating and connected to the same buffers around the Joule-Thomson restriction allows for very continuous pressure levels at the test mass (the ripple in the pressure is about 4 orders of magnitude less than that in a pulsetube cooler, and at two orders of magnitude lower frequencies. We expect that the vibrations of the cold finger are completely dominated by seismic noise and the transfer functions of the support, and that the gas-induced pressure spikes introduce negligible extra noise; i.e. forces on the cold finger at the $fN/\sqrt{\text{Hz}}$ level above 10 Hz.

In case of the METIS instrument in the E-ELT, cooling powers at different temperatures were needed for different instruments. Since sorption cooling for Helium is very efficient when the temperature of the heat exchanger in the cell is below 20 K, but quite inefficient at 70 K, thermal reservoirs and heat-exchange steps were needed; a Neon stage to lower the temperature and provide cooling power at 40 K, 2 hydrogen stages with thermal reservoirs at 25 and 15 K, and the ultimate He stage at 8 K. Temperatures, cooling powers, and heat exchangers as employed in the METIS detector are shown in Fig. 4.17. The cooling bus that provides the heat sink at the high end of the instrument is made from liquid Nitrogen. By far the most cooling power is needed to pre-cool the He since the starting temperature of the LN2 bus is high, too high for efficient adsorption of He gas. Much more cooling power around 10 K could be obtained if the sorption cell was pre-cooled via other means to a temperature of e.g. 40 K. Instead of a liquid Nitrogen bus to cool all sorption stages, as used in the METIS detector, we also study the possibility to use a pulse tube cooler to deliver the high-temperature heat exchanger for the Helium sorption cells. This has the disadvantage that a noisy device is active inside the building, but since the pulse tube coolers can be placed outside the clean room and are only cooling the heat sink at the high-temperature end of the sorption cooler (which is located in its own vacuum system, outside the towers hosting the arm cavity mirrors), the vibrational transfer to the cold reservoir inside the ETpathfinder vacuum system is much less than in schemes where the pulse tube cooler directly cools the cold cryogenic screens or the mirror suspension. An alternative for using sorption cells to drive the refrigerant is using a Joule-Thomson cooling cycle with a pump that circulates cold gas at high pressure (replacing the sorption cells); the EMS group in Twente also has experience with that scenario. According to them, that scenario would not need prototyping even, whereas the sorption scheme is more complicated and requires further research.

For the ETpathfinder experiment, we intend to try sorption cooling and demonstrate that this is the superior technique for use in future third-generation gravitational-wave interferometers. This is a technically challenging project and we need to design and test several steps with prototypes. From our initial calculations we expect that we need about 3 W cooling power at a temperature of 30-40 K for the thermal shields (and to sink heat for the He that is used in the cold step) and much less, in the order of 0.1 W, at 8K. Scaling from the METIS experiment, that would require around 400 W cooling

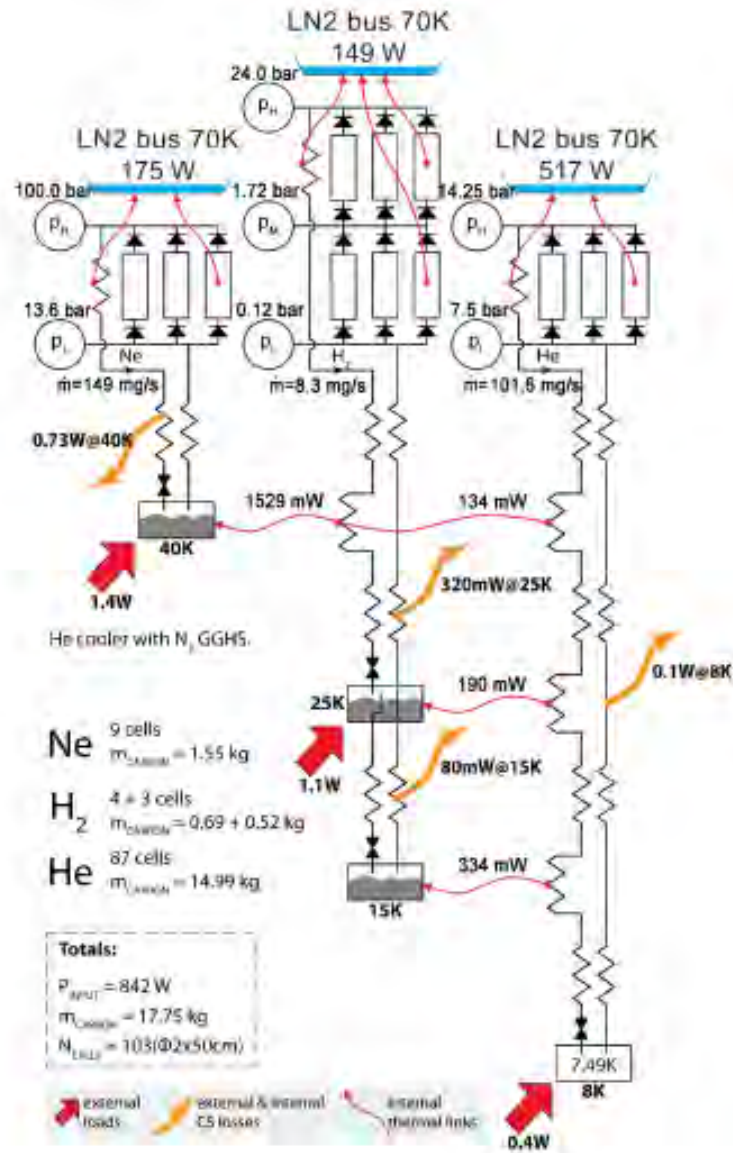


Figure 4.17: Cooling scheme for the METIS instrument. The different heat loads, pressures, heat exchangers, and gases are indicated. Figure from [17].

power at liquid Nitrogen temperature. Alternatively we could use a pulse tube cooler to pre-cool the cold reservoirs, and then around 20 W cooling power at 40 K would suffice. Our design is still very premature and conceptual; we want to keep the flexibility to use an ordinary Joule-Thompson scheme for the thermal shields (pumping around pre-cooled gas where the gas is cooled outside the ETpathfinder vacuum by a pulse tube cooler) so in the proposal we reserved 4 pulse tube coolers (one per tower) to provide pre-cooling, consuming 12 kW of electrical power and needing 30 l/min of cooling water. Furthermore, pulsetube coolers are more efficient and it might be necessary to initially cool the thermal shields from 300 K to 40 K using a pulsetube cooler; and maybe switch it off and use a sorption cooler during measurements to maintain the shield temperature. Also, for the sorption schemes, different gases and mixtures can be used; see e.g. [20]. This needs further exploration.

4.3.4 Thermal links

The mirror, reaction mass, and marionette are very well isolated from seismic vibrations but in order to cool these parts down below 100 K, heat transfer via thermal conduction is necessary. Care must be taken to minimize extra vibrational noise from thermal links. In our scheme, we connect the cold finger (the lowest-temperature heat link) to the bottom of the inner cryogenic shield. The level of vibration of that cold finger will be at least as much as the ground; the supports are not damping ground motion. We expect that the cooling of these links do introduce less noise than the level of seismic excitations of the ground, but that needs to be measured and demonstrated as part of the ETpathfinder research program. The cold finger will end into 2 rings, one for each of the 2 Fabry-Perot mirrors present in each cryostat during Phase 1a/1b. The connection between these rings and the platform that cools the reaction mass and marionette is made by a first jelly-fish construction of ultra-pure Aluminum wires. This Aluminum has a heat conductivity of about $20 \text{ kWm}^{-1}\text{K}^{-1}$ at temperatures of 10 K and below and several $\text{kWm}^{-1}\text{K}^{-1}$ even at 20 K. In equilibrium, with the mirror, marionette, and reaction mass at temperatures around 10-15 K, these links should transfer about 100 mW of heat (see the calculations in this section above); even a small number of thin wires suffice. The first cold platform is supported from the reaction mass chain, hanging from the last GAS filter above the thermal shields. From this cold platform, jellyfish connections are made to the reaction mass and to the marionette, again from ultrapure Aluminum wires. Therefore, the transfer of vibrations from the cold finger to the marionette will pass through 2 jellyfish stages and vibrations will be strongly damped.

The mirror is then cooled through the monolithic suspension; the monolithic silicon wires (that still must be developed, also for Einstein Telescope) also have $>10 \text{ kWm}^{-1}\text{K}^{-1}$ heat conductivity. Note, that in absence of the monolithic suspension, the mirror can only be cooled radiatively, so a program with silicon mirrors as cold as 10 K (Phase 1b) requires the development of monolithic silicon suspension.¹

An overview of the design of the suspensions is shown in Fig. 4.18, where the jellyfish wires are drawn. Details of how these are mounted to the reaction chain and marionette are shown in Fig. 4.19. In this figure, the cryogenic shields are not shown.

The mechanical transfer function of the jellyfish connections will be measured in a test facility at Nikhef; the layout of the test setup is shown in Fig. 4.20. The vacuum parts and suspensions for this test setup have been designed and the first parts have already been produced by the mechanical workshops of RWTH Aachen; the vacuum vessel is already installed.

¹For the first phase we only have to cool the mirror to 123 K and that can be done via the normal suspension and

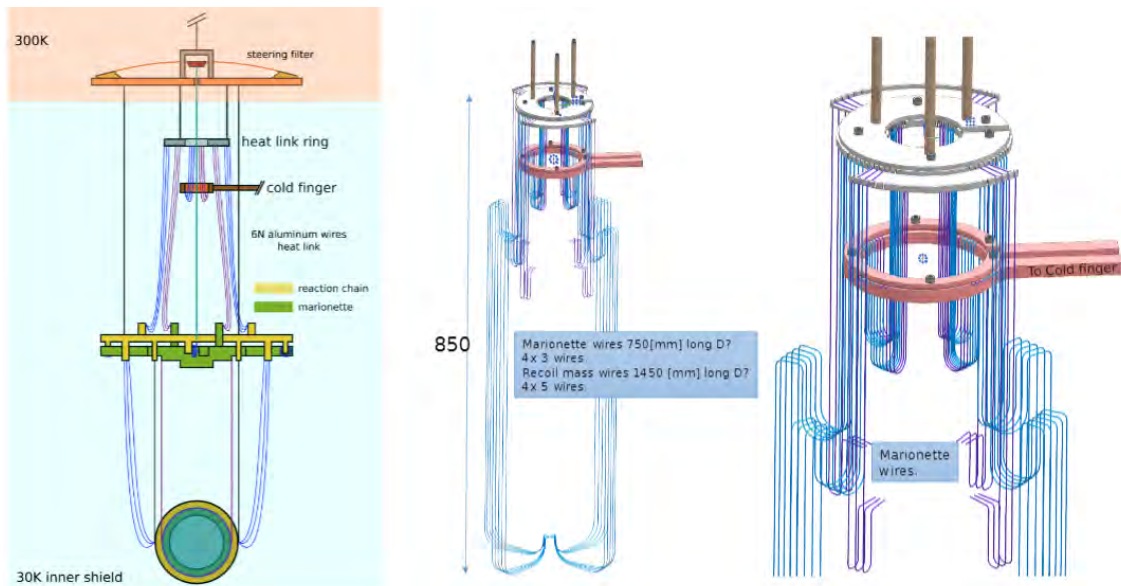


Figure 4.18: Layout of the thermal links (jellyfish connections) to cool the suspended test masses.

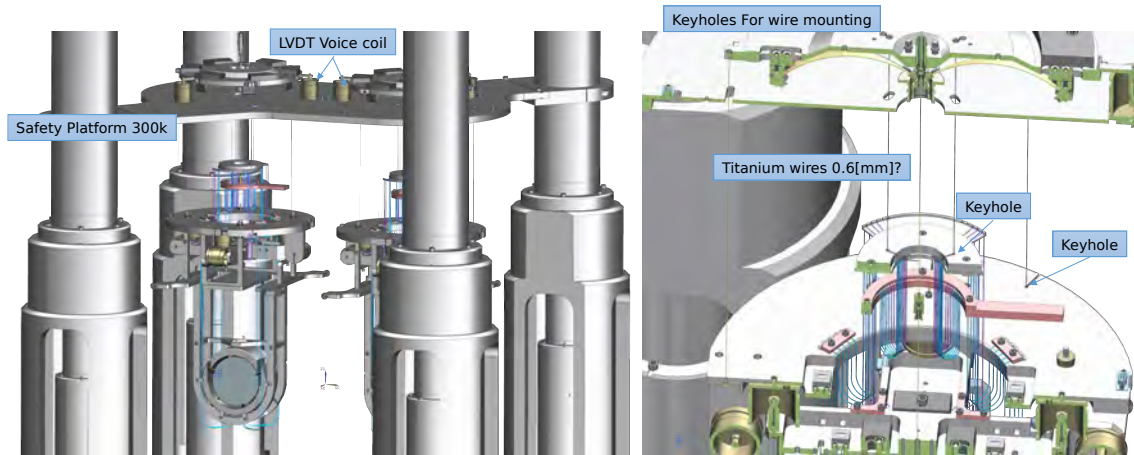


Figure 4.19: Overview of the thermal links between the cold fingers, the supported cold platform (the aluminum ring above the cold finger), and the reaction mass and marionette system. The mirror is cooled via a monolithic suspension connected to the marionette, the reaction mass around the mirror is cooled via the reaction mass of the marionette.

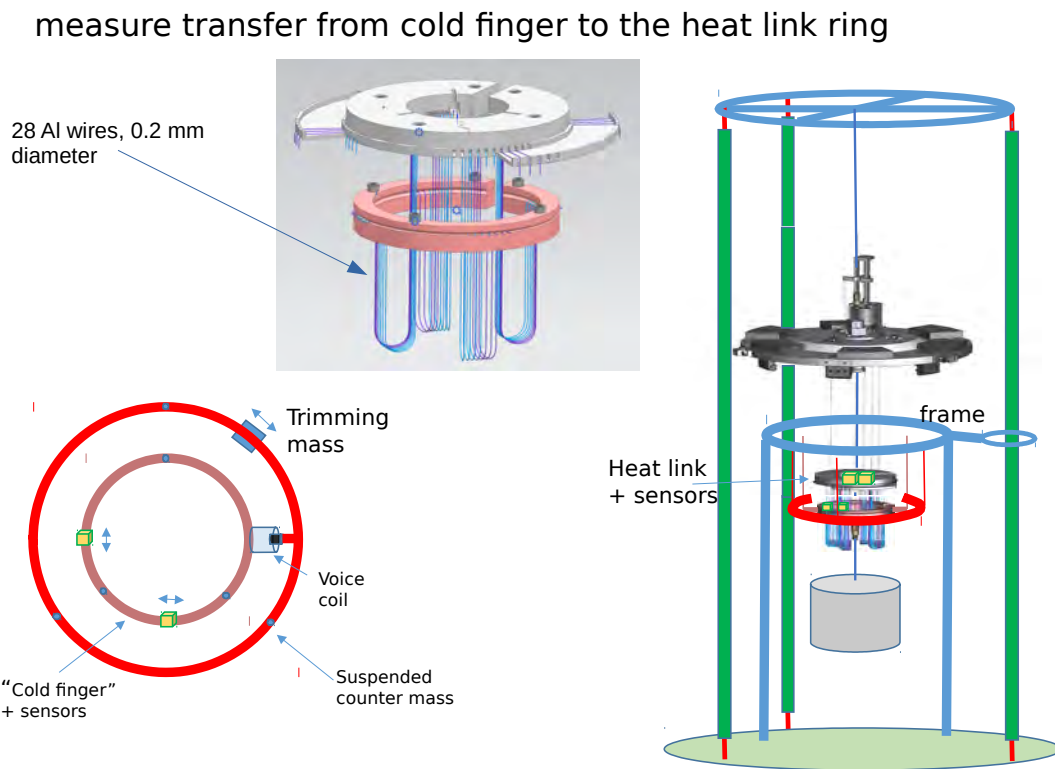


Figure 4.20: Test setup to measure the transfer function for vibrations from the cold finger to the cryogenic support platform by the jellyfish connection that we foresee for ETpathfinder. Wire diameter is still to be determined.

4.3.5 Initial Cool-down calculations

Since January 2020 we upgraded our simulation package to the level that time-dependent heat transfer calculations can be done. Conductive heatflow between all elements are calculated from the center of one element to the center of the connected element, by calculating the average cross-sectional area and path length and integrating over the conductivity as a function of temperature along the path. At a given time, the sets of coupled differential equations describing conductive and radiative heat transfer are calculated and the heat stored in all elements is then numerically integrated in time. This turned out to be numerically quite challenging; especially since the heat capacity of the jellyfish wires and monolithic suspensions is very small and the conductivity at low temperatures very high; small differences in end temperatures lead to large fluctuations of heat flow. Finally for the jellyfish wires we ignored the heat inside the wire and calculated the transfer, assuming that as much heat flows in at one end as is extracted at the other end. Under these conditions, we can simulate a simplified model - containing 350 bodies to describe the tower, arm, thermal shields, marionettes, mirrors, jellyfish connections, reaction masses and baffles, but ignoring details in shape for e.g. IP legs, the top filters, the turbo pumps, etc. We model the towers and the arms as cylinders - for 1000 hours of cool-down time in about half a day CPU time. (For radiation, that includes 1 emitted photon per mm^2 for the full surface, about a 150 million tracked thermal photons). In order to describe the heat flows and body temperatures correct to the ppm level, a sixth-order adaptive Runge-Kutta scheme was necessary; using up to sixth-order time derivatives allowed for stepsizes in the order of 1 second. A real finite-element model based on the 3D-model of the design drawings would be nice to obtain, but it was expected that such a model would not be capable of performing these calculations in a timely manner; quite some effort has been put in the numerical stability, accuracy, and speed in our custom-made code.

Since the code was debugged and verified only recently, we include only 1 calculation in this version of the ETpathfinder design document. In this calculation, we start with the bottom of the liquid-Nitrogen shield cooled to 77 K and we assume that enough liquid Nitrogen is flown to maintain that temperature; all other bodies have a temperature of 300 K. Furthermore, for the inner cryogenic parts, we assume that we develop a cryocooler (sorption cooler) that is capable of cooling 3 W of heat when the heat exchanger (the cold finger or the bottom of the 10-K shield) has a temperature above 30 K, and of 0.2 W of cooling power between 10 and 20 K. We assume that the cooling power at 8 K equals 0 W and that it varies linearly with temperature between 8 and 10 K and between 20 and 30 K. Such cooling power may not be realistic, but these calculations serve to determine the design of the sorption cooler. We know from the static equilibrium calculations that we need about 0.1 W cooling power at 10 K and 3 W at 30 K and here, we want to see how fast the system cools down when starting from 300 K and using the cooling power that we need in the final equilibrium condition.

All aluminum surfaces except for the baffles (the shields, marionette, and reaction masses) were assumed to have an emissivity of 0.1. Lower emissivities could be obtained by polishing, but it is expected that we would prefer more diffuse surfaces in view of parasitic beams from scattered light. The baffles (around the mirror and in the pipes surrounding the laser beam) are assumed to be coated and having a emissivity of 0.95. Note, that it might be possible to have an efficient anti-reflective coating at the laser light frequency and a lower thermal emissivity; or even a thermal emissivity that is lower at 300K than at 10 K; in this calculation a constant emissivity for all wavelengths is assumed,

radiative cooling.

and the same emissivity for the laser beam and for thermal radiation. All stainless-steel surfaces were assumed to have an emissivity of 0.3. However, since we expect that cool-down is very slow and that radiative heat transfer might help, we also performed a calculation in which the bottom of the 10 K shield (both sides) and the bottom of the liquid Nitrogen shield (top side, facing the bottom of the 10 K shield) had an emissivity of 0.9 (such an emissivity should be provided by a vacuum-compatible coating). Also the marionette and the reaction masses in mirror chain 2 were assumed to have an emissivity of 0.9. This served to inspect how higher emissivity impact on initial cool-down speed and final equilibrium temperature; the majority of the heat is cooled radiatively. For the monolithic suspension, we assume that the silicon mirror is suspended from 4 monolithic wires with a length of 400 mm and a diameter of 0.5 mm; for the jellyfish connection between marionette and suspended cold platform we assume a total cross-sectional area A divided by wire length l of 10^{-6} m^{-1} , e.g. 12 wires with a length of 750 mm and a diameter of 0.3 mm, for the connections between mirror reaction mass and marionette reaction mass we assumed slightly higher total cross-sectional areas; i.e. $A/l = 2 \times 10^{-6} \text{ m}^{-1}$ between marionette reaction mass and suspended cold platform we assumed $A/l = 3 \times 10^{-6} \text{ m}^{-1}$ and between suspended cold platforms and the fixed cold finger (connected to the Joule-Thompson restriction and cooling agent) we assumed $A/l = 4 \times 10^{-6} \text{ m}^{-1}$. The tests with the shaker have to verify that such jellyfish connectors are acceptable. Even so, the conductance of such a link is quite low; at room temperature it is less than 1 mW/K. About 50 kg material needs to be cooled down from room temperature to 10-20 K via these links; they form a serious heat resistance. On the other hand, the fact that we need very soft links in order to avoid vibrational noise on the mirror implies that we only can use moderate cooling power at low temperatures, since the heat resistance of the jellyfish connections limit the heat current; a sorption cooler seems optimally suited in that respect (since higher cooling power is not useful due to the jellyfish restriction).

Fig. 4.21 shows the temperature dependence of several elements for the current design, with low-emissivity for the bottoms of the thermal shields. After about 10 hours, the liquid Nitrogen shields are in thermal equilibrium. The top reaches ultimately an end temperature of about 112 K, the front panel with the shielded pipes around the laser beams and baffles reaches an intermediate temperature at the center (about 103 K) and the bottom in this simulation is directly cooled by the liquid Nitrogen, so it stays at 77 K. The top and bottom of the inner shield are at almost the same temperature, due to the fact that the conductivity in the shield is large. Radiative heat loss at any part of the shield is distributed via conductance in an efficient manner. The cold finger in this simulation represents the copper bar that is connected via the 2 jellyfish links to the 2 cold floating platforms above the marionette. It initially cools down slower than the inner shield, since it is cooled down with 3 W via the simulated He cooler; but the inner shield loses much more than that via radiation towards the outer shield. It takes about 5 days before the cold bar temperature drops below 30 K, from which moment in time our cooling power decreases. Only at these low temperatures does the conductivity of the jellyfish links increase enough to get more efficient conductive cool-down of the cold platforms, the reaction masses and marionettes, and finally the mirrors. Indeed, the temperature of the cold platform is lagging the cold finger by a few days (see the decrease in temperature around 200 hours) and the temperature of the cold platform stays higher, since it continuously receives heat from the reaction masses and marionette via conduction, and from the surroundings via radiation. In this simulation, even after 1000 hours the mirror temperatures are still around 100 K and only after a week or so of cooling do they become colder than the inner thermal shields; implying that in the first week the heat loss is dominated by radiation, not by conduction.

Fig. 4.22 shows the temperature as a function of time for some elements in both the calculation

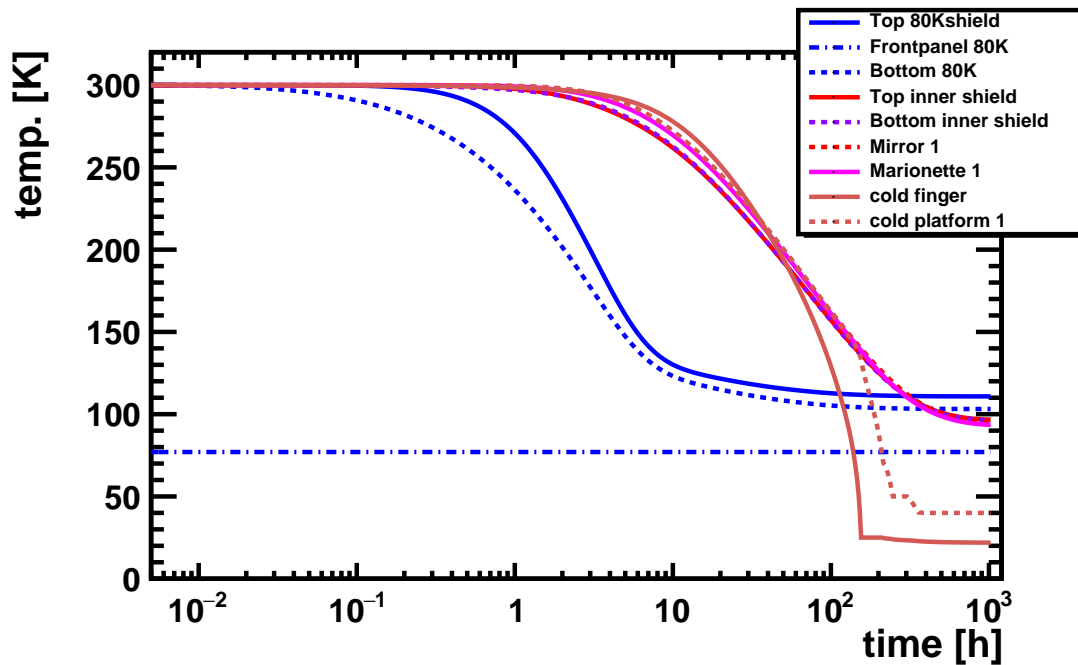


Figure 4.21: Temperature as a function of time for several elements in the simulation.

with shiny shields (emissivity 0.1) and black bottoms of the shields (emissivity 0.9). For the liquid-Nitrogen thermal shields, the temperatures are almost the same, although it is noteworthy to see that the lower emissivity in the first calculation leads to higher temperature of the top of the liquid Nitrogen shield. That is due to the fact that the *inner* shield cools down more slowly, leading to a higher radiation load on the *top* of the outer shield. The most important difference in the two scenarios is the cool-down time of the inner shield (for which the temperature at the bottom is plotted). In the first hours, cool-down is about ten times faster, decreasing to a factor of 2 at temperatures around 100 K. Also, the mirrors reach lower temperatures earlier, although even after 1000 hours of cooling, the temperatures of the mirrors, marionettes, and reaction masses are still above 80 K. Blackening the marionette and reaction masses, for mirror chain 2, leads to quicker cool-down, but not as much as one might expect. This is due to the fact that although the radiative transfer goes up by about a factor of nine due to higher emissivity, the temperature differences between mirrors and inner shield are not that large. In order to get faster cooldown of the mirrors radiatively, one should obtain faster cool-down of the inner shields. Furthermore, it takes 100 hours to cool down the cold finger (20 kg of copper in this simulation) to 30 K, and only at those temperatures does the heat resistance of the jellyfish wires decrease enough to get a significant contribution from conductive cooling (at 30 K, the conductivity of the jellyfish is about 50 times higher than at 100 K).

To compare the cooling of radiative and conductive heat flow, these heat flows are plotted as a function of time in Fig. 4.23. Here, the total heat flow towards the liquid Nitrogen exceeds 2 kW in the first hour; this is not plotted for readability. In practice, we do not start with a cold bottom of the shield but will slowly fill the liquid Nitrogen vessel, so the heat flow will be limited to whatever flow rate we can use (probably about 1 l/min or 3 kW cooling power). In Fig. 4.23, the solid lines

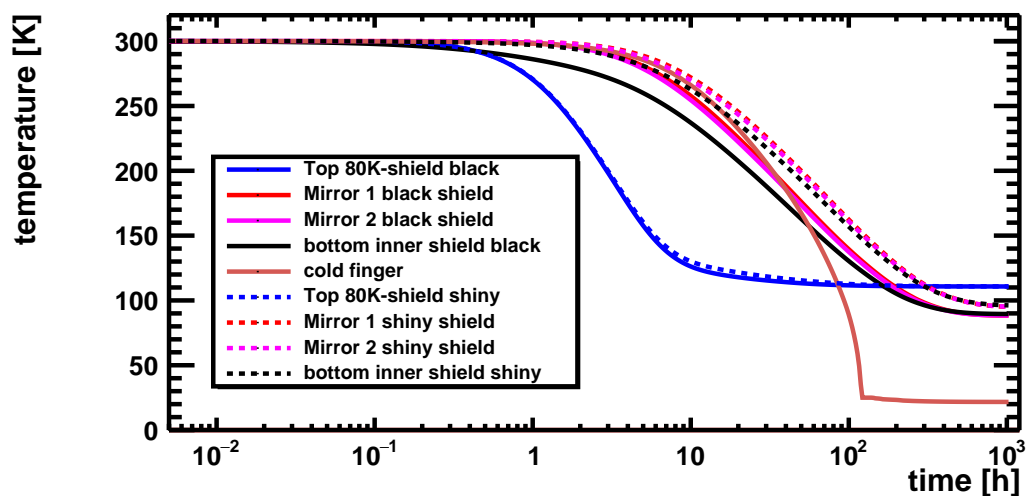


Figure 4.22: Temperature as a function of time for several elements in the simulation.

indicate conductive flow and the dashed lines radiative flow. A positive sign indicates that the heat of the element increases. In this figure, the radiative heat transfer to the bottom of the 80-K shield starts out at 300 W in the case of black-coated inner side of the bottom and 50 W in case of low emissivity, uncoated Aluminum). One can observe that after ten hours, the conductive flow into the black-coated bottom is less than into the uncoated bottom; that is due to the fact that for the black-coated shield, the inner shield temperature is significantly lower and the sides of the liquid Nitrogen shield experience less heat input (although the bottom experiences still higher radiative heat). For the bottom of the inner shield, the differences are remarkable, especially in the first ten hours. The radiative heat loss of the bottom of the inner shield is about ten times higher when the bottom is coated black, and whereas the bottom of the shiny inner shield loses heat via conduction (due to the fact that the sides of the shields lose heat more rapidly than the bottom), the bottom of the blackened inner shield gains heat, that is flowing in from the side panels and the top. The large difference in heat flow for blackened shield bottom results in the more rapid temperature decrease observed in Fig. 4.22.

Finally, Fig. 4.24 shows the heat transfer in the inner shield and mirror region for several elements. In this figure, the jellyfish refers to the conductive heat flow through the jellyfish wires from the floating cold rings above the mirror/marionette into the cold finger (the copper structure that is fixed to the bottom of the thermal shield). Shiny shield and black shield refer to the uncoated (emissivity 0.1) and coated (emissivity 0.9) bottom plates of the inner and outer thermal shields. Mirror chain 1 has uncoated and mirror chain 2 coated marionette and reaction masses. From this calculation it appears that the radiative heat flow to the mirrors is initially between 1 and 2 W and peaks somewhere between 1 and 10 hours. The heat flow for the black shield bottoms is a bit higher, but less than a factor of 2. This is due to the fact that the other sides of the inner shield are still shiny and that the temperature differences between marionette, reaction mass, and thermal shield are a bit lower for the black-coated option than for the shiny option. Nevertheless, due to higher temperature loss via radiation, the cold platforms above the marionette reach low temperature about 50 percent earlier, at

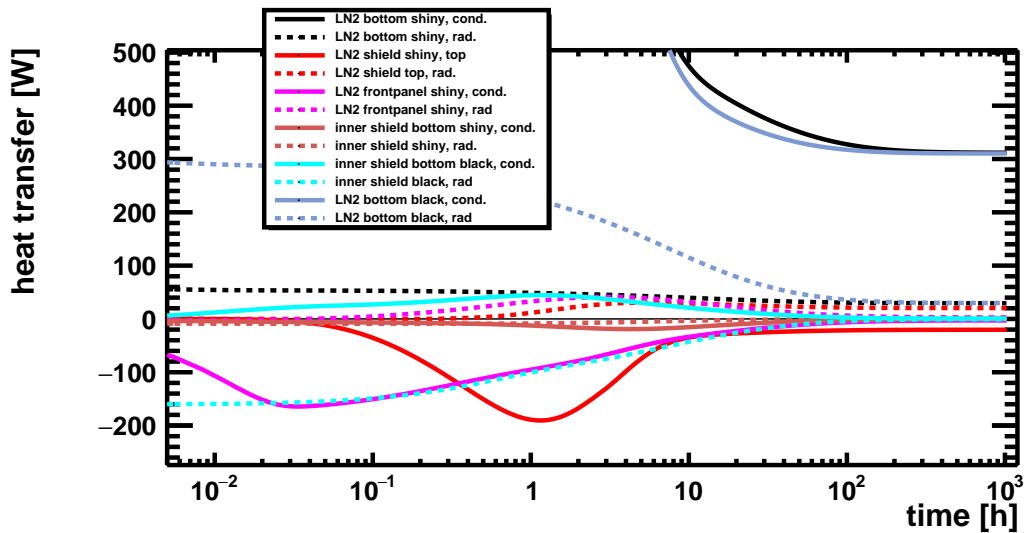


Figure 4.23: Conductive (solid) and radiative (dashed) heat flows for several elements in the simulation as a function of time. Positive flow means that heat flows into the element (the element heats up).

which point the jellyfish connection is starting to become useful. However, it must be noted that even after 1000 hours of cooling, only 0.2 W of conductive heat flows through this jellyfish, and with that net cooling power it will take a long time to cool down the reaction masses, marionettes and mirrors still behind that jellyfish.

We will have to verify whether we can increase the jellyfish wire diameters; in this calculation I used rather small diameters and a separate connection between the supported cold platform that distributes the wires and on the one hand the cold finger and on the other hand the reaction masses and marionettes. It may also be possible to just use this cold platform to loop the wires through; if they are not in good thermal contact then there is just a single jellyfish heat bridge between marionette and cold finger and cooldown may increase.

From these preliminary calculations, it seems that the majority of the cooling power is coming from thermal radiation. Using a 3-W sorption cooler for the inner cryogenic shield seems to slow down the overall cooling too much; after 1000 hours of cooling the temperature of the inner shields amounts still to around 90 K instead of the final equilibrium temperature of 30 K. Therefore, it is likely that in the final design, the inner cryogenic shields are pre-cooled either by a continuous flow Joule-Thomson cooler with a pump instead of a sorption cell, or using some pulse tube cooler, possibly with heat pipes connected to the inner shield. This noisier pre-cooler should then be switched off at shield temperatures around 30 K and the steady-state equilibrium temperature could be maintained by the sorption cooler.

Mirror Temperature Control, 123 K

For the initial operation of ETpathfinder (Phase 1a), we aim to operate around 123 K where the thermo-elastic noise from the bulk of the mirror material disappears. From Fig. 4.22 and Fig. 4.24 one can see that, due to radiative cooling, the mirror temperature tends to be close to the temperature of the surrounding thermal shields, and that a mirror temperature of 123 K can be reached in about 4 days time, using liquid Nitrogen cooling. At that time, the cooling of the inner cryogenic shields,

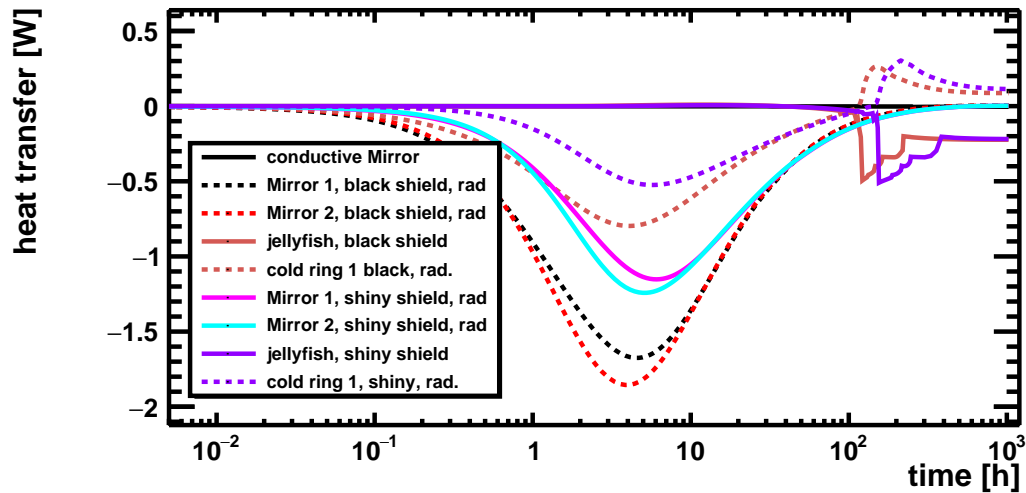


Figure 4.24: Conductive and radiative heat flows for several elements in the simulation as a function of time. Positive flow means that heat flows into the element (the element heats up). Label "shiny" refers to the bottom of the thermal shield uncoated (emissivity 0.1) and "black" to coated (emissivity 0.9).

mirrors, marionettes, and reaction masses is still dominated by radiative transfer. The liquid Nitrogen shields have already reached their final temperatures; the radiative load on these shields is about 300 W from the room-temperature environment and about 3 W from the (still warmer) inner shields. Therefore, an equilibrium temperature can be maintained by using a heater on the inner shield, about 3 W of heating power would be needed to maintain equilibrium temperature. The temperature gradient over the inner shield is rather small (since only 3W of heat is flowing through it); without heaters the difference between top and bottom of the shield is smaller than 2 K even during cool-down. The bottom of the inner shield faces the coldest ambient temperature (from the liquid Nitrogen vessel below it) and we plan to install a single heater on the bottom of this shield. Note, that the extra load on the liquid Nitrogen cooler is then only 3 W; raising the temperature of the inner cryogenic shields and mirrors to 123 K does not lead to noticeably higher liquid Nitrogen consumption.

4.4 Work Break Down Structure of the vacuum and cryogenics WP

Table ?? gives an overview of the tasks for ETpathfinder. In order to speed up the project, we started designing right away and no detailed planning has been made. The table gives a rough indication of the minimum time needed. After the clean room, the mechanics and suspensions are the first items that need to be installed, so our priority was to ensure that the mechanical infrastructure is suitable to host the interferometer for the coming 3 decades.

The cryogenic cooling to 10 K will happen at a later phase and design choices for that part have still to be made. We provide in the tower design an interface for the cryogenic fluids that we expect to use and we can still re-design the cryo coolers that deliver these fluids, which are located outside the mirror towers, if necessary. In the current concept, one 300-mm flange is used with feed throughs of cryogenic liquids, both for the liquid Nitrogen cooling stage and for the inner thermal shields. However, the initial calculation above shows that we might need 2 separate cryogenic cooling

systems to reach a working temperature of about 30 K for the inner cryogenic shields in a timely fashion; a powerful (30-40W at 30K) cooler (maybe a pulse tube cooler), that may be used in initial cool-down and could be switched off when the temperature of the shields is around 30 K, and a less powerful cooling system with low vibrational noise to maintain the steady-state temperature of the inner shields and cool down the mirror from 30 K to the final operating temperature (around 10 K). It is unfortunate that we did not have time to design these options more fully; here we want to state that if necessary, we can use one of the two 800-mm flanges for feed-throughs of the lowest-temperature cryogenic systems in the case that the 300-mm flange is limiting access too much. We think that the current design of the vacuum towers and shields will allow for an appropriate cooling scheme.

We know from measurements with the Virgo cryolinks that our liquid Nitrogen vessel should not introduce noticeable excess noise in the noise budget, but we want to measure and test innovations in that design (most notably the spiral heat exchanger that would eliminate boiling of the liquid Nitrogen inside the vessel in the mirror tower). We foresee to build a prototype and test cryogenic operations outside the ETpathfinder hall, measure vibrations and cool-down curves, and at a later stage prototype the inner cryogenic coolers for cooldown of the mirror to 10 K.

However, we do not have time to first install a vacuum system and do prototyping before tendering the towers for ETpathfinder; probably the vacuum vessel that we want for our prototyping of the LN2 shields arrives only a little before the first ETpathfinder tower, for which the time line is already very aggressive. Therefore, in this table we assume that the liquid Nitrogen system equals the current design; we already anticipate that the tests of this system are successful and support the current design. This is not ideal, but from our experience with the Virgo cryolinks we have confidence that we can design the right liquid Nitrogen cooling system and tender the mechanics of the vacuum system before waiting on the results of a prototype.

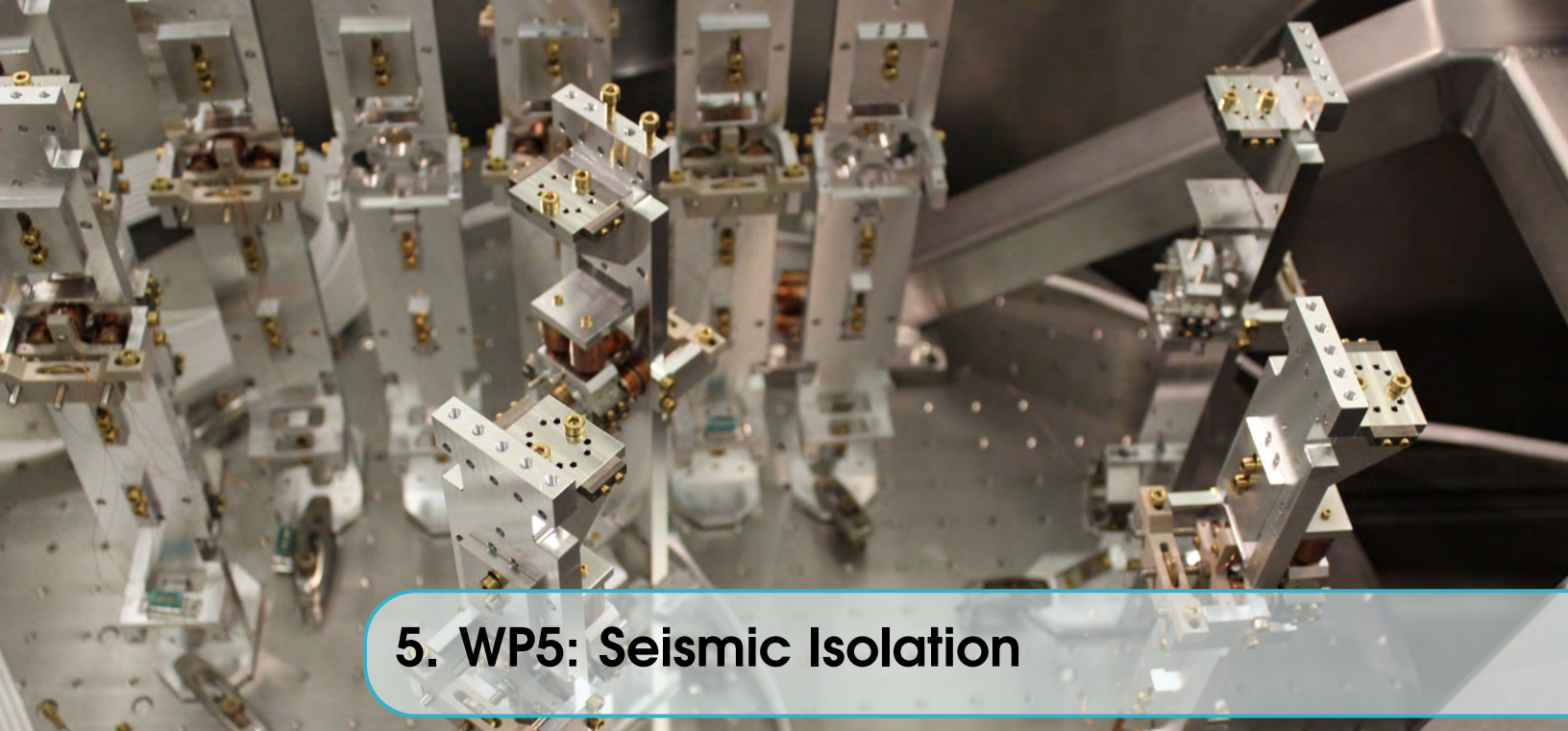
Summarizing, apart from designing, building and installing the cryogenic and vacuum system in the ETpathfinder facility, the following measurements are foreseen to finalize and validate our designs for ETpathfinder:

- Measure transfer functions of vibrations through the jellyfish thermal link. Scheduled for Q1 2020
- Measurements of the vibrations introduced by the liquid Nitrogen vessel; Produce a vessel with Teflon coating inside and lower the temperature to below boiling point via the spiral immersed into the system. This step requires the production of a LN2 vessel, a phase separator, the presence of liquid Nitrogen, accurate low-temperature seismometers, and a data acquisition system. Partial funding, lab space, and manpower still needs to be found.
- Design and fabrication of a prototype 10-K sorption cooler. For this step, agreements on funding and manpower are also not completed.

4.5 Detailed Budget for the vacuum and cryogenics WP

For the mechanics of the vacuum system, the budget has been detailed in table ??, the totals are repeated in table ?. Since after the clean hall, the first equipment that needs to be installed is the vacuum system, we spent most time in getting a detailed, future-proof design for that system. Therefore, we have a mature estimate for those costs (vacuum and mechanics together, close to 4.5 M€). For the liquid Nitrogen cooling we can make a good guess; for the 10-K cooling system the design is not yet mature, but the principal building blocks are obvious and hence included in the presented budget. Note, that the costs for the water cooling, electrical power, liquid Nitrogen storage,

and liquid Nitrogen transfer lines were assumed to be part of the infrastructure of the hall, see Chapter 2. We did not put quotations on those in this chapter. In the design, we assume a highly isolated storage vessel with a volume of 15 m^3 liquid Nitrogen outside the hall. For the liquid Nitrogen shields, we will use about 150 l/day per shield. We assume that the storage vessel consumes 5 l/day due to thermal losses and that the transfer lines from storage vessel to phase separator consume another 1l/h/line or 100 l/day (this requires better line design than at Virgo). That would raise the liquid Nitrogen consumption to about $0.7 \text{ m}^3/\text{day}$ and we could re-fill the vessel on a weekly basis. We estimate that when we want to use liquid Nitrogen for the heat sink of the 10-K sorption cooler, we would need an additional 18l/h/shield or 900l/day/arm; We could still operate for a week without refilling in such a case. This option would eliminate the need of pulse tube coolers for pre-cooling. However, in order to cool down from 300 K to 30 K, we need to dissipate about 60 MJ of heat for the inner cryogenic shields, cold fingers, and the mirrors, reaction masses and marionettes. Part of that is done radiatively, but from 100 K down this has to be done conductively. At the moment, we cannot rule out that we need a pulsetube cooler for the initial cool-down phase so pulse tube coolers were included in the design of the cryogenics.



5. WP5: Seismic Isolation

5.1 Overview

The microseismic climate of the ETpathfinder laboratory is typical for a highly urbanized area with large amplitude anthropogenic noise at frequencies between 1–30 Hz. The plot in Fig. 5.1 shows the acceleration spectrograms from two weeks of data recorded in 2018 in the future ETpathfinder hall: the characteristic daily and weekly amplitude variations are clearly visible, corresponding to changes in the traffic load on the nearby highway and in the level of human activity in the building itself.

A more detailed spectrum of the horizontal seismic noise is presented in Fig. 5.2, in which the low frequency region is dominated by the oceanic microseismic peak around 0.2 Hz. The amplitude of the microseismic peak is typically evolving on a seasonal basis, depending on the weather conditions on the high seas.

Multi-stage vibration isolators will be used to shield, with different residual motion requirements, core and auxiliary optics from environmental seismic noise. In particular, for the mirrors of the arm cavities, vibrations must be reduced, in the frequency band from 10 Hz to 10 kHz, to $10^{-18}\text{m}/\sqrt{\text{Hz}}$ or better, below the level of all other relevant noise sources, namely Brownian and quantum noise. Such a requirement involves suppressing the seismic noise by more than nine orders of magnitude in horizontal direction and six in vertical (assuming the typically observed 10^{-3} level vertical-to-horizontal spurious coupling). For this reason, the cryogenic mirrors will be isolated by means of long attenuation chains inspired by Virgo and KAGRA designs [22, 23]. A different solution has been devised for the room temperature beam-splitters and the input mode-cleaners optics for which compact double pendulum suspensions will be used, which will be placed on top of suspended optical benches which will provide additional seismic attenuation. For these optics a maximum residual motion of $10^{-15}\text{m}/\sqrt{\text{Hz}}$ is specified above 10 Hz.

5.2 Technology background

The vibration isolators of ETpathfinder are based on a hybrid approach in which bulk attenuation above 10 Hz is provided passively by means of a chain of low natural frequency mechanical oscillators

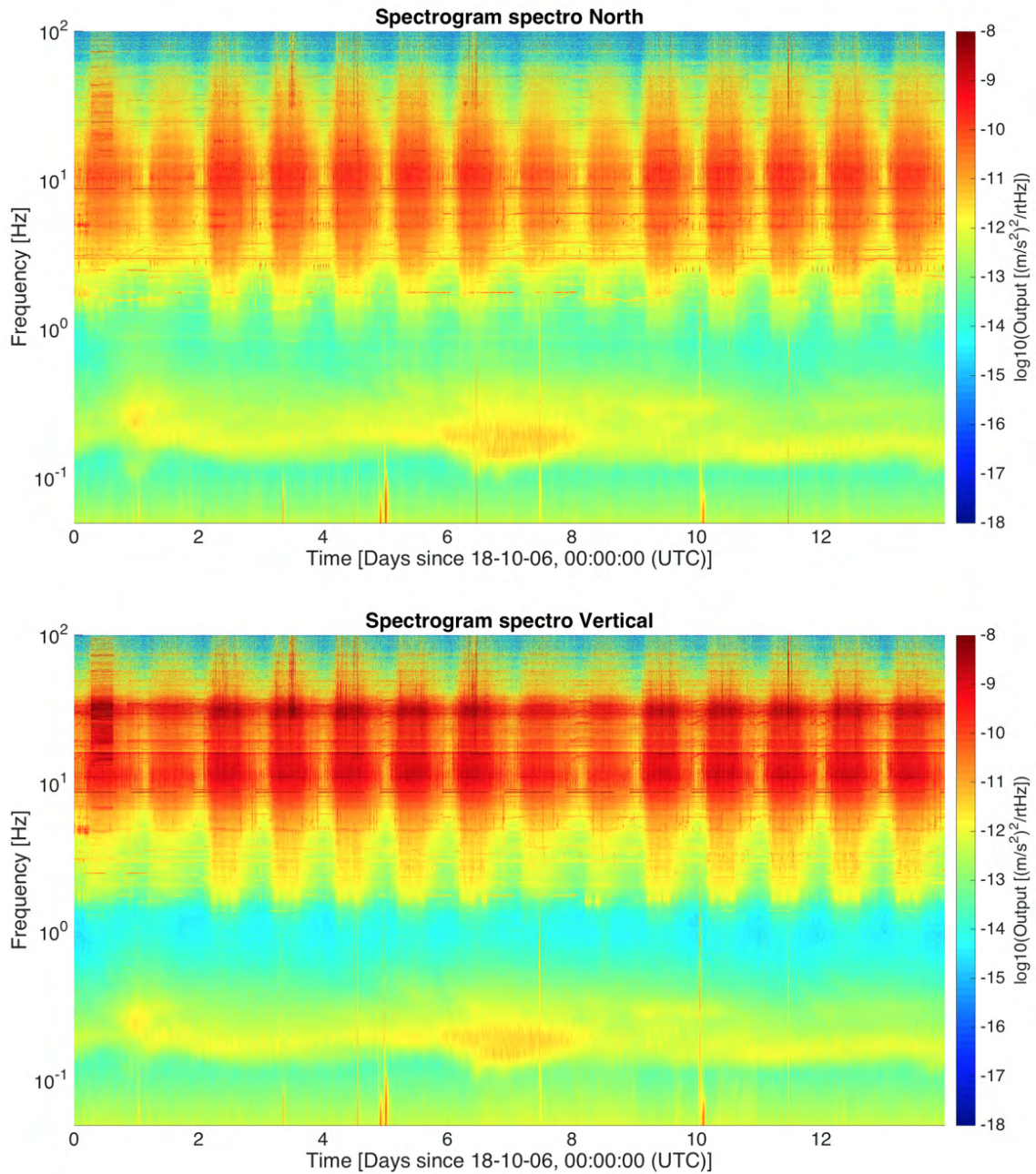


Figure 5.1: Spectrograms of ground acceleration measured inside the ETpathfinder building. On the top panel the data along North direction gives indication of the horizontal noise level; vertical floor vibrations are shown in the bottom panel. The temporal evolution of the oceanic micro-seismic peak can be observed around 0.15 Hz. The measurement was made by means of a triaxial geophone with 2.5 Hz natural frequency.

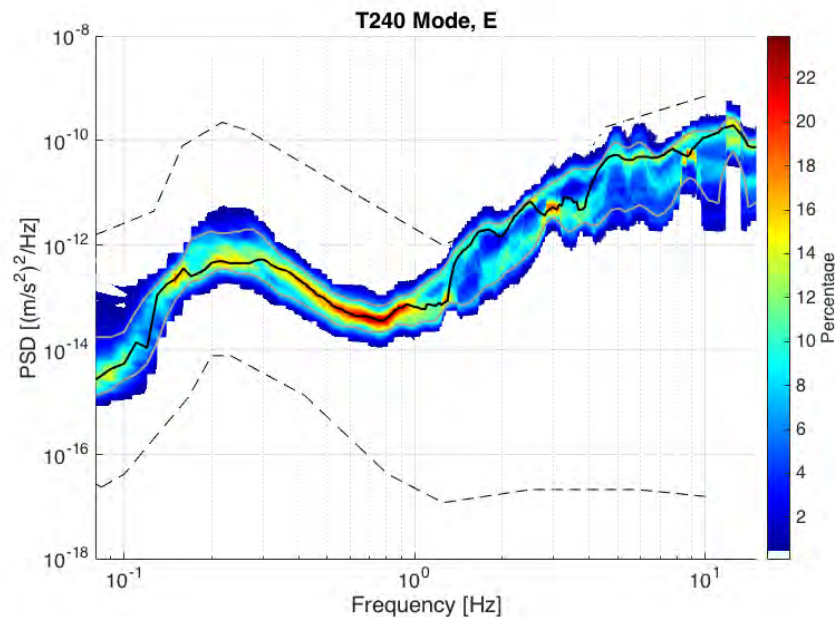


Figure 5.2: ETpathfinder hall horizontal acceleration power spectral density variation as measured with a Trillium–T240 broadband seismometer during the same observation time as in Fig. 5.1. The two grey traces indicate the boundaries of the 90th percentile. The New Low (NLNM) and High (NHNM) Noise Models from Peterson [21] are also plotted for reference (lower and higher dashed line respectively).

(*filters*). Filters are created with simple pendulums in horizontal and a set of cantilever springs in vertical direction. Feedback control is used to damp the low frequency rigid body eigenmodes of the system and to maintain, in the long term, position and orientation of the suspended body, being either a mirror or an optical bench. High-frequency internal modes are handled, where needed, by means of passive resonant dampers. The isolators are designed based on standard building blocks and consists of:

- a four degrees-of-freedom (two horizontal translations, yaw and vertical) passive very low frequency pre-isolator, optimized for performance augmentation by means of active attenuation;
- a chain composed of a variable number of passive standard isolation filters each providing attenuation along all six degrees-of-freedom.

Each attenuator carries a *payload* which includes the mirror (or optical bench), its suspension and steering mechanics.

The design of the main components is mature, based on the same technology already applied in several high precision optics experiments worldwide. Details about the most relevant building blocks are presented in the following.

5.2.1 Inverted pendulum

In all RTpathfinder isolators the first horizontal seismic attenuation stage is realized by means of an inverted pendulum (IP) platform. The platform is supported by three legs each consisting of a thin walled tube; the legs are hinged to the platform and to a stiff base ring by means of corner filleted circular cross-section flexures providing elastic restoring force (the details of the IP leg of the

MultiSAS seismic attenuator used in Advanced Virgo is presented as an example in the left panel of Fig. 5.3.

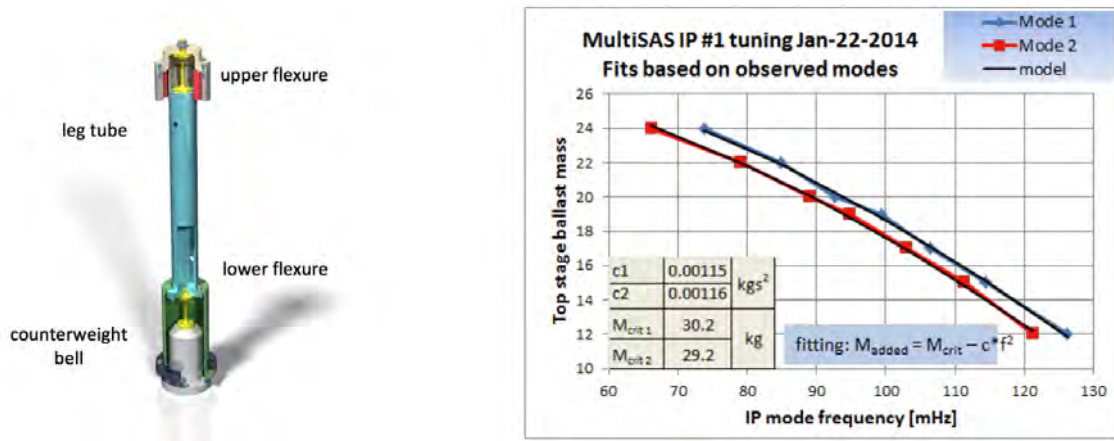


Figure 5.3: Left-panel: example of IP leg design; the flexures are shown in yellow while the bell carrying the counterweight for the neutralization of the leg inertia is shown in green. Right-panel: measured tuning curve in one of the MultiSAS IPs; the natural frequency of the two horizontal translational modes is shown as a function of the ballast mass.

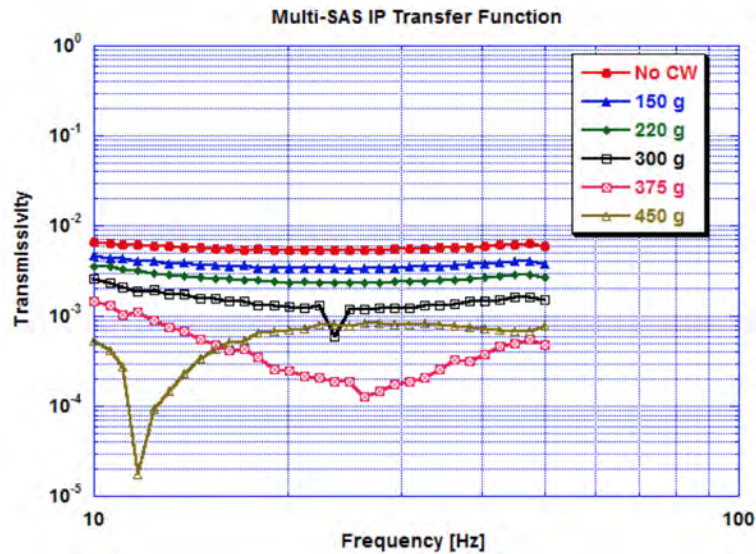


Figure 5.4: Suppression of the center-of-percussion effect. The different curves refer to the mass of the counterweight mounted on each leg.

The natural frequency f_0 of the IP is tuned by adjusting the load, exploiting the negative stiffness effect provided by gravity according to:

$$f_0 = \frac{1}{2\pi} \sqrt{\frac{k}{m} - \frac{g}{L}}, \quad (5.2.1)$$

where k is the flexure cumulative stiffness, m is the load and L is the length of the legs. Translational

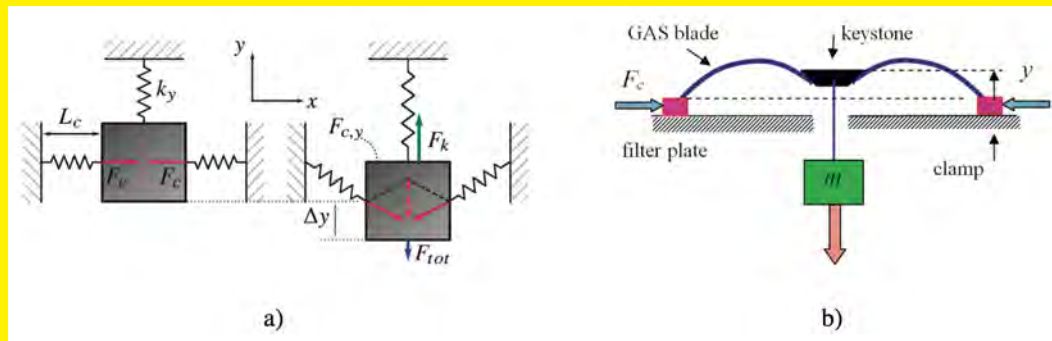
natural frequencies below 100 mHz are readily achievable (see an example the plot in the right panel of Fig. 5.3), allowing seismic attenuation around the microseismic peak. At higher frequencies the isolation performance of the inverted pendulum is limited by the inertia of the legs causing the transmissibility curve to reach a plateau (so-called center-of-percussion effect). However, by introducing suitable counterweights on each leg, the effect can be strongly suppressed and the plateau pushed down to -80 dB level (see Fig. 5.4).

5.2.2 Geometric anti-spring (GAS) filters

Filter stages are realized (see an example in Fig. 5.6) by combining cantilever blades in geometric anti-spring (GAS) configuration, for isolation along the vertical (y) direction, and single wire pendular suspensions for isolation in horizontal (x , z and yaw). The single wires allow to prevent, at first order, transmission of the tilt motion through the filter chain. Residual excitation of the angular (**pitch** and **roll**) degrees of freedom, due to the coupling with the horizontal ones, is suppressed by locating the effective bending point of the suspension wires as close as possible to the center of mass of the payload at each stage.

The geometric anti-spring effect

The anti-spring effect is illustrated in the left-panel of the figure. By introducing a horizontal static compression force F_c , any vertical mass displacement Δy will give rise to a force $F_{c,y} = -2F_c \cdot \Delta y / L_c$. This force cancels part of the restoring force $F_k = k_y \cdot y$ introduced by the suspension spring and effectively lowers the total stiffness. Changing F_c will alter the vertical stiffness and natural frequency of the system as desired. The stiffness indicated with k_y needs not be physically separated from the loading springs (see the sketch on the right panel), but merely represents the suspension stiffness in vertical direction.



a) conceptual illustration of the GAS effect. Left side: mass in equilibrium position with lateral preload F_c . Right side: mass in displaced state. Most of F_k is cancelled by $F_{c,y}$. b) practical implementation of the GAS effect for vibration isolation.

In the GAS configuration (see text box) the cantilever blades are arranged radially, mounted from a common retainer structure (filter body) and opposing each other via a central disk (keystone), to which the payload to be isolated is connected. The blades are completely flat when manufactured and flex like a fishing rod under load. Suitable clamps provide the blade base featuring an initial angle to accommodate the bending.

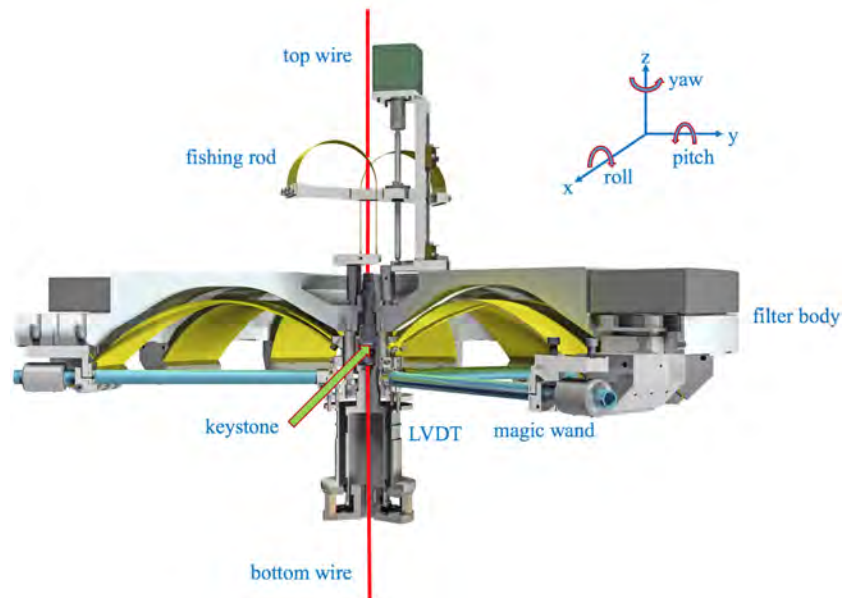


Figure 5.6: Standard GAS filter designed for the seismic isolation chains (MultiSAS) of the in-vacuum optical benches in Advanced Virgo. The filter body is a 100 kg 700–mm diameter stainless steel disk. The body is suspended by means of a single wire to the upward isolation stage and carries the clamps for the blade springs (in yellow). The keystone, at center, is used to connect all together the tips of the blades and acts as the suspension point for the downward pendulum stage. The filter also includes a vertical displacement sensor (LVDT) measuring the position of the keystone with respect to the body and a step motor driven auxiliary spring, called fishing rod, to apply large static forces for compensating temperature drifts and long term creep.

The radial position of the clamps is adjusted to realize the required amount of radial/horizontal compression necessary to build up the desired anti-spring effect and lower the vertical natural frequency of the system: periods of oscillation from 3 to 5 seconds are typically achieved, yielding up to 60 dB vibration attenuation at frequencies above 10 Hz (see an example in Fig. 5.7). The blades, the geometry of which is optimised with the help of FEM analysis, work at 80% of the yield stress of their material, selected based on the low creep and high strength properties; standard choices are either maraging steel C–250 or beryllium-copper C–17200, both precipitation hardened alloys.

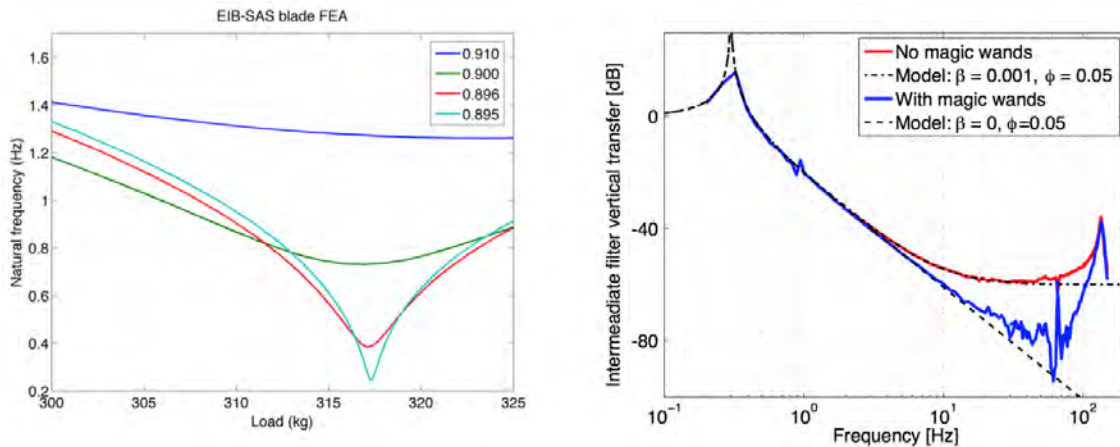


Figure 5.7: Left-panel: as an example, the FEA model of the GAS filter used in the Advanced Virgo EIB–SAS seismic isolator. The tuning curve of the filter is shown as a function of the compression rate. Right-panel: measured vertical transmissibility of a MultiSAS standard GAS filter tuned at 0.3 Hz natural frequency. The blue curve in the plot shows how the addition of the blade inertia compensators (magic–wands) can be used to boost the isolation performance above a few Hz.

5.3 Seismic isolation for the arm–cavity mirrors

The most sensitive optics of ETpathfinder are vibration isolated by means of a chain consisting of a room-temperature seismic attenuator, providing the majority of noise suppression in the 10 Hz–10 kHz frequency band, and of a two-stage payload cooled to cryogenic temperature, either 123 K or about 15 K. The ETpathfinder optical layout, with two Fabry–Perot cavities in each arm of the facility, requires two mirrors to be closely suspended in each vacuum chamber. For this reason, it has been decided to introduce, for each mirror pair, a long (3 meters) inverted pendulum stage as common pre–isolation platform for the two attenuation chains. In this section, details about the design of platform and seismic attenuator are presented.

5.3.1 Mechanics: pre–isolation platform

The pre–isolation platform provides a lightweight structural element to elevate the ground level of the seismic attenuation chains while minimising the footprint of the suspension system on the bottom part of the vacuum chamber. The 600–kg mass platform is supported by means of four inverted pendulum legs (see left panel of Fig. 5.8). In this way the fundamental resonances of the structure are pushed below 1 Hz, while the influence of higher order modes (like rigid body modes of the legs etc.) can be mitigated by first optimising design parameters like the geometry of lower and upper flexures,

Table 5.1: Preliminary inverted pendulum pre-isolator design parameters.

Parameter	Value	Unit
Leg length	3	m
Leg/CW bell masses	13/6	kg
Platform horizontal modes	< 0.1	Hz
Platform yaw mode	0.7	Hz
Platform bouncing mode	65	Hz
Platform tilt modes	55	Hz
Leg swing modes	> 80	Hz

geometry and material of the leg tubes, and eventually introducing tuned dampers. The choice of four legs instead of three was dictated by the need of maximising the accessibility to the cryostats and to the payloads, although the over-constrained configuration requires careful load equalization. The design parameters of the pre-isolation platform are summarised in Table 5.1.

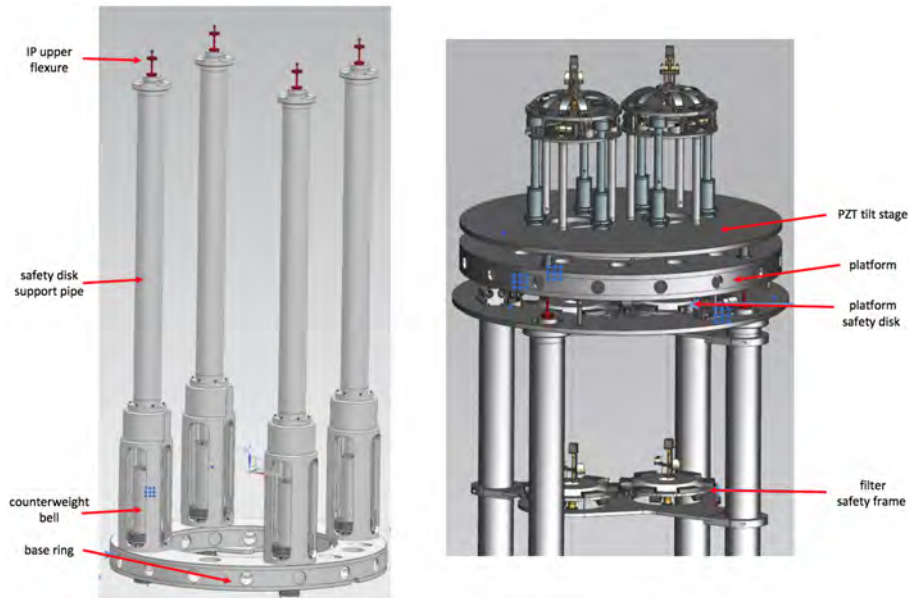


Figure 5.8: Left-panel: view of the pre-isolation platform support structure. Each IP leg is surrounded by a second pipe supporting the platform safety disk and the two safety frames for the filters of the chains. Right-panel: details of the platform. An optional additional stage, driven by three vertical piezoelectric actuators, is foreseen between the platform and the mirror seismic isolators for optional vertical and tilt active vibration suppression.

On the lower side, the inverted pendulum legs are hinged to a stiff base ring standing on feet that are directly connected to the Hall floor through low stiffness edge-welded bellows, ensuring that the suspension system is mechanically decoupled from the vacuum tank. The safety disk (see right panel of Fig. 5.8), which carries sensors and actuators for the horizontal control of the platform and limits its displacement, is supported by means of pipes surrounding the IP legs. The same frame is also used to support the safety structure of the filter chains. Optionally a tilt control stage, consisting of

an auxiliary platform supported by three vertical piezoelectric stack actuators, can be introduced to support the two seismic attenuators on top of the common inverted pendulum. The actuators are guided by means of flexure disks to prevent the piezoelectric ceramics to be damaged by shear loads. Although it is not considered essential for the operation of the system, this stage will allow to perform R&D studies on active seismic attenuation in pitch, roll and vertical degrees–of–freedom, if suitable angular inertial sensors will be available.

5.3.2 Mechanics: seismic attenuator

The role of the seismic attenuator is to provide passive vibration isolation for the mirror payload in the 10 Hz–10 kHz band in all six degrees of freedom. The preliminary layout of each attenuator is shown in Fig. 5.9.

The top stage (Filter–0) consists of a short (0.5 m) inverted pendulum providing a second layer of pre-isolation in **x**, **z** and **yaw** degrees of freedom and supporting the first low frequency (200 mHz fundamental mode) vertical GAS filter. The inverted pendulum is tuned around 100 mHz natural frequency and the mass of the platform has been chosen to be comparable with the one of each following attenuation stage; in this way all translational modes of the chain produce a significant recoil on it and they can be effectively damped by applying feedback at the level of Filter–0 without introducing noise at the mirror level. The other function of the platform is to provide large dynamic range static positioning of the payload (see Fig. 5.10); this feature is implemented as follows:

- three motorized correction blade springs act on the inverted pendulum platform to translate and rotate horizontally the entire attenuation chain within the range set by the platform end stops ± 6 mm, with a positioning accuracy better than $1 \mu\text{m}/1 \mu\text{rad}$;
- differential rotational adjustment between the platform and the attenuation chain can be performed thanks to the wire rotator mechanism, also step motor driven; the adjustment range is ± 10 degrees, with a positioning accuracy of $100 \mu\text{rad}$;
- the *fishing rod* is mostly used to cope with temperature changes and, occasionally, to correct any effect from the long term residual creep or elastic hysteresis of the GAS blades. The mechanism, making use of a pair of parasitic thin blade springs connected to the GAS system keystone, is also used in each of the three filter stages down along the chain. Temperature drifts affect the Young modulus of the blade spring material ($\Delta E/E \simeq -250 \text{ ppm}/^\circ\text{K}$ for C250 maraging steel), causing the position of the filter keystone to change. The fishing rod actuation range corresponds to about ± 1.5 K temperature change. The positioning accuracy achievable is better than $1 \mu\text{m}$. The reference signal for the fishing rod is the displacement of the keystone with respect to the filter frame read by the built–in LVDT (Linear Variable Differential Transformer) sensor.

The passive isolation chain makes use of three filters each consisting of a 20 kg disk hanging with a long wire from the previous stage and carrying a set of GAS blade springs tuned to 250 mHz. The keystone of the filter acts as suspension point for the next isolation stage and its static vertical position can be adjusted by means of a step motor driven fishing rod. An LVDT measures the position of the keystone with respect to the filter body to monitor the GAS system working point. The third filter of the chain, called the *steering filter* (see Fig. 5.11), is provided with additional features:

- three wires clamped on the side of the filter body suspend the payload reaction chain; the wires are made out of low thermal conductivity grade 5 titanium alloy and penetrate the payload heat shield system to reach the marionette reaction mass;
- three combined vertical LVDT–coil magnet actuators (in Maxwell–pair configuration) are

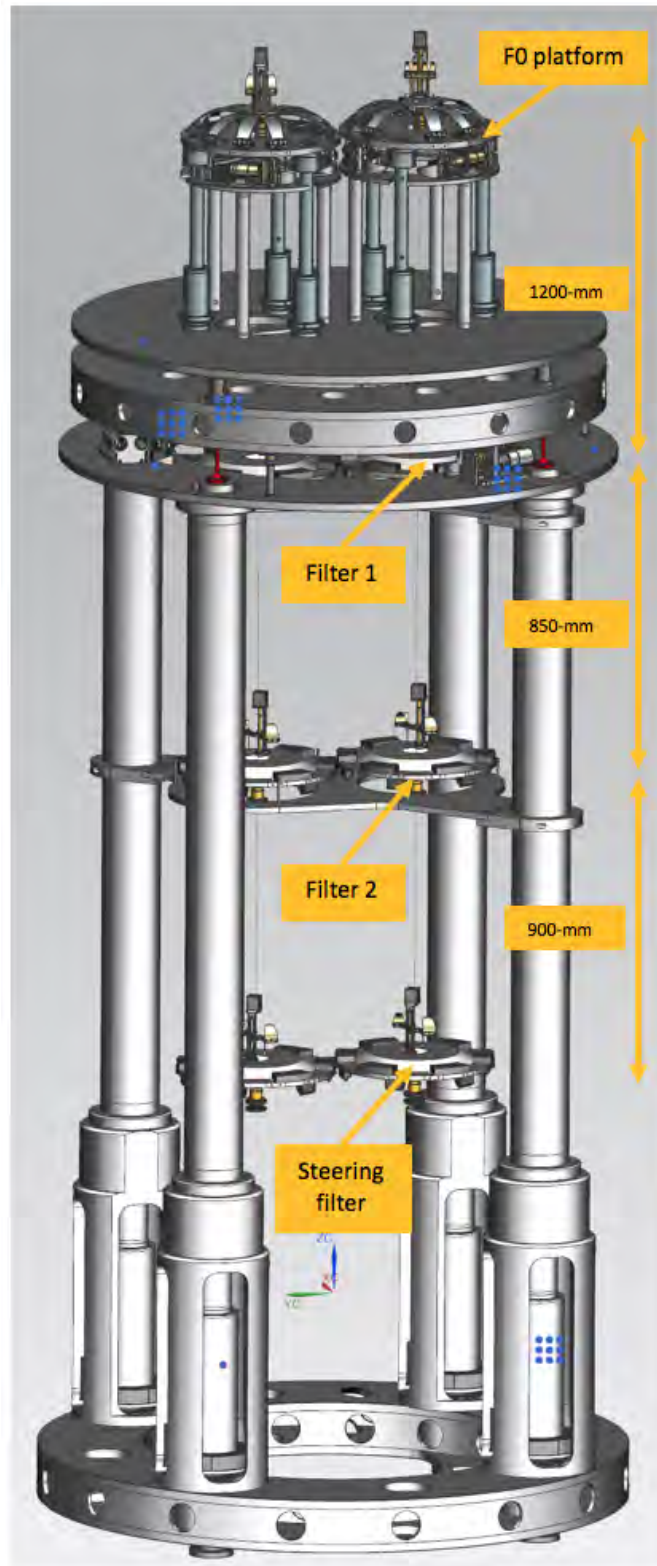


Figure 5.9: Overview of the room temperature seismic attenuation chains for the cryogenic payloads. Four horizontal (an inverted pendulum and three simple pendula) and four vertical (GAS filters) isolation stages are foreseen. The payloads are omitted for clarity.

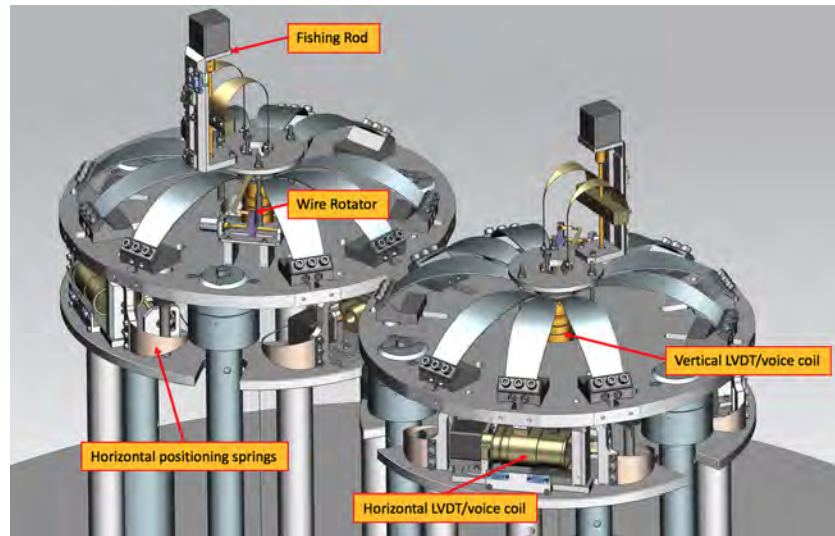


Figure 5.10: Details of the Filter-0 platforms. Each platform is equipped with step-motor driven correction springs that allow precision static positioning of the payload in horizontal, yaw (wire rotator) and vertical (fishing rod) degrees of freedom. The platform is also instrumented with horizontal and vertical displacement sensors (LVDT), collocated with voice coil actuators for operation in closed-loop.

foreseen to both monitor the orientation (**pitch** and **roll**) and the vertical position of the filter body with respect to the vacuum chamber (ground), and, optionally, to actively damp the tilt modes of the payload reaction chain.

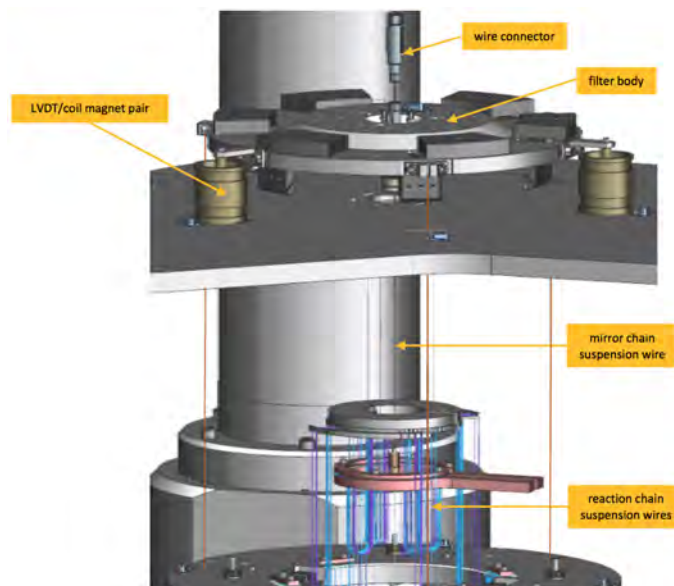


Figure 5.11: View of the Steering Filter. The filter supports the payload recoil chain and it is equipped with sensors and actuators for damping of its angular modes.

5.3.3 Passive seismic attenuation performance

FEM based models of the ground-to-mirror displacement transfer functions are presented in Fig. 5.12. The residual horizontal seismic motion of the mirrors above 3 Hz is expected to be limited by the spurious vertical-to-horizontal coupling. The model does not include yet the effects of the inertia of the cantilever blade springs and the dynamics of the filter keystones, which are expected to flatten the suspension transmission level at high frequency. More accurate simulations are being carried out at the time of writing this document. Nevertheless, the overall attenuation factor, exceeding 240 dB above a few Hz is considered sufficient, with an ample safety margin, to meet the specifications.

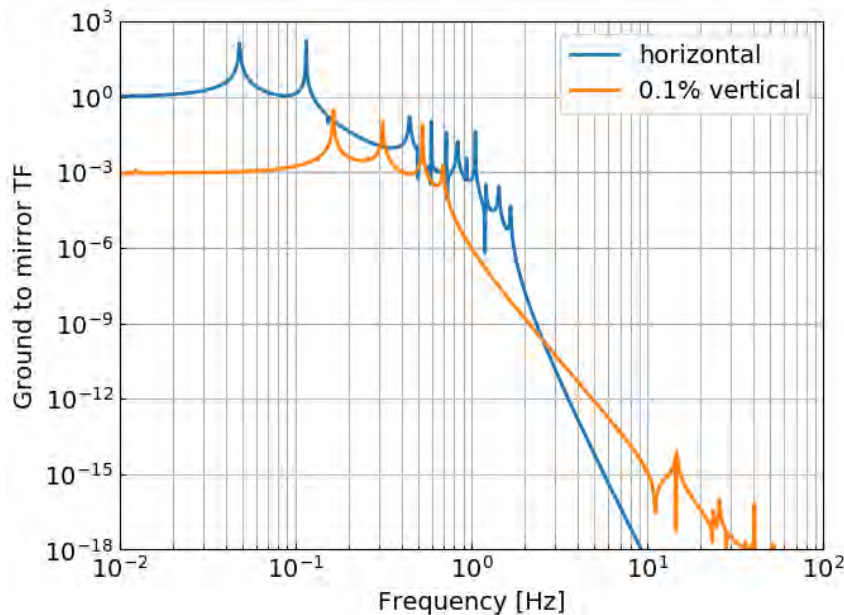


Figure 5.12: Simulated ground-to-mirror transfer function. Even at level of 0.1 %, the vertical-to-horizontal spurious coupling is expected to be dominant in the residual motion of the mirror.

5.3.4 Controls

For each individual seismic attenuator the baseline control strategy is the traditional VIRGO inertial damping scheme, in which the three modes of the IP platform and the low frequency horizontal translational modes of the seismic attenuation chain are damped by using sensors and actuators at the level of the suspension top stage. Nevertheless the novel configuration with the two attenuators supported by a third common inverted pendulum introduces a significant level of complexity which is related to the need of suppressing cross-talk between the two suspensions. In this respect the following design choices has been made:

- the pre-isolation platform (IP 0) mass is about 20 times larger than the mass of each Filter-0, and the natural frequency of its translational modes is a factor of two-three lower than in the small inverted pendulums (IP 1 and IP 2).

- the geometry of the flexures of IP 0 has been optimised for the highest possible rotational stiffness of the platform, in order to mitigate the cross–talk via the reaction torques.

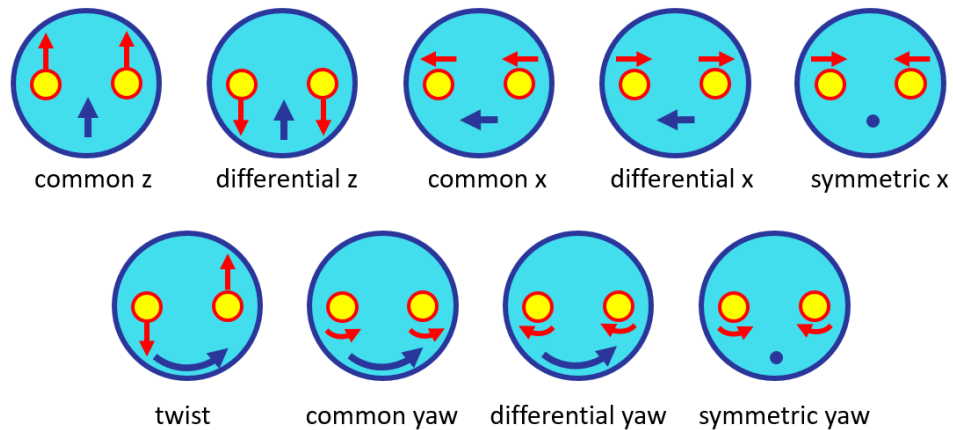


Figure 5.13: Schematic representation of the nine modes of the three inverted pendulums system: the modes in the first row are characterized by pure translation of the platforms, while those in the second row combine translation and rotation. All modes involve all three rigid bodies except for the symmetric x and symmetric yaw, in which the large pre–isolation platform remains still.

Extensive FEM and rigid body dynamic simulations have been performed in order to validate the design. The results indicate that:

- the three inverted pendulums are strongly coupled both in translation and in rotation, as shown in Fig. 5.13 in which the nine modes of the system are described;
- most of the translational and angular modes can be actively damped by means of the sensors and actuators of the pre–isolation platform, as shown in Fig. 5.14. Symmetric– x , symmetric–yaw and twist modes are instead characterized either by a null or by a weak coupling to the large inverted pendulum and therefore can only be controlled at the level of the small IPs;
- above the inverted pendulum system x and z fundamental modes, the dynamic coupling between the two attenuation chains is strongly suppressed. This crucial aspect is illustrated by the plots in Fig. 5.15: the z –displacement response of IP 1 to a force applied either to IP 2 or to IP 0 is about two orders of magnitude smaller compared to the case in which the force is directly applied to IP 1. The plot also shows (see the orange curve in the right panel) that the coupling between the two mirror suspensions is purely dynamic and vanishing towards DC, proving that independent static positioning of the two payloads is achievable.

Sensors and actuators: pre–isolation platform

Three voice–coil actuators in pinwheel configuration (120° relative orientation) are used to control the horizontal motion of the pre–isolation platform. The position of the stage with respect to the large IP safety frame is monitored by means of three horizontal LVDTs collocated to the actuators, while the inertial motion is measured by means of two triaxial Nanometrics TC–120 seismometers mounted inside vacuum sealed pods. The error signal for the control of the platform is generated by blending the signals from the LVDTs and from the seismometers at a cross–over frequency located below the micro–seismic peak. Seismic noise re–injection from the LVDTs (and the arm length noise with that) can be further reduced by implementing a tracking scheme between the different

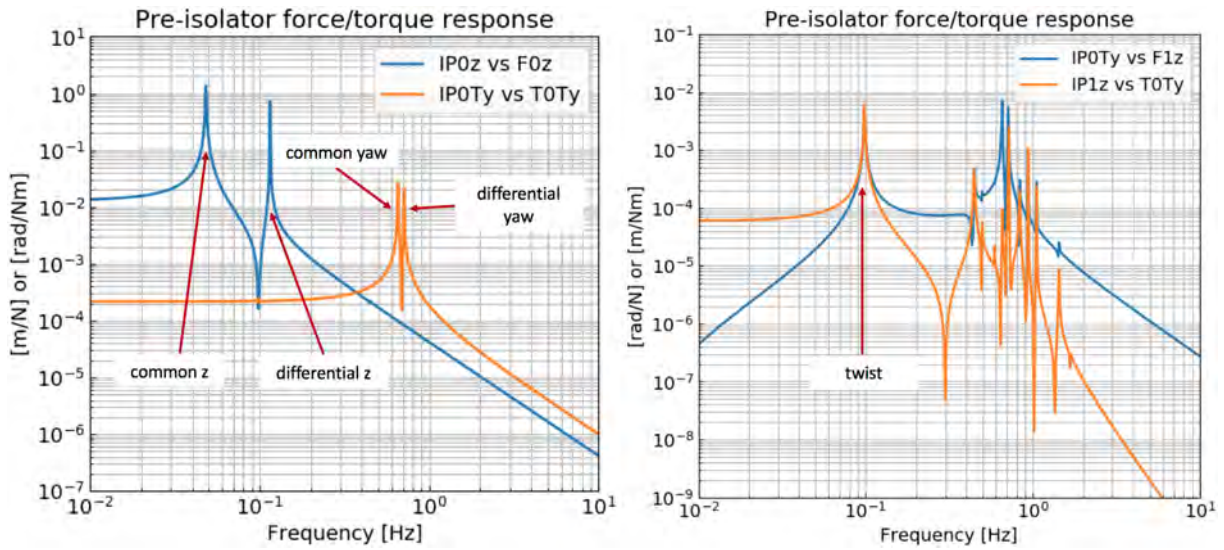


Figure 5.14: Left panel: force (torque) response of the pre-isolation platform, with the indication of the modes observable by the IP 0 sensors when the platform actuators are driven. Six modes, e.g. common z, common x, differential z, differential x, common and differential yaw, can be damped just using sensors and actuators of IP 0. Right panel: longitudinal (z-axis) response of IP 1 to a torque applied to IP 0 (blue-line), and yaw response of IP 0 when IP 1 is actuated longitudinally (orange-line). The plot shows that the twist mode produces a recoil observable on the IP 0 yaw degree of freedom and that it can be damped by means of the actuators of the large inverted pendulum.

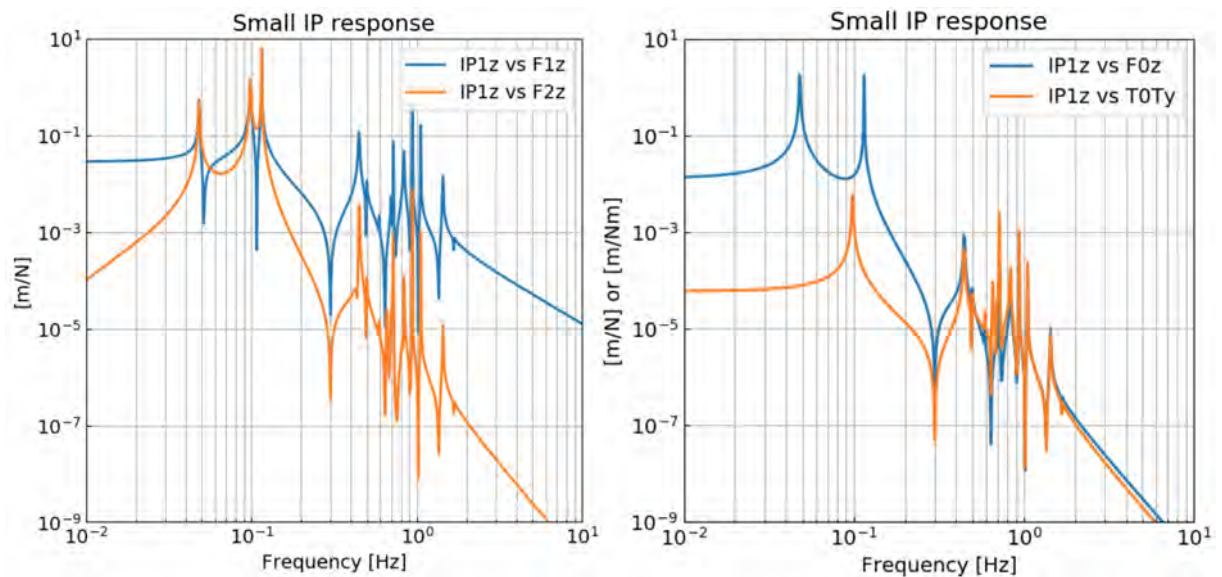


Figure 5.15: Left panel: IP 1 z-axis displacement per unit force applied by means of the local actuators (blue-line) and by the actuators from IP 2. The plot shows that the two attenuation chains are well decoupled above 0.1 Hz. Right panel: IP 1 z-axis displacement per unit force and torque (orange-line) applied to IP 0.

platforms, a strategy successfully applied in Virgo. The design of the platform foresees, for R&D purposes, an optional tilt control stage, mounted on three PZT stack actuators, supporting the two attenuation chains. Whenever this configuration will be applied, three vertical LVDTs, collocated to the actuators, will be installed and the two seismometers will be moved on top of the tilt control stage; two additional inertial rotation sensors, as for instance of the BRMS type [24] used in Advanced LIGO, would complete the setup.

Sensors and actuators: seismic attenuators

Inertial damping of the chain translational rigid body modes is performed at the level of the small IP platform. Filter-0 (F0) is instrumented with three horizontal and a vertical voice-coil actuators; three horizontal LVDTs are used to measure the position of F0 with respect to the Pre-isolation platform and a vertical LVDT is provided to measure the position of the F0 keystone; a Sercel L4-C horizontal geophone is also installed, inside a vacuum sealed pod, oriented along the cavity axis. The IP is controlled using only the LVDTs except for the cavity longitudinal degree of freedom in which the LVDT output is blended to the signal of the geophone, to reduced the noise injected at high frequency. The devised control strategy takes into account of the reduced noise level of the small IP, thanks to the filtering effect of the pre-isolator, of the large recoil expected on F0 from the modes of the chain, due to the close-to-unity mass ratio with the downstream stages, and of the control noise filtering from the downstream five isolation stages. The control of the suspension along the vertical axis makes use only of the F0 LVDT from which the ground noise is subtracted by using the information from the vertical component of the seismometers on the Pre-isolation platform.

5.4 Cryogenic payload

At early stage (Phase 1a) ETpathfinder will only operate the 123 K interferometer with single-crystal silicon mirrors suspended by means of metal wires. For this phase of the project a simplistic payload design, as close as possible to the traditional one used in Virgo for room temperature optics, has been chosen. In a second stage, when the related planned R&D program will be in advanced state, crystalline silicon fibers (or ribbons) will replace the metal wires to push down the suspension Brownian noise which is otherwise expected to limit the resolution of the facility in the mid-frequency range.

5.4.1 123 K payload

The payload (see Fig. 5.16) is a double pendulum suspension in which the upper stage, the *marionette*, is used for the dynamic positioning of the mirror in pitch, roll and yaw degrees of freedom. Feedback forces, both at the level of the marionette and at the level of the mirror, are applied from a coaxial reaction chain also consisting of a dual stage pendulum. The mirror double pendulum and its recoil chain are suspended, respectively, from the steering filter keystone and its body by means of 600-mm long low thermal conductivity Ti-6Al-4V wires penetrating the heat shields. The marionette is made out of 5056 aluminum alloy while the reaction masses are made out of Ti-6Al-4V to benefit from the poor electrical conductivity of the material for limiting the damping effect from the Foucault (eddy) currents induced by the actuation magnets. Based on the experience of KAGRA, all three bodies will be DLC (diamond-like-carbon) coated in order to increase the emissivity of their surface with the aim of reducing the payload cooling time.

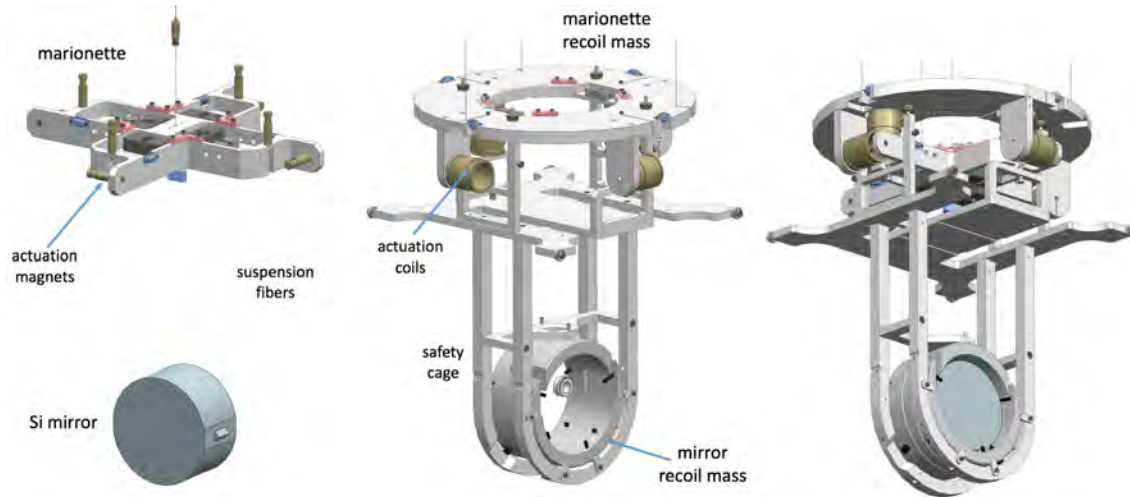


Figure 5.16: Details of the preliminary design of the 123 K interferometer payload. The left panel shows the double pendulum mirror suspension consisting of the 10 kg mass marionette and of the 3 kg mass single-crystal silicon mirror. The central panel shows the recoil chain comprising the marionette reaction mass and the mirror reference mass; part of the marionette reaction mass is the safety cage surrounding the last suspension stage.

The mirror consists of a single-crystal silicon cylinder with a diameter of 150-mm, 80-mm thick, and with two flat surfaces machined on its barrel (see Fig. 5.17a). On each flat a fused silica prism (spacer) is bonded, in proximity of the level of the mirror center-of-gravity, by means of Hydroxide Catalysis Bonding (HCB) technique; both the surface of the flat and the surface of the spacer are $\lambda/10$ polished to ensure the reliability of the bonding in terms of strength and mechanical losses. The pendulum length of the mirror, 400 mm, is determined by the edges of the spacers defining the lower bending point of the two suspension wires; thank to two tiny grooves carved into their edges, the spacers also define the wires longitudinal separation.

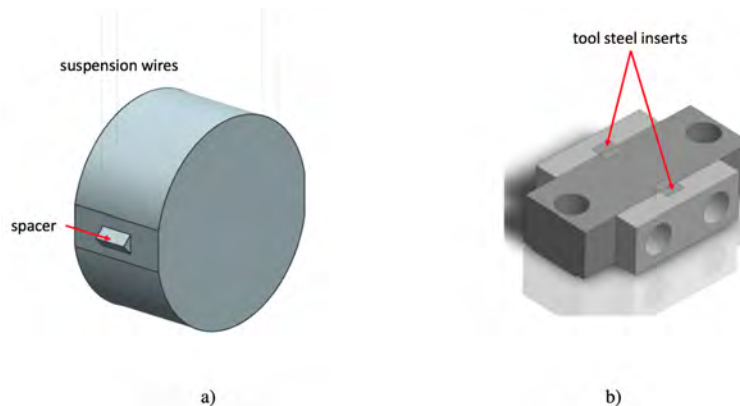


Figure 5.17: Details of the mirror suspension stage.

On the upper side the suspension fibers are fixed to the marionette by means of clamps the design of which is derived from Virgo. The clamps simply consist (see Fig. 5.17b) of an aluminum spacer and two plates provided with two high hardness tool steel split inserts (one pair per side). In each

Table 5.2: Suspension thermal noise modeling: geometry and material properties. The effective loss angle takes into account the material properties reported in literature and the dilution factor.

Parameter	Material	length [mm]	Diameter [mm]	Loss angle ϕ_{eff}	Notes
Marionette wire	Ti grade 5	600	0.8	$10^{-4} - 10^{-5}$	single wire
Mirror wires I	Al 5056	400	0.4	10^{-7}	four wires
Mirror wires II	silicon	400	0.7	10^{-9}	four wires

insert a jaw is flat while the other features a small V-groove machined by means of wire-EDM to keep the wire in position and to exert the clamping pressure on it. A calibrated torque, determined by FEM simulations, is applied when tightening the clamping screws in such a way that the elastic limit of the wire material is never exceeded. Based on this design, mechanical quality factors $Q \simeq 10^6$ have been achieved in Virgo for the mirror pendulum mode by using wires made out of A228 (C85) high carbon steel. A quasi-monolithic design, inspired to KAGRA, will replace the clamping system just described when crystalline silicon fibers will be introduced. Practical implementation of silicon mirror suspensions is, to date, an open issue and it is subject of various R&D programs worldwide. Different manufacturing methods and geometrical configurations are being evaluated with a major design constraint set by the operationally-safe tensile stress of 80 MPa.

Thermal noise figures

Mirror suspension thermal noise, e.g. the mirror Brownian motion associated to energy dissipation in the suspension wires, is the effect of a fluctuating force acting on the mirror with power spectral density given by (from the Fluctuation-Dissipation-Theorem):

$$F_{tm}^2 = 4K_B T \Re(Z_m), \quad (5.4.1)$$

where K_B is the Boltzmann constant, T is the temperature and Z_m is the mechanical impedance of the mirror. This latter is defined as $Z_m = F/v$, where F is a generic force applied to the mirror and v is its resulting velocity. The plot in Fig. 5.18 shows the estimated suspension thermal noise for the ETpathfinder interferometers over the different project phases; the material properties used in the calculation are presented in Table 5.2.

5.4.2 Controls

The marionette is controlled by means of a set of eight Maxwell-pair type (for better linearity) coil-magnet actuators, four vertical and four horizontal. The SmCo magnets are mounted on the marionette while the coils are mounted on the corresponding reaction mass. Four single coil-magnet actuators are used to apply feedback forces to the mirror; the magnets are mounted on fused silica cylindrical holders that are HCB bonded to the AR surface of the mirror, outside the coated area, while the coils are fixed to the mirror recoil mass. Both on the marionette and on the mirror the relative orientation between the magnets is such to prevent couplings to gradients of stray magnetic fields at the first order (see Fig. 5.19a) and b)). The payload angular position is sensed by means of two optical levers using the reflection from two perpendicular mirrors fixed underneath the marionette and whose centers lay along the suspension axis (see Fig. 5.19c).

The upper optical lever (magenta beam path in Fig. 5.20) is directed towards the side of the marionette, with 45° incidence angle and is reflected back to measure the roll of the payload; the same configuration is used for the lower one (blue beam path in Fig. 5.20) which senses pitch and

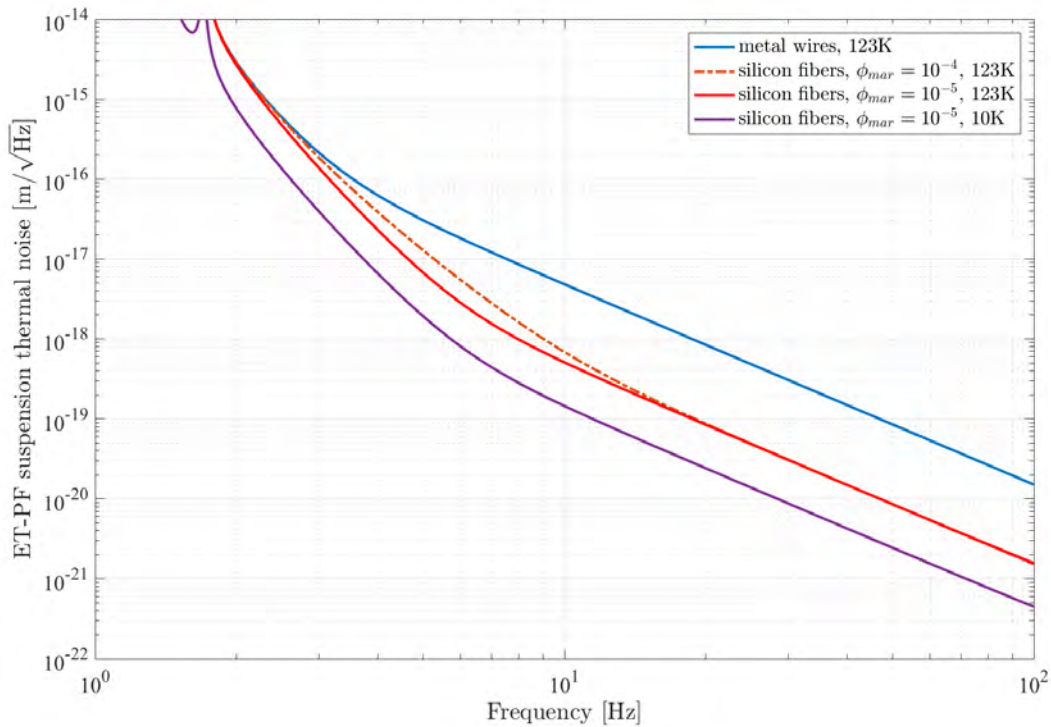


Figure 5.18: Modelled mirror suspension thermal noise in ETpathfinder. The calculation takes into account the contribution from all four arm cavity mirrors. Wires made out of 5056 aluminum alloy, known for the low mechanical losses at cryogenic temperatures [25], are planned for the initial phase of the project. A large improvement is expected later on with the introduction of crystalline silicon fibers, even though, as shown in the plot, in order to fully profit for the new material it is essential that losses also at level of the marionette are kept low.

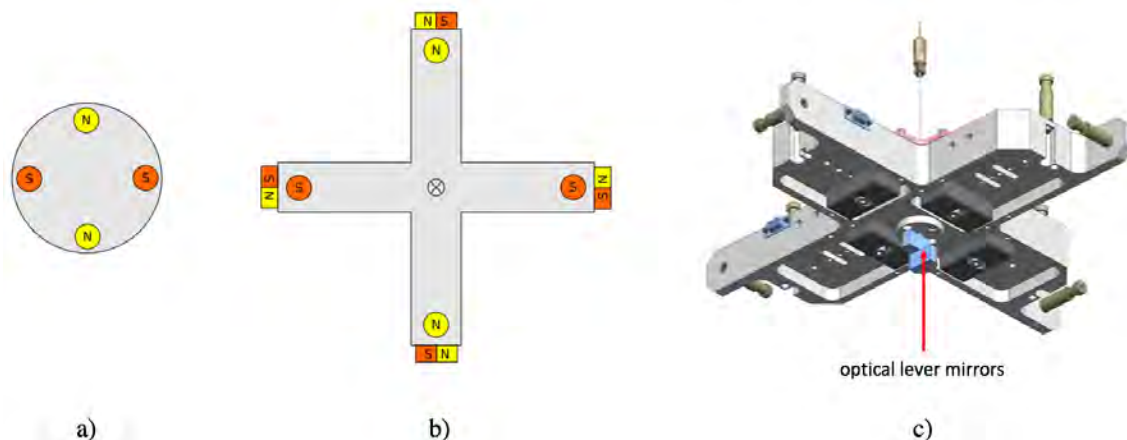


Figure 5.19: a) orientation of actuation magnets on the mirror; b) orientation of actuation magnets on the marionette c) details of the marionette optical lever reflectors: the height of the two horizontal incidence planes differs by 25 mm.

yaw rotations. The beam of a third optical lever (red one in Fig. 5.20) is incident on the front surface of the mirror providing useful out-of-loop information about its pitch, yaw and longitudinal position. Angular and longitudinal degrees of freedom of both marionette and mirror are optically diagonalized (decoupled) on focal and image planes of a suitable lens in front of the corresponding position sensors following the standard approach used in Virgo local controls. The payload optical levers are used to pre-align/steer, in pitch and yaw, the mirrors of the interferometer during the lock acquisition; once the interferometer is locked the control authority is released to the automatic alignment system except for the roll degree of freedom which stays local.

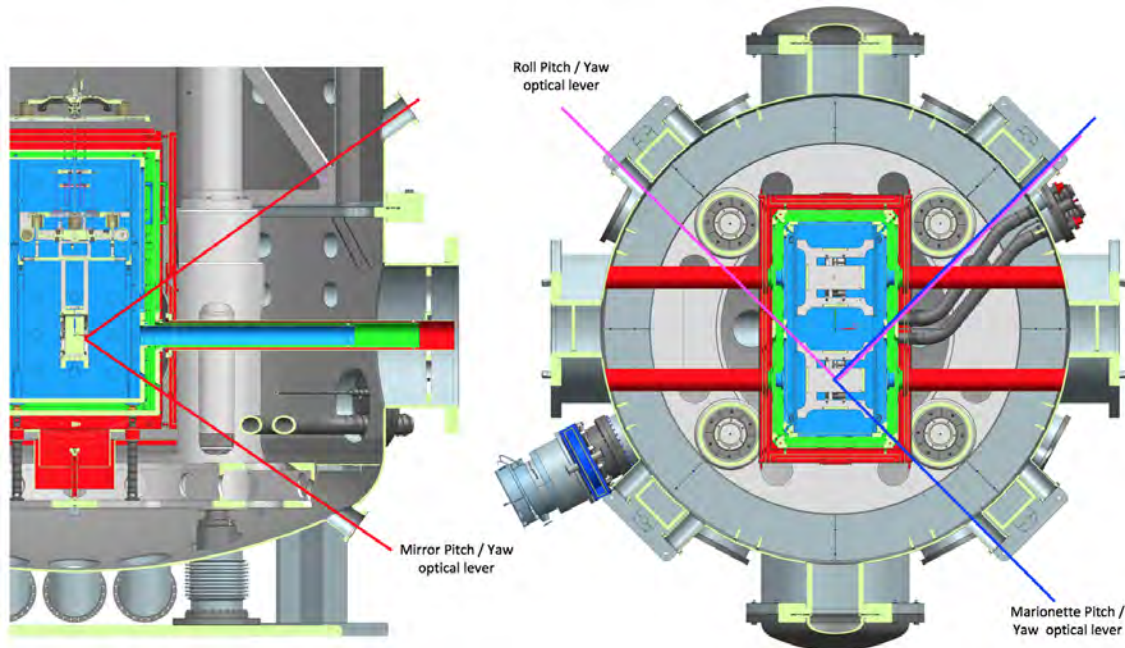


Figure 5.20: Layout of the payload optical lever system. The optical levers make use of SLED light sources and PSD (Position Sensitive Device) detectors both installed on external optical benches (not shown) placed on rigid pylons fixed to the hall floor. The benches are equipped with suitable boxes and connection pipes to avoid the in-air paths be spoiled by the air flow in the frequency range $0.5 < f < 1$ Hz.

5.4.3 10 K payload development

The design of the 10 K payload, though it will be closely inspired to the 123 K one, is not promptly available due to the additional challenge posed by the need of cooling the suspended mirrors by conduction.

Concerning the cooling aspects, a conceptual design has been devised which, however, needs to be validated with an extensive test campaign that will be carried out in parallel to the construction and the commissioning of the 123 K interferometer. The baseline configuration (see Fig. 5.21), treasuring the technical solutions adopted in KAGRA, foresees that

- the upper cold stage of the payload is connected to a cold finger by means of highly compliant braids made out of 6N-grade aluminum thin wires (thermal conductivity higher than $10000 \text{ W/m} \cdot \text{K}$ for 0.15-mm diameter wires between 4 K and 20 K);

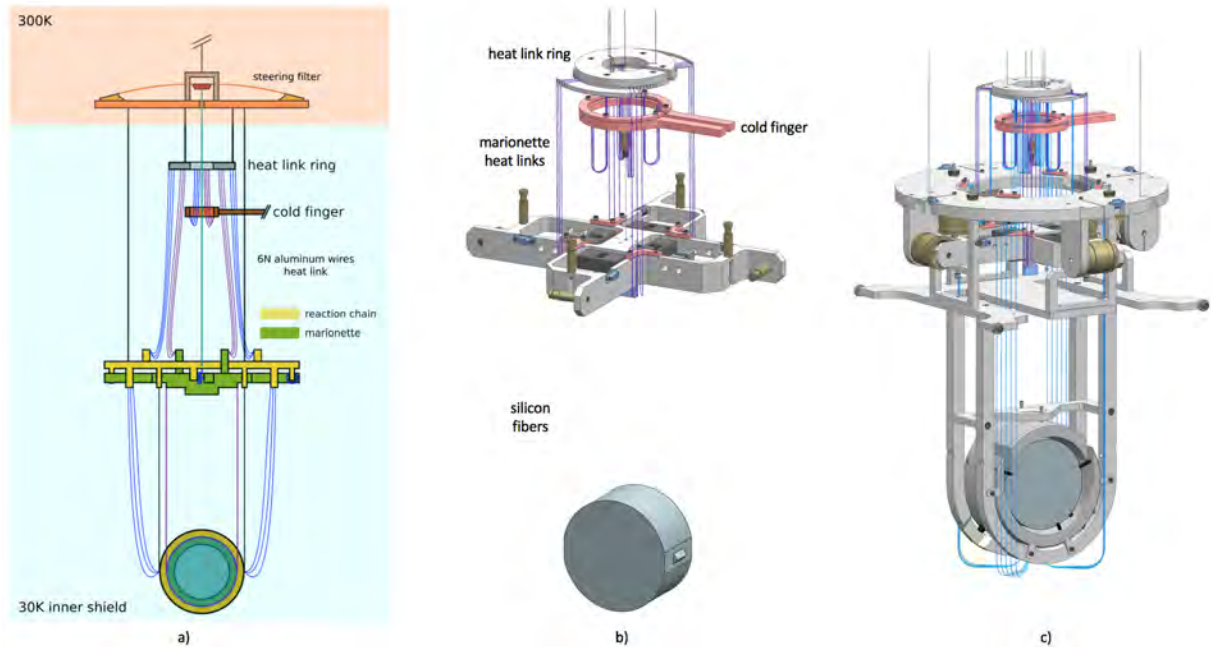


Figure 5.21: Conceptual design of the 10 K payload. a) schematic representation of the payload showing configuration and path of the heat conduction flexible links throughout the mirror suspension (blue) and its reaction chain (purple). Cooling of the last pendulum stage is provided by the silicon suspension fibers. b) details of the mirror double stage suspension. c) overview of the complete payload.

- similar braids are used to provide heat transfer throughout the payload, reaction-chain included, with the exception of the mirror pendulum stage which is cooled via the crystalline silicon suspension fibers in order to not spoil the thermal noise figures;
- the cold finger is rigidly connected to the cryostat mechanical structure and thermally insulated from the heat shields.
- an intermediate body, the heat link ring, suspended from the room temperature steering filter frame, is placed between the payload and the cold finger to provide a passive filtering stage for the vibrations of the cryostat.

Transmission of cold finger vibrations to the payload is a crucial aspect of the mechanical design. A detailed FEM model of the mirror suspension chain, including the heat links, has been produced to investigate the boundaries of the design parameters space. In the simulation the geometry of the heat links is such that, with 30 mW thermal radiation load on the mirror and a cold finger temperature $T_{CF} = 4$ K, the marionette and the mirror reach an equilibrium temperature, respectively, $T_{MAR} = 8.5$ K and $T_{MIR} = 15$ K. A thermal conductivity of 15000 W/m·K and of 3000 W/m·K (see text box) has been assumed, respectively, for 6N aluminum and for silicon. The other parameters of the model are summarized in Table 5.3.

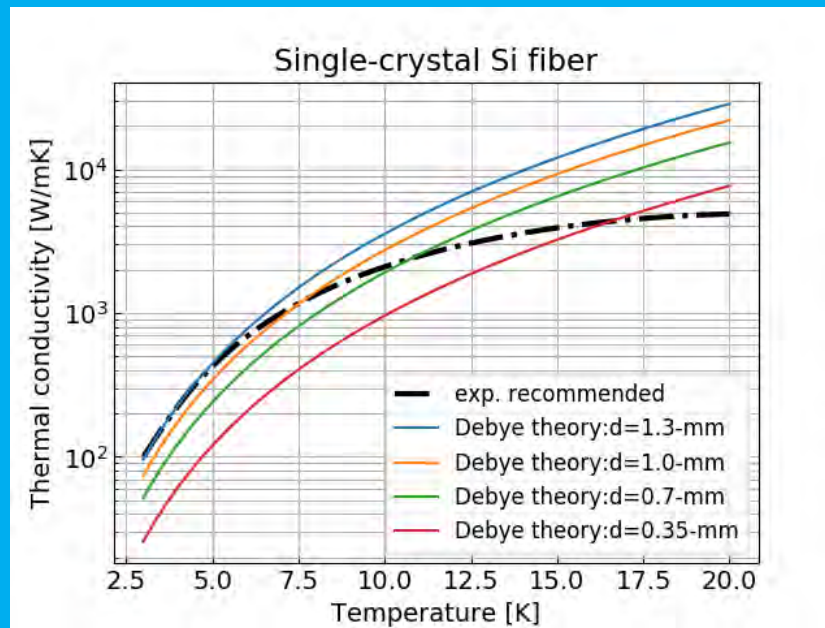
Low temperature thermal conductivity of silicon fibers

Thermal conductivity of high purity bulk crystalline silicon exhibits (see dash-dot line in the plot) a maximum value of about 4500 W/m·K between 15 and 25 K [26]. Better figures are

Table 5.3: Simulation parameters. HLR, MRM and RM are the acronyms for heat link ring, marionette reaction mass and mirror reaction mass.

Description	Number of wires	Length [mm]	Diameter [mm]
Heat link from CF to HLR	32	400	0.15
Heat link from HLR to MAR	12	600	0.15
Heat link from HLR to MRM	20	600	0.15
Heat link from MRM to RM	20	600	0.15
Suspension fibers	4	400	0.5

shown by isotopically enriched ^{28}Si which exhibits a much higher peak conductivity, up to $45000 \text{ W/m}\cdot\text{K}$, in the 20 K region [27]. At lower temperature all data are consistent with the Debye model according to which the thermal conductivity κ is given by $\kappa = \frac{1}{3}C_p v_s \lambda$, where v_s is the speed of sound in the material averaged over the different crystal orientations, C_p is the specific heat per unit volume (proportional to the third power of the temperature) and λ is the mean free path of the phonons. In this temperature region λ is constant and it is limited either by the concentration of impurities and isotopes or just by the physical dimensions of sample [28]. The solid lines in the plot show the calculated size-effect limit (so-called Casimir limit) of the thermal conductivity in circular cross section fibers of different diameters: the model suggests that these effects can be relevant in the sub-mm region.



Estimated Casimir limit ($\lambda = d$) of thermal conductivity in single-crystal silicon fibers of different diameter d . The diameter $d=0.35 \text{ mm}$ corresponds to 80 MPa loading of each of the four suspension fibers. Reference data for natural silicon measured on large size samples are plotted (dashed-dot line) for comparison.

The results of the simulation are shown in Fig. 5.23 in which a comparison between the transfer functions from cold finger to the mirror and from ground to mirror is presented. According to the model, the heat links are expected to spoil substantially the isolation performance of the seismic attenuation system, starting from a few Hz. When a vertical-to-horizontal coupling of 1% is assumed, a residual transmission of the cold finger motion at the level of about 10^{-9} can be observed. This figure requires an experimental confirmation since it appears to be marginally sufficient to meet the ETpathfinder specifications, even in the ideal scenario in which the cold finger does not introduce excess vibrations with respect to the hall floor. A dedicated test setup will be prepared to validate the model and to provide hints to improve the design (see also Fig. 4.20).

5.5 Seismic isolation for the optical benches

The two in-vacuum optical benches CBE1 and CBE2 will be suspended by means of multi-stage seismic attenuators the design of which is closely derived from the Multi-SAS [29] systems currently in use in the Virgo detector. Thanks to the Multi-SAS attenuators the residual motion of the Virgo benches is pushed below $10^{-14}\text{m}/\sqrt{\text{Hz}}$ level from 10 Hz onwards. In Virgo each suspended optical bench integrates an air-tight container to host all active analog and digital electronics needed to operate all installed sensors and actuators (photodiodes, picomotors, cameras etc.); cabling is limited to DC power and control signals are transmitted/received digitally via a highly compliant optical fibers. Such a configuration, requiring extended anodized surfaces for increasing the thermal emissivity, cannot be implemented in ETpathfinder due to the ultra-high vacuum requirement, and all signals must reach the bench via cables routed throughout the suspension with the risk of spoiling the seismic attenuation figure. For these reasons, even though critical optical components will benefit from an additional benchtop double-pendulum isolator, a third (compared to Virgo benches) filtering stage has been introduced.

5.5.1 Mechanics

An overview of a bench suspension is given in Fig. 5.24. The seismic attenuator consists of an inverted pendulum and a triple pendulum for horizontal isolation, while vertical attenuation is provided by three sets of GAS springs (Filter-0,1 and 2). The inverted pendulum design is the same as the pre-isolation platform of the arm cavities mirrors, except for the piezo-driven tilt control stage which has been removed, while the GAS filters (see the 3-D model of Filter-1 and Filter-2 in Fig. 5.25) are simply copies of the ones used in the Virgo Multi-SAS units.

The suspension can handle a bench with a total mass of 320 kg, 120-kg of which can be converted in usable payload (optics on top of the bench) by removing the ballast weights fixed to side walls (see Fig. 5.26). In order to preserve the tilt stability, any change in the vertical position of the center-of-gravity, due to a mass re-arrangement, can be compensated by shifting the bending point of the suspension wire by acting on the two connectors.

5.5.2 Controls

The bench suspension is controlled in a way very similar to the arm cavity mirrors seismic attenuators. Large dynamic range static positioning of the bench in all six degrees of freedom is available by means of:

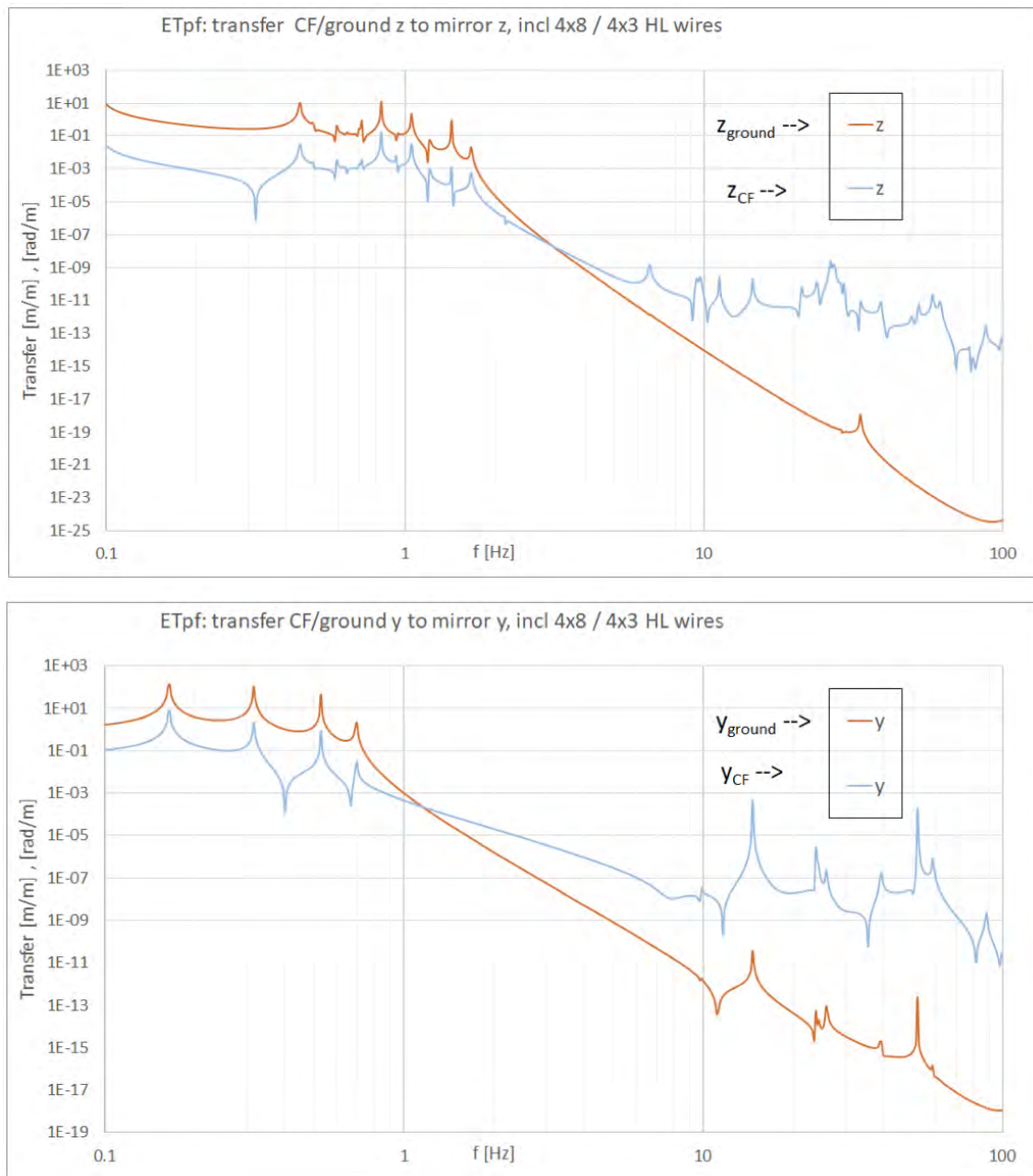


Figure 5.23: Calculated horizontal (top) and vertical (bottom) transfer functions (blue lines) from the cold finger to the mirror. Modeled ground-to-mirror transfer functions (orange lines) are shown for comparison.

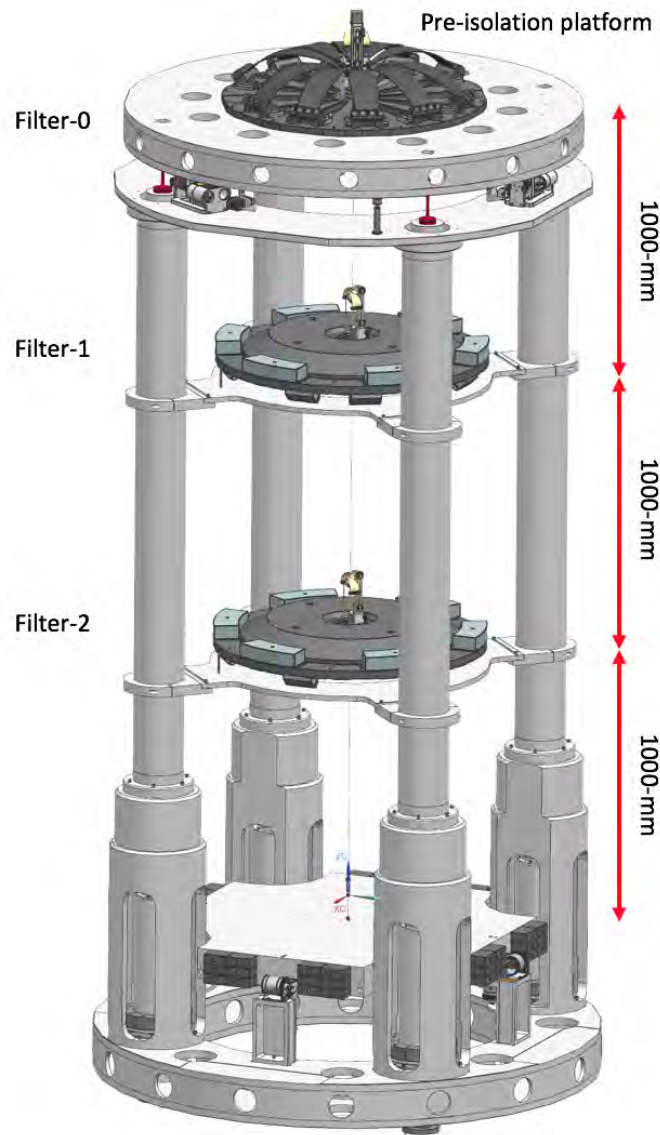


Figure 5.24: Overview of the bench suspension: The 3-m long four-legs of the inverted pendulum carry a 350 kg mass platform which supports the F0 GAS filter. The wires connecting the bodies of the triple pendulum are 1000-mm long and the intermediate GAS filters F1 and F2 have a mass of about 110 kg each.

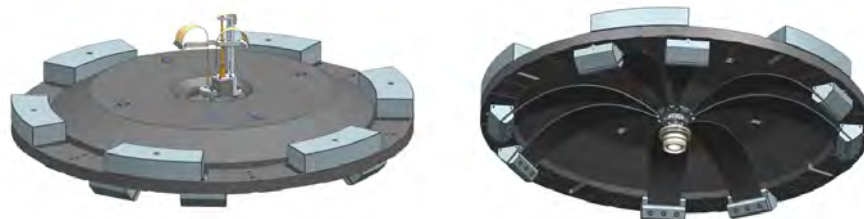


Figure 5.25: Top and bottom views of the Intermediate Filter.

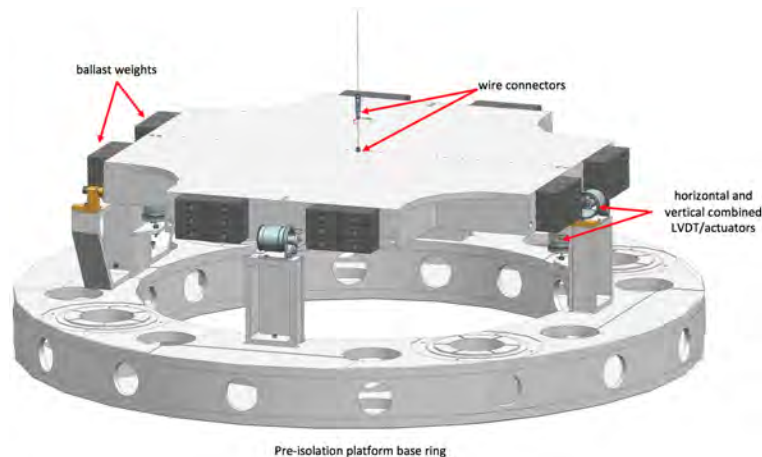


Figure 5.26: View of the suspended bench.

- three correction blade springs acting on the inverted pendulum platform for the horizontal position;
- three fishing rods, one for each set of GAS springs, for the vertical position;
- a differential rotational adjustment between the top stage and the suspension chain (based on a Harmonic Drive coupling) for the yaw orientation. The mechanism is located on the keystone of Filter-0;
- two movable counterweights located underneath the bench surface for pitch and roll orientation.

All adjustment mechanisms are step-motor driven.

Feedback is applied at the top stage level for the control of the attenuation chain translational degrees of freedom (x , z and y) and for the control of the inverted pendulum yaw (θ_y), by using the same set of sensors and actuators of the pre-isolation platforms of the arm cavity mirrors. Following the same scheme of the Virgo suspended optical benches, pitch, roll and yaw are instead locally controlled at level of the bench by means of a set of eight (four horizontal and four vertical) combined LVDT and Maxwell-pair type actuators.

5.5.3 Table-top suspensions

Beam-splitters and Input Mode Cleaners optics will be suspended on top the central benches, respectively, by means of compact double and single stage isolators. The design of the table-top suspensions is not discussed in this document since it will be based on existing design (from AEI-10m, LIGO, Glasgow prototype or similar) based on combination of pendulums and cantilever blade springs. No risk or unknown is expected.

5.6 WP5 risk mitigation strategy

Potential risks and the corresponding mitigation strategy are listed as follows:

- **multiple inverted pendulum control:** The triple inverted pendulum pre-isolation system foreseen for the mirrors in the arm cavities is a novel design and its control/damping is not trivial. If the crosstalk between the two mirror suspension chain would turn out to be too large and not manageable, the large inverted pendulum (IPO) could be disabled (blocked) without

Table 5.4: WP5 work breakdown structure.

Item	Name	Coordinating lab
Task	ETpathfinder Phase-1 design	Nikhef
Task	Arm cavities seismic isolation	Nikhef
Task	Optical benches suspensions	Nikhef
Task	Benchtop optics suspensions	Nikhef
Task	123 K cryogenic payloads	Nikhef
Task	Installation of suspended optical benches	Maastricht U.
Task	Installation of Input and End seismic attenuation systems	Maastricht U.
Task	Installation of Input payloads	Maastricht U.
Task	Installation of End payloads	Maastricht U.
Milestone	Conceptual design approved	
Milestone	ITM and ETM seismic attenuators design completed	
Milestone	ITM and ETM seismic attenuators ready for installation	
Milestone	Optical benches suspensions design completed	
Milestone	Optical benches suspensions ready for installation	
Milestone	Benchtop suspensions design completed	
Milestone	Benchtop suspensions ready for installation	
Milestone	Optical benches ready for installation	
Milestone	123 K payload design completed	
Milestone	123 K ITM payload ready for integration	
Milestone	123 K ETM payload ready for integration	
Milestone	Central optical benches ready for commissioning	
Milestone	123 K ITM tower ready for commissioning	
Milestone	123 K ETM tower ready for commissioning	

affecting dramatically the isolation performance of the system above 10 Hz, thanks to the large overkill factor accounted for in the design of the two attenuation chains.

5.7 WP5 work breakdown structure

The project planning presented in this document only refers to the initial phase of the ETpathfinder project (Phase 1a) which foresees the implementation and the commissioning of the 123 K interferometer. The planning consists of macro-tasks and milestones which are listed in Table 5.4. According to the present timeline, the central interferometer, is expected to be ready for commissioning by the end of 2021 while the terminal mirrors will be available starting from Q2 of 2022.

5.8 WP5 budget

A task-by-task detailed budget for the Phase-1 of the project is presented in Table ??.



6. WP6: Optics

6.1 Overview of the Optics WP

ETpathfinder fundamentally represents a modified Michelson interferometer with arm resonators. In phase 1, we will not consider recycling cavities to keep the complexity manageable. In any case, recycling cavities are not required to reach the target sensitivity of phase 1 of around $1 \times 10^{-18} \text{ m}/\sqrt{\text{Hz}}$, and the additional frequency response shaping that can be obtained with signal-recycling is not necessary. This interferometer can be conceptually broken down into four subsystems as shown in Figure 6.1: a stable laser source, in-vacuum input optics that provide a stable and clean beam, the main interferometer, and finally the readout train.

The *prestabilized laser* (PSL) provides the main laser source for the interferometer. It will consist of a stable, NPRO-like master laser that is amplified sufficiently to provide around 1 W of input power at the interferometer beam splitter. The PSL subsystem incorporates suitable actuators and detectors to reduce intensity and phase fluctuations of the laser sufficiently such that the laser can be locked onto subsequent, narrow-linewidth resonators. Ultimately, the arm resonators will act as the frequency reference. A pre-mode cleaner (PMC) at the output of the PSL subsystem will spatially filter the beam, reduce beam-pointing fluctuations and will act as a fixed reference for the beam that is delivered into the vacuum system.

Inside the vacuum system, the *input optics* are mounted on suspended benches. Since these benches provide already a significant amount of reduction of seismic noise, many steering mirrors can be placed directly onto those benches and be actuated with piezo motors. A input mode cleaner, with double-pendulum suspended mirrors, provides further frequency stability and reduction of beam pointing fluctuations. Afterwards, a modulation stage imprints phase modulations for the control of the main interferometer onto the laser beam.

The optical elements that make up the actual interferometer are called *core optics*: a beam splitter, and input test-masses (ITMs) and end test-masses (ETMs) in each arm. ITM and ETM together form arm resonators that strongly enhance the circulating light power in the arms and increase the phase sensitivity of the interferometer.

Detection of the interferometer output signal takes place with a single photo detector located

after an output mode-cleaner (OMC). The OMC's main task is to remove modulation sidebands and higher-order modes from mode-mismatches between the two interferometer arms from the output signal, as those can contribute a significant amount of shot noise, while not carrying any signal.

It is the task of the optics work package to provide the above subsystems, in close collaboration with work packages 5 (suspensions) and 7 (controls). Requirements and deliverables will be outlined for each subsystem below.

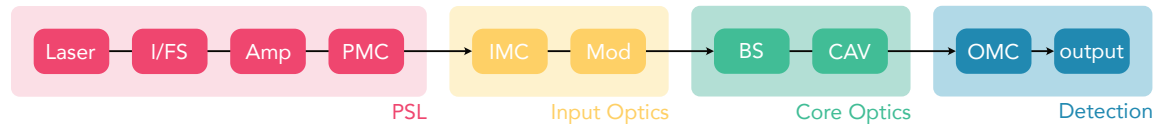


Figure 6.1: Block-diagram of optical subsystems from seed laser to detection. Each subsystem will be linked by beam telescopes. PSL, pre-stabilized laser; I/FS, intensity/frequency stabilisation; Amp, amplifier; PMC, pre-mode cleaner; IMC, input mode cleaner; Mod, modulation (bench) optics; BS, beam splitter; CAV, arm cavities; OMC, output mode-cleaner.

6.2 Pre-stabilized Laser

For both wavelengths that ETpathfinder will run at, we aim at an injected laser power of initially about 1 W at the beam splitter optic. This means that we will require around 2 W of initially available laser power, giving ample extra power that can be picked off for laser stabilisation and other control tasks, as well as allowing for some transmission loss of mode cleaners and Faraday isolators. The laser source will have to be pre-stabilised in frequency such that lock acquisition of the IMC is possible. Once the IMC and the arm cavities are locked, the PSL should provide feedback inputs such that the laser can ultimately be stabilised onto the long, narrow-linewidth arm cavities. Relative intensity-noise couples into the interferometer output because of the small dark-fringe offset, imperfect dark fringe contrast and because of potential imbalances in the main beamsplitter splitting ratio, which leads to unequal radiation pressure forces in the arms. The exact requirements will have to be determined from a noise simulation. A prestabilised laser system at 1550 nm by now is quite well understood and will consist of the items specified in table ???. Note that, except for some interfacing electronics, most of the electronics relating to locking loops are absorbed in WP7 (see Chapter 7). Many of the optical elements are readily available in high quality from multiple vendors, as 1550 nm is a standard in the telecommunication industry. For laser wavelengths around 2 μm , the market is much less developed and choices are not yet as clear. Options include Tm or Ho doped fibre lasers, or even wavelength-doubling of a 1064 nm NPRO. Due to higher costs of custom-made optical elements at this wavelength and the generally higher costs of infrared-grade fused silica that will have to be used throughout, in addition to thicker coatings, we assume the budget numbers for the 1550 nm laser system plus a 70% contingency factor.

6.3 Input and Output Optics

The *input optics* begin immediately after the PMC of the PSL. It can be further broken down into four parts, the *injection optics*, the *input mode-cleaner* (IMC), the modulation bench and the input telescope. The *output optics* begin in the (dark) output port of the beam splitter, with a telescope to an *output mode-cleaner* (OMC), after which the final $h(t)$ detection happens.

6.3.1 Injection Optics

It is the task of the injection optics to inject the laser beam into the vacuum system and provide a mode-matching onto the in-vacuum IMC. For this, the initial working assumption is that mode-matching happens on the in-air table with lenses, the beam is transferred into the vacuum chamber via a periscope, and once inside the vacuum system it will be guided with 2" diameter, suspended steering mirrors. To avoid stray light already at this stage, these optics should all be super-polished and all residual beams will be properly dumped at designated beam dumps (black glass positioned under Brewster's angle, and/or AR coated). We furthermore collect here several auxiliary optics that are needed to extract signal beams out of the vacuum system and onto in-air benches. Many of these auxiliary optics do not need to be suspended, therefore required mounting hardware is part of this work package and not of the suspension work package.

A preliminary layout of the in-vacuum input optics is shown in Figure 6.2. This layout will be refined and finalized with raytracing software such as OptoCad once beam parameters have been set. Specifically, the steering mirrors towards the IMC will need to be arranged in a way such as to get a sufficient Gouy phase difference for control of IMC auto-alignment. As part of the injection optics, suitable beam pick-offs for locking of IMC will be provided, while the detectors themselves are outside the scope.

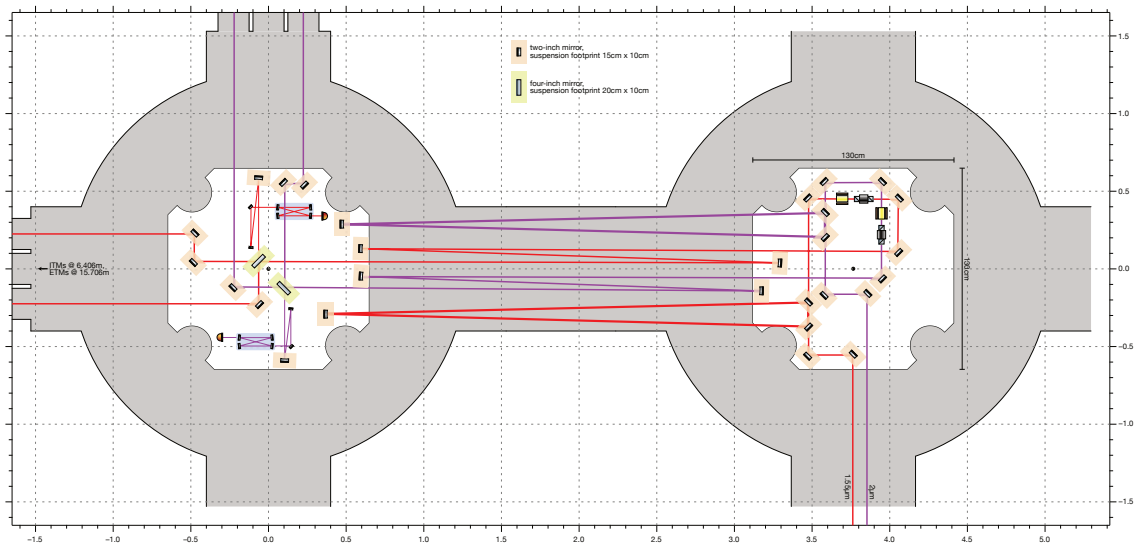


Figure 6.2: Schematic layout of in-vacuum input optics, input mode-cleaner and output mode-cleaner for the two FPMI to be installed in Phase 1a/b. The 1550 nm interferometer beams are shown in red, while the 2 micrometer beams are shown in purple. The interferometer arm cavities are located to the left (1550 nm) respectively top left (2 μm), the pre-stabilised lasers come into the vacuum system from the bottom right.

From this scope, the requested budget for Sec. 6.3.1 is given in Tab. ??, based on the prerequisites and deliverables given below.

Prerequisites:

- beam parameters of IMC
- beam parameters of PMC
- suitable auxiliary optics suspensions from WP5

- requirements from WP7 and IMC for beam pick-offs for control tasks

Deliverables:

1. optical layout for the positioning of injection optics, satisfying necessary pick-off beams and IMC AA requirements,
2. mode-matching solution from PMC to IMC,
3. set-up of in-air periscope into vacuum tank,
4. set-up of in-vacuum steering optics,
5. stray-light control inside the input chamber,
6. provide small optics, as well as beam dumps, also for other in-vacuum subsystems.

6.3.2 Input Mode-Cleaner

Inside the vacuum environment, but before the main interferometer, we will have another mode-cleaning resonator, the input mode-cleaner (IMC). The purposes of this resonator are

- suppression of higher-order transverse modes of the light field, such that a purified TEM₀₀ beam reaches the interferometer;
- suppression of the orthogonal light polarisation, as the two polarisations are non-degenerate for ring resonators with an odd number of mirrors;
- suppression of input beam jitter, as the mode cleaner will see these as higher-order transversal mode contributions and reject these – to avoid the resulting conversion into amplitude fluctuations, a power stabilisation stage will have to follow the IMC;
- passive filtering of frequency fluctuations above the linewidth of the IMC;
- use as a stable frequency reference for pre-stabilisation of the laser source.

Two important characteristics will have to be evaluated during the design phase, in close contact with the suspensions and control work packages. These are (a), the required length stability of the mode cleaner; and (b), requirements for additional phase modulation sidebands that might have to be transmitted through the mode cleaner. If this is feasible, then modulation sidebands could be imprinted already before the IMC, removing the necessity of an in-vacuum, suspended modulation bench. It is likely that the IMC would be installed between the input chamber and the beam splitter chamber, unless this would demand too high requirements on the relative motion of these two benches. The round-trip length of the IMC would then be of the order 6.5 m, equivalent to a free spectral range of 46 MHz.

The optics of the IMC will have to be tightly specified to guarantee a high transmission and low amounts of scattered light, especially since it will be difficult to shield the main interferometer from the latter within the available vacuum envelope.

The input mode-cleaner budget is listed given in Table ??.

Prerequisites:

- suitable optics suspensions from WP5,
- relative stability of suspended benches from WP5,
- requirements on linewidth and possibly FSR from WP7.

Deliverables:

1. mirror and coating specifications,
2. geometrical coordinates for the placement of the IMC within the vacuum envelope,
3. procurement and characterisation of optics,
4. installation of optics in suspensions from WP5.

6.3.3 In-Vacuum Modulation Bench

It is likely that, after the IMC, further phase modulation sidebands will need to be imprinted onto the laser light entering the interferometer. In addition, reflected light from the interferometer (the *bright port* field) should be separated from the incoming light with a Faraday isolator and made available for diagnostic and locking purposes. The budget breakdown is given in Table ??.

6.3.4 Detection Bench and Output Mode Cleaner

The dark-port output of the interferometer provides the main output signal. As in current large-scale detectors, we aim for a DC readout, i.e. with a single photo-detector that directly samples the (amplitude) modulation of a small offset field that leaks into the dark port. This offset field is generated by either DARM offset or MICH offset and should be of the order of a few mW. In addition to this carrier field, modulation sidebands and higher-order light field modes generated by mirror asymmetries will appear in the output port. These would contribute significantly to shot noise on the detector, while not adding any signal. Therefore, an output mode-cleaner (OMC) needs to be installed in front of the main output detector to suppress those other fields. Suitable base-line designs are available from Advanced LIGO and will have to be adapted to give the necessary mode spacing and suppression for our setup.

A mode-matching telescope is required to adapt the beam coming from the beam splitter to the eigenmode of the OMC. Some of these mirrors need a small amount of transmission that can be used to monitor the output field directly.

The main output detector, as well as locking electronics and an auto-alignment system for the OMC falls within the scope of WP7. The OMC budget is given in Table ??.

Prerequisites:

- frequency of sidebands on the output field,
- required suppression of higher-order modes and sidebands, especially also higher-order modes of sidebands, by the OMC,
- requirements on additional monitoring and locking outputs.

Deliverables:

1. optical layouts of output telescope and OMC,
2. requirements for output telescope and OMC mirrors,
3. procurement, characterisation and assembly of OMC,
4. installation of OMC and output telescope.

6.4 Main Interferometers

Current gravitational-wave detectors are using silica (SiO_2) mirror substrates with highly-reflective (HR) coatings made of stacks of SiO_2 and Ta_2O_5 doped with TiO_2 . Thermal noise of the HR coatings, which is proportional to the square root of the mirror temperature, limiting the sensitivity of the detectors, is the motivation for cooling the mirrors. This has not only implications on the coatings but also on the mirror substrates. The following sections will give an overview of the requirements on the mirror substrates and on the HR coatings.

6.4.1 Main Mirror Substrates

The mechanical loss of silica increases by several orders of magnitude when cooling it, as shown in Fig. 6.3. The thermal noise amplitude spectral density of the substrate $S_x(f)$, in which f is the

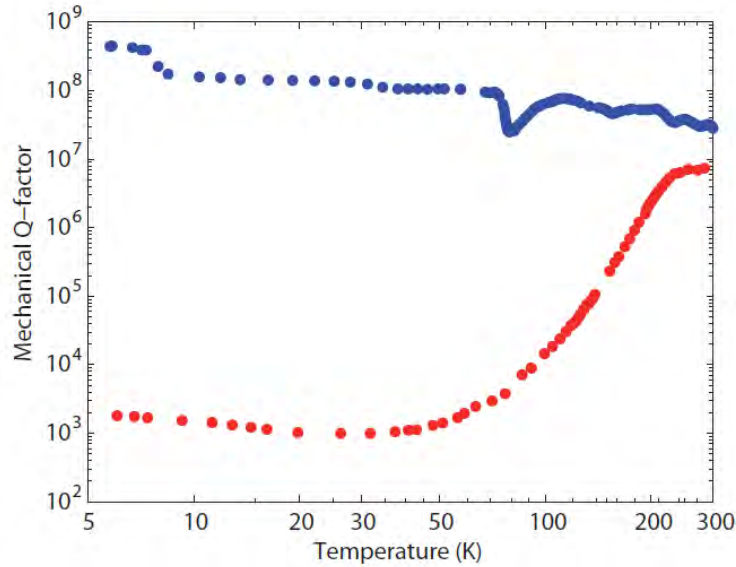


Figure 6.3: Q-factor (loss $\phi(\omega) = 1/Q(\omega)$) of SiO₂ (red dots) and of crystalline silicon (blue dots) as a function of temperature [30].

frequency, is proportional to the square root of the substrate mechanical loss $\sqrt{\phi_{sub}}$. Therefore, SiO₂ becomes unsuitable as a substrate material at low temperatures and silicon has been brought up as the material of choice for cryogenic detectors such as the (low-frequency) Einstein Telescope. Silicon shows a mechanical loss several orders of magnitude lower than that of SiO₂ at low temperatures [30]. A high thermal conductivity and low thermal expansion coefficient are of additional benefit resulting in low thermal lensing and thermo-elastic noise [31]. These and a number of other material properties are highly relevant for the choice of a test-mass mirror material, and within the ET Pathfinder we want to thoroughly test also the practical aspects of using silicon.

The projected budget for the main test-masses, as well as the beam splitters, is given in Tables ?? and ??.

Mirror Dimensions

Planned dimensions for the input test-mass (ITM) mirrors and the end test-mass (ETM) mirrors of ET Pathfinder are 15 cm diameter and 8 cm thickness, resulting in a mass of $1414 \text{ cm}^3 \times 2.329 \text{ g/cm}^3 = 3.293 \text{ kg}$ each.

Initial calculations were performed to arrive at a radius of curvature for the HR side of ITMs and ETMs, where both radii are assumed equal for cost saving reasons (more economical polishing, less spares). From the mechanical drawings, the distance between the centers of ITM and ETM chambers is 9.3 m, so that the distance between the two mirror surfaces is $L = 9.22 \text{ m}$, assuming perfectly centered optics. A *Finesse* simulation was set up to find mirror radii of curvature that lead to an optimally non-degenerate distribution of higher-order modes. In Figure 6.4, the resulting power built-up in higher-order modes is shown. Darker (bluer) colours correspond to lower mode orders, which have higher probability of carrying considerable power, while lighter (green-yellow) curves correspond to high mode orders, that are less likely to have significant intensities. A zoom shows the region around 14.5 m, where the next higher-order modes around the carrier resonance are of 8th and

13th order. A deviation from the radius of curvature by ± 0.1 m, as indicated by the shaded area, is unlikely to change the mode content significantly.

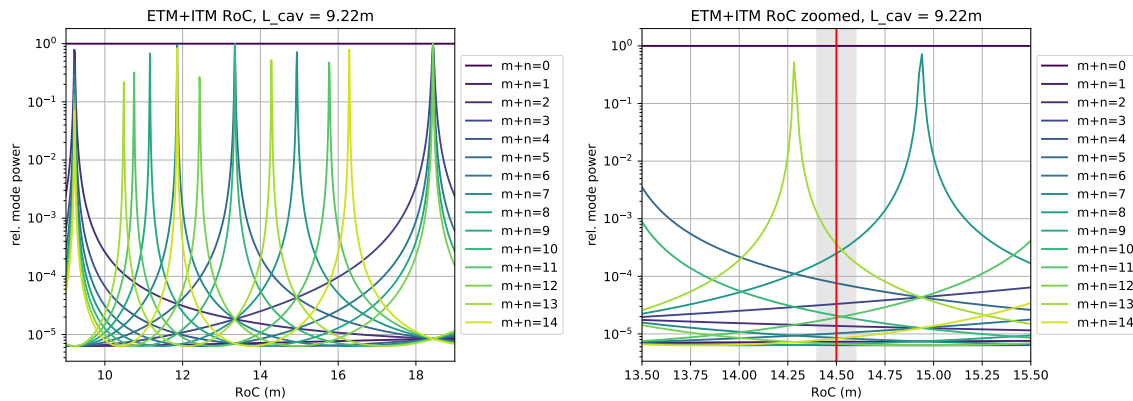


Figure 6.4: Higher-order mode built-up inside the arm cavities as a dependence of ITM/ETM radius of curvature. The right plot shows the region around 14.5 m.

For a radius of curvature of 14.5 m, the cavity g factor product is 0.13, and therefore well within the stable region. A plot of the beam waist and radius for different curvatures is given in Figure 6.5, at 14.5 m the waist will have a $1/e^2$ radius of 1.825 mm, while the beam radius on the test masses will be 2.21 mm.

Due to silicon's high refractive index (roughly 3.45 at 1550 nm and 2 μ m), the test masses will act as surprisingly strong diverging lenses. Therefore, the AR sides of the test masses will also need to be curved, at a similar radius of curvature as the HR side, to counteract this effect and end up with a nearly collimated beam. This can lead to a Virgo-style etalon in the test-masses; it will have to be further analyzed whether we want to exploit or rather actively avoid this. We will be able to extract locking/alignment signals for the arm cavities through the folding mirrors between the beam splitter and ITMs (see Fig. 6.2), so no wedge is required for this purpose.

A preliminary list of mirror geometry specification is therefore:

Dimensions

Diameter $150_{-0.5}^{+0}$ mm, thickness $80_{-0.5}^{+0}$ mm, total weight 3.293 kg

Side S1

curved, concave, radius of curvature (14.5 ± 0.1) m

Side S2

curved, convex, radius of curvature TBD

Chamfers

45° , 1 mm throughout

Markings

Side S1 indicated with engraved arrow on barrel, engraved serial number

Optical Absorption

One of the most critical material properties is the optical absorption of the crystalline silicon substrates as absorption causes heating which results in thermal deformations and heating of the substrates. While there will be only little power in the ETMs, the ITMs get transmitted by the full laser power.

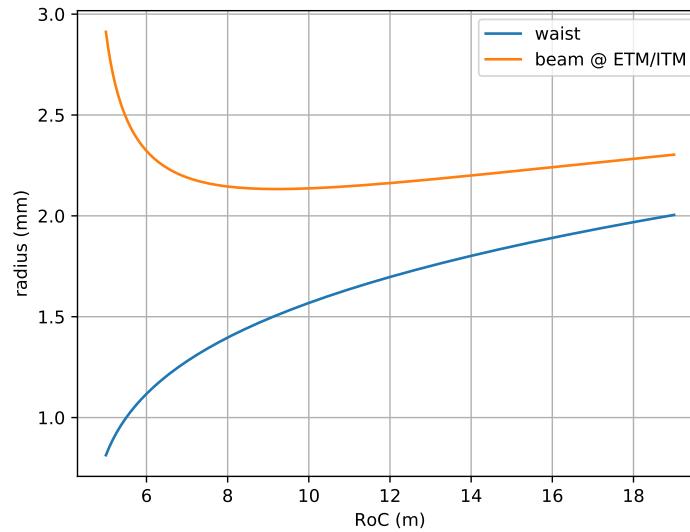


Figure 6.5: Arm cavity beam waist and beam radius on the test masses as a function of ITM/ETM radius of curvature. A laser wavelength 1550 nm is assumed.

For ETpathfinder, in the absence of power recycling and with moderate input power, a moderate absorption level would be tolerable. However, for the Einstein Telescope, extremely low absorption of the ppm/cm level is critical. In view of testing materials and techniques for the Einstein Telescope, we will therefore aim at sourcing material that is already as close to those specifications as possible.

Figure 6.6 shows the optical absorption of crystalline silicon as a function of wavelength as presented by Green and Keevers [32]. In the visible range, crystalline silicon is not transparent, and at a wavelength of 1064 nm, which is used in current gravitational-wave detectors, it is still as high as $\approx 10/\text{cm}$ (marked by the dashed, vertical line). Towards higher wavelengths, the absorption reduces significantly and was below a measurable level according to the data presented by Green and Keevers. This makes the telecommunications wavelength of 1550 nm, at which established laser systems and optical components are available, an attractive option for interferometers based on silicon mirrors.

To achieve such (or similarly low) absorption levels, extremely pure material is required as the optical absorption is proportional to the concentration of conducting electrons such as generated by dopants and other (unintentional) impurities [33]. A purity corresponding to $> 10 \text{ k}\Omega\text{cm}$ can result in an optical absorption in the ppm/cm (10^{-6}) range. The most common method for the production of mono-crystalline silicon is the *Czochralski* growth method (CZ-Si). However, standard CZ-Si has a maximum resistivity of $\approx 1 \text{ k}\Omega\text{cm}$ due to rather high oxygen content. For the purer *float zone* crystalline silicon (FZ-Si), an absorption of $\approx 2\text{--}3 \text{ ppm/cm}$ has been shown at 1550 nm at room temperature by Markosyan and Bell [34]. The resistivity of this material was $\approx 30 \text{ k}\Omega\text{cm}$.

The exact requirement on the optical absorption of the substrate material depends on the capability of the mirror suspensions to extract heat which in turn is related to the tolerable suspension thermal noise [35] and on other sources of absorption such as the optical coatings. However, it is certain that for the Einstein Telescope, the absorption of standard CZ-Si will be far too high and that the lowest absorbing-silicon on the market is needed.

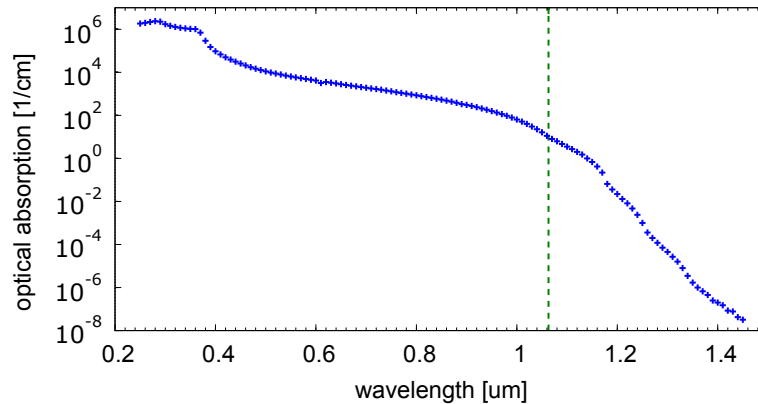


Figure 6.6: Optical absorption of crystalline silicon at room temperature (300 K) as a function of laser wavelength [32].

As a prototype, one of the goals of ETpathfinder will be realizing silicon mirrors with an absorption level as required for the Einstein Telescope. Pure FZ-Si can be produced in diameters of up to ≈ 20 cm and can provide the dimensions required for ETpathfinder mirrors. However, for the Einstein Telescope, diameters in the order of 50 cm will be required.

A possible option being investigated is so-called magnetic Czochralski (mCZ) silicon, which is grown in a magnetic field in order to remove impurities from the material. Test samples of mCZ silicon have shown an absorption similarly low as FZ-Si. While in theory, mCZ silicon can be produced in larger sizes than FZ silicon, low absorption has not been demonstrated yet on large-scale samples [34]. In order to develop mirrors for the Einstein Telescope, mCZ silicon mirrors are of interest for ETpathfinder.

Material properties, which are required to analyse the absorption measurements, are less accurately known at low temperatures and thermal effects, on which the measurements are based, are smaller. This results in large error bars of the low-temperature absorption data, of which the lower boundary would indicate not much change in the absorption with cooling, while a slight increase by about a factor of 2 towards lower temperatures is more likely for FZ silicon at 1550 nm [34].

Mainly motivated by the optical absorption of some potential coating material (see Sec. 6.4.2), higher wavelengths of around 2000 nm are of interest for the Einstein Telescope. The optical absorption of FZ silicon is about a factor of 2 higher at such wavelengths than at 1550 nm [34]. However, non-linear absorption effects are lower at a higher wavelength (= less photon energy).

Non-linear absorption

Two photon absorption (TPA) becomes relevant at high laser-light intensities. Due to low transmission of the ETM coating, it is mainly relevant within the ITM, which is transmitted by the full laser power. However, for cryogenic detectors, TPA can usually be assumed to be negligible due to relatively low intensities in order to maintain the low operating temperature.

Figure 6.7 shows the TPA as a function of laser power for a beam radius of 2.2 mm, as currently planned for ETpathfinder, based on a TPA coefficient of 5×10^{-12} m/W, as measured on pure FZ silicon by Bell [36]. For the Einstein Telescope, TPA will be significantly lower due to the large beam radius.

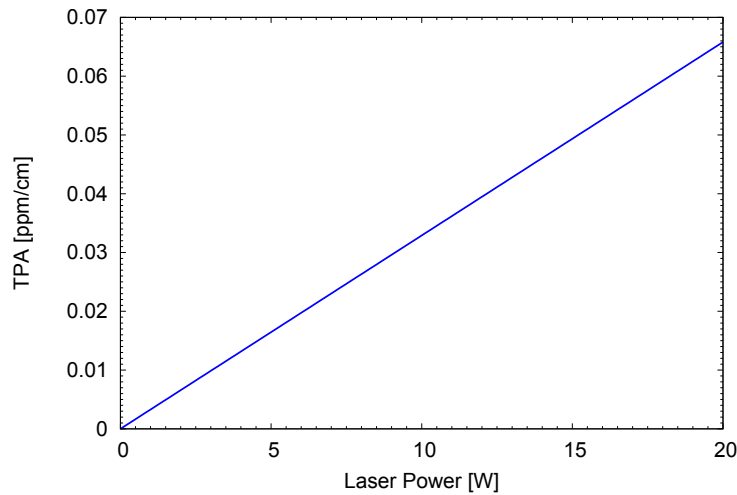


Figure 6.7: Optical absorption due to TPA as a function of laser power for a laser beam radius of 2.2 mm.

Optical Absorption on the Sample Surfaces due to Polishing

It has been observed that polishing of the silicon samples can cause optical absorption near the surfaces [37, 38]. The origin of this absorption has not been fully understood yet. The level of absorption is usually in the few tens to few hundreds of ppm/surface range and inhomogeneous across one surface. A procedure is known to reduce the absorption to a negligible level, however, this procedure has only been established for a rather low polishing quality of $\lambda/2$ and is not easily transferable to higher quality. The level of surface absorption for high polishing qualities, possible ways to reduce the absorption and the implication of remaining absorption on the mirror has to be studied.

Crystal Orientation

Crystalline silicon is commonly available in (100) and (111) crystal orientation. For (100) orientation, the mechanical loss has been shown to be slightly lower than for (111) orientation [39]. However, this difference in loss is insignificant for applications.

For the option of direct growth of crystalline coatings on the silicon substrates, the crystal orientation would be relevant in order to achieve lattice matching of the coating and substrate materials. However, for amorphous coatings, the substrate crystal orientation is not relevant. For the optical polishing (see Sec. 6.4.1), the crystal orientation might also be of relevance.

Birefringence has been shown to be negligible at 1550 nm for silicon in (111) orientation, even when extrapolated to ET-LF dimensions [40]. Literature does not provide a clear conclusion for a correlation of birefringence and crystal orientation (see [40] for detailed discussion), but indicates that literature values depend on sample geometry and treatment. Based on the investigation made in [40], birefringence is not expected to be an issue for ETpathfinder, but may need to be further investigated for other types of silicon than float zone (e.g. magnetic Czochralski etc.).

Surface Quality

The specifications of the interferometer-mirror are currently under investigation via dedicated numerical simulations. In the following we present the current best estimate of the mirror surface requirements for ETpathfinder 1a/1b. These are based on a mixture of the requirements of the

Glasgow speedmeter mirrors and Advanced LIGO using various parameter dependent scaling factors. Two zones are defined: Zone A is an area of 20 mm diameter in the center of the mirror (the laser beam will be ≈ 4.4 mm in diameter) and Zone B will be the remaining surface area, with a clear aperture of $> 90\%$.

Side S1 radius of curvature concave, (14.5 ± 0.1) m

surface error Zone A – LSF error < 2 nm for spatial frequencies 0.3 mm^{-1} to 1 mm^{-1} , HSF error < 0.3 nm pk-pk for spatial frequencies 1 mm^{-1} to 750 mm^{-1} , astigmatism < 8 nm.

micro-roughness < 0.1 nm RMS (super polish, best effort) for spatial frequencies above 750 mm^{-1}

surface defects Zone A – no more than 10 point defects larger than $2 \mu\text{m}$ and no scratches with a width $> 1 \mu\text{m}$, total area of defects $< 100 \mu\text{m}^2$;

Zone B – no more than 30 point defects larger than $2 \mu\text{m}$ and no more than 10 scratches with a width $> 1 \mu\text{m}$, total area of defects $< 2000 \mu\text{m}^2$

Side S2 radius of curvature concave, TBD

surface error better than $\lambda/10$ at $\lambda = 633$ nm

micro-roughness < 0.1 nm RMS (super polish, best effort) for spatial frequencies above 750 mm^{-1}

surface defects Zone A – no more than 20 point defects larger than $2 \mu\text{m}$ and no scratches with a width $> 2 \mu\text{m}$

flats 4 cm on each side, parallel to within 0.1 mm (2.5 mrad)

chamfers

polished, $1 \text{ mm} \times 45^\circ$

barrel

polished to standard optical quality

6.4.2 Main Mirror Coatings

Coating Reflectivity

Highly-reflective mirror coatings are made of stacks of layers of alternating high and low refractive index. In the simplest case, each layer has an optical thickness (geometric thickness multiplied by the refractive index) of a quarter of the laser wavelengths, at which the coating is designed to be reflective. In order to optimize the coating for a certain reflectivity, for reflectivity at more than two wavelengths, low thermal or thermo-optic noise or other properties, the layer thicknesses may differ from the simple quarter-layer design. As the refractive-index contrast of the two materials increases, the number of layers required to achieve a certain reflectivity decreases.

The coating materials used in current gravitational-wave detectors are silica (SiO_2) and tantala doped with titania ($\text{Ti:Ta}_2\text{O}_5$). For the initial ETpathfinder mirrors, reflectivities of $R_{\text{ETM}} \approx 99.999\%$ and $R_{\text{ITM}} \approx 99.9\%$ are planned. Figure 6.8 shows the schematic of a coating with $R \approx 99.999\%$ made of 16 double layers of silica (blue) and tantala (green) on a crystalline silicon (pink) substrate. The blue line shows the light-field intensity in the coating layers. All layers have an optical thicknesses of $\lambda/4$ for $\lambda = 1550$ nm.

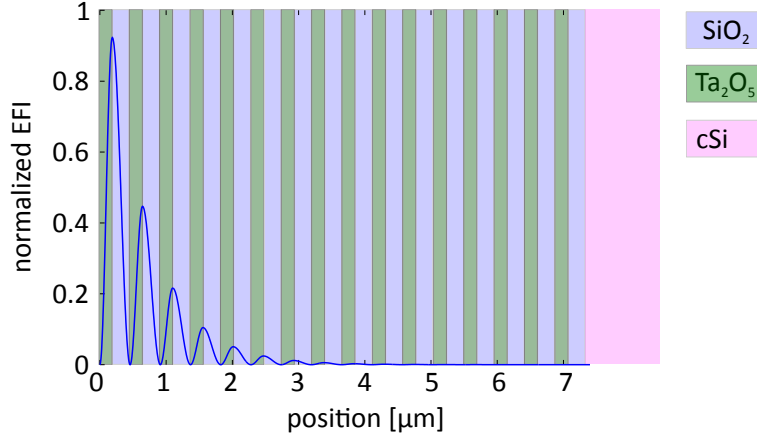


Figure 6.8: Schematic of a coating with $R \approx 99.999\%$ made of silica and tantalum layers on a silicon mirror substrate.

Coating Thermal Noise

Coating thermal noise, which is one of the main noise sources limiting current gravitational-wave detectors at their most sensitive frequencies, is given by

$$x(f) = \sqrt{\frac{2k_B T}{\pi^2 f} \frac{d}{w^2} \phi \left(\frac{Y_{\text{coat}}}{Y_{\text{sub}}^2} + \frac{1}{Y_{\text{coat}}} \right)}. \quad (6.4.1)$$

Here, k_B is the Boltzmann constant, T the mirror temperature, f the frequency, d the coating thickness, w the radius of the laser beam on the coating and ϕ the mechanical loss of the coating. Y_{sub} and Y_{coat} are the Young's moduli of the substrate and coating materials. This equation assumes that the mechanical losses associated with bulk motion and shear motion are approximately equal ($\phi_{\text{bulk}} \approx \phi_{\text{shear}} \approx \phi$).

In order to reduce coating thermal noise, the Einstein Telescope will use large laser beams and a low mirror temperature. However, thermal noise still will have to be reduced by reducing the coating mechanical loss, which is too high for silica and tantalum, and/or the coating thickness. In addition to low thermal noise, the coatings are required to have

- low optical absorption
- low scattering
- homogeneous thickness

Meeting all these requirements simultaneously is challenging and there are currently several research strands under investigation in order to develop coatings with improved performance. While coatings made of silica and tantalum meet the requirements of the initial ETpathfinder, at a later stage, new coatings for the Einstein Telescope will be tested. A selection of coating options, which are currently in the development phase are, is briefly introduced in the following sections.

Figure 6.9 shows coating thermal noise power spectral density of ETpathfinder for coatings made of silica and tantalum (on crystalline silicon substrates) with $R_{\text{ETM}} \approx 99.999\%$ and $R_{\text{ITM}} \approx 99.9\%$. At a wavelength of $2 \mu\text{m}$, coating thermal noise is higher than at 1550 nm due to thicker coating layers. However, for identical radii of curvature and detector arm length, the beam radius on the mirrors increases from 2.1 mm at 1550 nm to 2.6 mm at $2 \mu\text{m}$, resulting in very similar noise levels for the two wavelengths. These coatings meet the requirement of $\approx 10^{-18} \text{ m}/\sqrt{\text{Hz}}$ (arm length of $\approx 10 \text{ m}$).

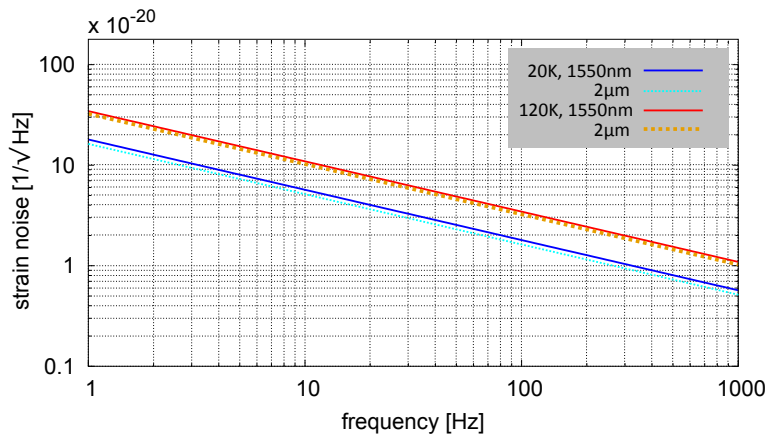


Figure 6.9: Calculated coating thermal noise of ETpathfinder (Phase 1a/b) for coatings made of silica and tantala.

Alternative Amorphous Coating Materials

In order to reduce coating thermal noise, alternative amorphous materials are under investigation. Some examples are:

- Amorphous silicon (aSi) is a material with a very high refractive index, resulting in a reduced coating thickness, and a low mechanical loss at low temperature (about 40 times lower than that of tantala at low temperatures). However, the optical absorption of aSi has to be further reduced for use in GW detectors [41].
- Silicon Nitride (SiN_x) has a refractive index similar to tantala and could be used as a high index material. However, it also could be used as a low index material with aSi. The refractive index can be varied by changing x . The mechanical loss of SiN is similar to that of aSi and the absorption slightly lower. SiN is commonly produced via vapour deposition, but it is also possible to produce IBS SiN [42, 43].
- Hafnia doped with silica has a mechanical loss about a factor of 2 lower than that of silica at low temperatures, while the refractive index is closer to that of tantala. The absorption is slightly too high. Unwanted crystallization prevents the use of undoped hafnia [44].

Alumina, germanium, titania, various different dopants and doping concentrations for tantala [45, 43] and nano-layered coatings [46, 47], in which each coating layer has a sub-structure of thinner layers to modify a material's crystallisation temperature, are also amongst possible coating materials for ET and other future detectors and therefore may be of interest for being tested in ET Pathfinder at a later stage.

Multimaterial Coatings

The upper layers in a coating contribute significantly more to the optical absorption than the lower layers (see Fig. 6.8), while the lower layers contribute slightly more to the mechanical loss than the upper layers. Multimaterial coatings combine more than two materials in a multilayer coating in order to optimally exploit their properties [48, 49]. These coatings are a possible solution in order to use the amorphous coatings listed above.

Crystalline Coatings

Many crystalline materials show lower optical absorption and mechanical loss than amorphous materials. However, the low and high refractive-index materials have to be lattice matched, which limits the number of possible materials significantly. Crystalline coatings made of AlGaAs and GaAs are under investigation and show promising performance [50]. The requirement of a lattice matched substrate – GaAs wafers in case of AlGaAs coatings – for the growth procedure requires a transfer of the coating to a suitable substrate (e.g. SiO₂ or cSi) after production and also can limit the maximum coating size (to ≈ 20 cm in case of GaAs). Defects in the bond for attaching the coating to the new substrate can lead to the coating detaching during the test-mass cooling procedure or to thermal noise from a change in bulk and shear loss.

Alternative materials may solve some of these problems (e.g. AlGaP and GaP coatings can directly be grown on cSi). For more details see the Sec. 6.5.

6.4.3 Coating Uniformity

For uniformity, two different aspects have to be considered: (i) The thickness uniformity of the total coating stack across the large mirror affects the mirror surface parameters. (ii) Thickness variations within individual coating layers can affect the transmission performance of the coating. Of particular relevance is a very similar transmission of the two ITM mirrors, because these define the arm cavities' finesse values, which must be closely matched.

The coating specifications of the aLIGO mirrors were

- flatness after HR coating: < 0.5 nm RMS in the central area (identical to the polishing specification),
- < 50 ppm round trip losses,
- and transmission matching for ITM (at 1064 nm): $\Delta T < 0.01\%$ with $T = 1.4 \pm 0.1\%$ [51].

These specifications were met for silica/tantala coatings made by LMA [51]. To achieve transmission matching, the two ITMs had to be coated simultaneously in the same coating chamber. Similar specifications are desirable for the ETpathfinder coatings, with $T_{\text{ITM}} \approx 0.1\% \pm \text{TBD}$.

A thickness uniformity of < 0.5 nm RMS has also been shown for crystalline AlGaAs coatings [52].

6.5 Novel Mirror Coating Development

Part of the approved ETpathfinder proposal is a contribution to the capital funding for the construction of a novel MBE coating facility at Leuven University to investigate new crystalline coatings for application in future GW detectors and ETpathfinder. In the following sections a detailed motivation and description of this activity is given.

6.5.1 Main Activities

Oxide Molecular Beam Epitaxy

Currently, the main methods to create state of the art oxide mirror coatings are based on Sputtering and Ion Beam (Assisted) Deposition (IBAD) techniques. There is already quite a large group of laboratories worldwide that focuses their efforts on using these techniques for oxide mirror coatings.

The Oxide Molecular Beam Epitaxy (MBE) technique is an interesting addition to the portfolio of techniques for mirror coatings and presents several unique and complimentary advantages. This technique has matured well over the past 30 years and the participants in the ETpathfinder project have build 3 generations of small or large area oxide MBE systems [53, 54].

Overall principle

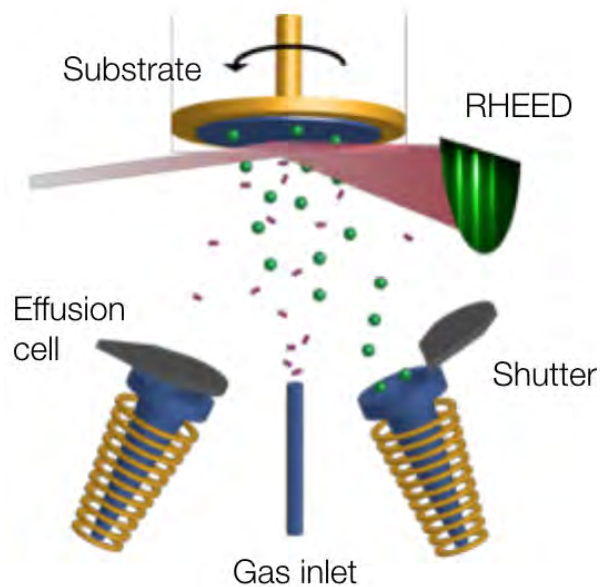


Figure 6.10: Schematic drawing of the main elements in a standard molecular beam epitaxy system.

The overall principle of MBE is illustrated in Figure 6.10. In short, a rotating and heated substrate is bombarded with a beam of atomic or molecular (precursors) species emanating from for instance an effusion cell. An effusion cell is essentially a crucible in which the material to be evaporated is inserted combined with a heating element wrapped around it and a shutter that opens and closes the path to the substrate. The deposited species on the substrate then react with oxygen species (atomic oxygen, molecular oxygen or ozone) emanation for instance from a gas inlet, to form an oxide film. The structure of the growing film is then monitored in real-time using an electron diffraction pattern created on a screen with a technique called Reflection High Energy Electron Diffraction (RHEED).

Compared to other techniques, the main advantages of oxide MBE include:

- A low background (10^{-11} Torr) and operational pressure (10^{-8} - 10^{-5} Torr). This enables an excellent control on (gaseous) contamination as well as oxygen content in the layers. For instance it allows to grow suboxides, i.e. oxides that do not have the highest oxidation degree; but many of which have a higher refractive index. In addition, it permits a good control on the oxidation modulation in a coating. A good example would be the case of combining aSi with an oxide as mentioned above. Nevertheless if a higher oxidation state is required then atomic oxygen or ozone gases are added.
- A low energy deposition process in the sense that energetic species - as is typical in sputtering

in IBAD - are not present during growth. Indeed MBE uses elemental thermal evaporation from sources operating at a maximum of 3000C or about 0.75 eV. Typically higher energetic growth processes are more prone to the appearance of 3D features and particles on the growing surface. In addition, diffusion reactions are also enhanced which can lead to a poorer control on interface sharpness and roughness.

- An excellent uniformity control at or below 1 %. The main sources - effusion cells and electron beam guns - are essentially point sources. This means that a simple geometric relation exist between the source and the evaporation profile. Hence, to improve uniformity over large areas requires only to change the geometrical position of the source vis-a-vis the substrate. Interestingly, it does not need the uses of larger targets as might be required in large area IBAD or sputtering processes.
- A directed "beam" deposition. The low pressure operational conditions ensure that the evaporating beam has molecular beam properties. This means that atoms evaporating from the hot source surface are not scattered on their path to the substrate. This has several advantages. First, it means that the beam can be directed only towards the substrate and that no atoms hit - and contaminate - the walls of the chamber. Accumulation of such "debris" deposits on chamber walls can be a main source of subsequent particle contamination in the coatings which then necessitates frequent cleaning of the chamber. Second, it enable to easily shape the coatings in a well defined manner, through the use of shutters and the substrate rotation. For instance composition-graded or thickness-graded profiles can be grown while conserving rotational symmetry. As an example, a rotational symmetric "curved" coating can be made whereby more substrate material is deposited at the edges.
- In-situ thin film characterisation tools. Because of the low operational pressure several unique tools can be used to monitor the deposition process such as the beam fluxes and the growing film surface. The beam flux techniques include quadruple mass spectrometry (QMS), electron impact emission spectroscopy (EIES) and ionisation gauges. With these the composition of the evaporants to the substrate can be controlled with high precision ($\approx 1\%$). The film structure (roughness, crystallinity) can be measured in real-time using reflection high energy electron diffraction (RHEED) while the film composition can be measured using the x-rays emitted from the RHEED gun with a technique called low angle x-ray spectroscopy (LAXS). The RHEED technique becomes very important if the goal is to grow crystalline oxides.

The unique advantages of MBE apply to all types of coatings that can be made whether metals, semiconductors, oxides, nitrides, etc. Furthermore, they also apply to both amorphous as well as crystalline oxides. Nevertheless given the availability of in-situ characterisation tools, the biggest impact that can be made in this field with a new coating tool is related to exploring crystalline oxides.

Crystalline coatings

The motivation to explore crystalline oxides is similar to that used by the Cole et al. [50], namely that the thermal noise of single crystals is currently still several orders of magnitude better than that of amorphous coatings. While single crystals can have very low mechanical loss angles of the order of 2×10^{-9} (Al_2O_3) or 5×10^{-9} (SiO_2), the values for their amorphous coating counterparts is at best around 5×10^{-5} for state of the art materials. Furthermore, there are a number of interesting features of oxide single crystals that may offer unique advantages in specific situations such as:

- Explore tensor properties. The unique features of crystals are often tensor properties in contrast to those of amorphous materials. While the latter can typically be described by values averaged over the 3 crystal axes, this is often not the case for the crystalline materials. This can be a blessing, for instance when the anisotropy of the thin film properties can be used to compensate those of the substrate. The relevant properties here are the elastic, thermo-optic and thermal expansion coefficients.
- Tailoring thermal expansion. While most materials have positive thermal expansion coefficients along the three crystallographic axes, there are quite a number of materials that have anisotropic coefficients whereby the thermal expansion coefficient is negative (NTE) along one direction. To date the highest NTE reported is $-1.3 \times 10^{-4}/\text{K}$ which is about 200 times larger - in absolute value - than the PTE of fused quartz. That means that in principle such a $500 \mu\text{m}$ thick NTE coating may completely compensate the PTE of a 10 cm thick fused quartz mirror.
- Controlling the uniformity of elastic properties. While the origin of the mechanical losses in coatings are not fully understood or identified, it is reasonable to estimate that non-uniformity in structure and composition are some of the main culprits. Both have an immediate effect on the local elastic properties. Although on a macroscopic scale the elastic properties of thin films are usually considered uniform they are most definitely not uniform on a microscopic / atomic scale. Such local non-uniformity are for instance structural defects like dislocations, anti-phase grain boundaries, vacancies, interstitials, variations in local composition, density variations, etc. Hereby not only elasticity in terms of its static components - with properties such as Young's modulus, Poisson's ratio, etc. - must be considered but also its dynamic components like the velocities at which elastic waves propagate in solid media.
- Large family of interesting compounds. The amount of interesting oxide binary, ternary, quarternary, etc. materials is quite large compared to the crystalline AlGaAs and AlGaP compounds. Two families stand out namely the corundum type (R_2O_3) as well as the perovskite (ABO_3) type. The hexagonal corundum compounds include for instance Al_2O_3 , Cr_2O_3 , Fe_2O_3 , Ti_2O_3 , V_2O_3 , Ga_2O_3 and In_2O_3 . Within these materials it is also easily possible to create intermediary alloys, such as $(\text{Cr}_x\text{Fe}_{1-x})_2\text{O}_3$ or $(\text{Ga}_x\text{In}_{1-x})_2\text{O}_3$. Here, the in-plane lattice parameters spans a broad range between 0.476 nm - 0.549 nm, while the refractive index (at 1064 nm) varies between 1.75 to 2.80. Epitaxial films of these materials can be grown on sapphire or on Si(111) substrates. The perovskite family of compounds - like SrTiO_3 - is even much larger and can be well grown on Si(100) substrates. Note that there is also quite some structural variability within the perovskites that can be either cubic, tetragonal or orthorhombic.
- Use of strain engineering. Thin crystal films can be quite easily deformed in a uniform and homogeneous manner through the use of epitaxial strain. This means that the lattice parameters of a substrate - or of a thick buffer layer - can be imposed on the subsequent films. In such a case, the film lattice parameters - and all its other properties - can be tailored within a well defined range until optimal features are obtained.

Alignment with other coating activities

An important remark is to note that many of the above mentioned materials have not been considered and/or have only been partially tested for their use into GW coatings. Specifically, the temperature dependent optical and elastic properties of these thin films will need to be measured. Therefore, it will also be imperative to align these activities with ongoing coating developments in

the LIGO/VIRGO consortia where a large amount of relevant experimental techniques and expertise are available.

Epitaxial oxides on Silicon

Since about twenty years there has been steady progress in the growth of epitaxial oxides on Silicon. Despite many different efforts and approaches the best quality films still rely on epitaxial SrTiO_3 buffer layer [55–58]. In order to create this buffer layer, a set of specific conditions is necessary. This includes: i) perfect cleaning of the silicon wafer, ii) creating a dedicate surface reconstruction of the silicon surface, iii) depositing a fractional monolayer of strontium metal, iv) creating a strontium silicide interlayer before v) finally starting the deposition of SrTiO_3 . A schematic illustration of the silicon - SrTiO_3 interface is shown in Figure 6.11.

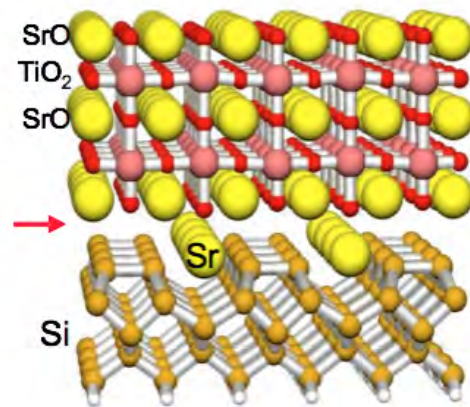


Figure 6.11: Schematic illustration of the silicon - SrTiO_3 epitaxial buffer.

Note that over these twenty years there have been many attempts to perfect this approach as well as to try to implement it using all the different deposition schemes available in the literature. To date however, the stringent requirements listed above have only yielded excellent quality single crystal oxides films with MBE.

6.5.2 Infrastructure components

Based on the above challenges, there are quite a few elements that need to be considered when defining the appropriate tooling to grow the thin film coatings. Both the individual elements as well as their combination will contain a number of technological innovations necessary to produce the high quality films needed for this application.

Sources

Typically each element to be deposited requires its own source. Such a source can be an effusion cell - as illustrated above - an electron beam evaporator or a gas inlet system for gaseous (molecular/chemical) precursors. Each of these sources can come in different flavours. For instance under the umbrella of effusion cells, we have high temperature cells, low temperature cells, dual

filament cells, cold-lip cells, valved crackers, etc. Among the different constructions of electron beam evaporators we have single crucible, multiple crucible as well as vertical evaporators. Depending on the amount of heat these sources produce, they are contained with a water cooled enclosure. A schematic drawing of an electron beam evaporator is shown in Figure 6.12 (left).

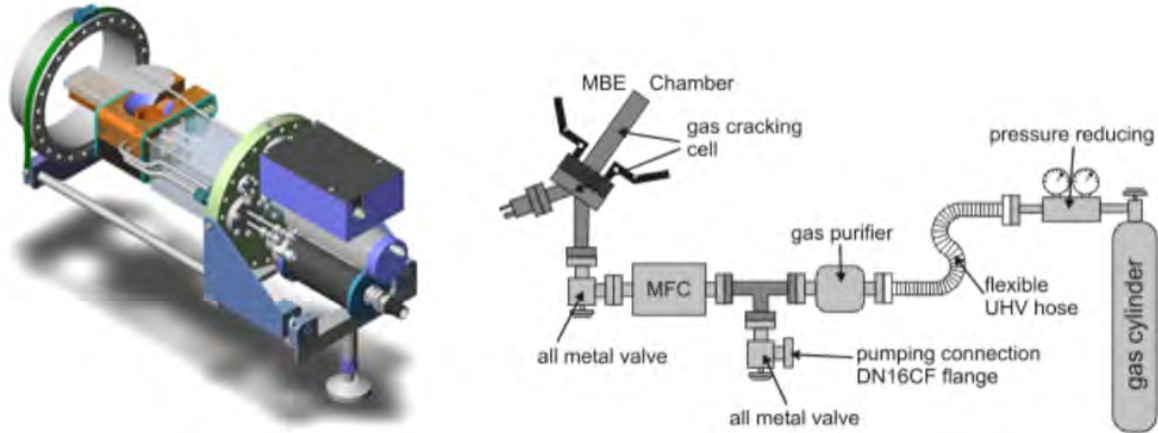


Figure 6.12: Schematic drawing of an electron beam evaporator (left) and a gas injection manifold (right).

Also for the gaseous species injection there are a range of possible designs and options. One such gas manifold is illustrated in Figure 6.12 (right). Depending on the type of gas to be used, instead of a gas cylinder a gas bubbler may be used and the gas lines might required to be heated. The bubblers are typically used when the gaseous precursors have a low vapor pressure. In that case the mode of operation is to use a (inert) carrier gas - such as nitrogen or argon - that is flown through the heated bubbler that contains the precursor. The overall principle of a bubbler system - with the mass flow controller (MFC) that controls the gas flow rate - is illustrated in Figure 6.13 (left). Note that in a typical system, several gas lines and manifolds will be put together in a rather complex system.

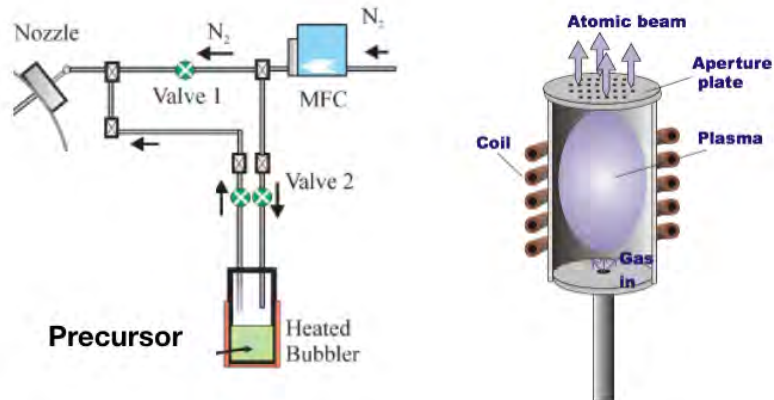


Figure 6.13: Schematic drawing of a precursor bubbler system (left) and an atomic beam source (right).

Another important element is a source of reactive and/or highly energetic species. This can be performed by a range of different sources, mostly involving the creation of plasma's and/or high

energy ion beams. One such radio frequency (RF) plasma source is depicted in Figure 6.13 (right) where an oxygen plasma is generated inside a crucible leading to the generation of a relatively high amount of atomic oxygen (up to 30%) which then flows out through an aperture on top. Other implementations make use of a electron cyclotron resonance (ECR) to create a plasma. Furthermore when grids are added on top of these sources, then the application of a voltage allows to extract electrons or ions from the plasma leading to an ion source.

Vacuum and pressure control



Figure 6.14: Pictures of a cryopump (left), a turbomolecular pump (middle) and an ion pump with titanium sublimation filaments (right).

The base pressure inside an MBE system is typically of the order of 10^{-11} Torr. This requires a range of pumping systems including cryopumps, turbomolecular pumps and their forepumps, ion pumps equipped with titanium sublimation filaments as well as liquid nitrogen cooled cryopanel. In standby operation, mostly the ion pumps with titanium sublimation and the cryopumps are active. However during film growth where the temperature inside the chamber increases and a gaseous oxidizing flow is necessary then the turbomolecular pumps are active while the others are valved off. Schematic pictures of the different systems are shown in Figure 6.14.

The liquid nitrogen that feeds the cryopanel of the system require a specific set of double walled vacuum tubings that transport the liquid nitrogen and a phase separator. The latter recovers part of the liquid and separates it from the hotter gas that comes back after circulating through the panels. This concept is illustrated in Figure 6.15 (left).

The pressure in the different vacuum chambers is measured using a variety of instruments including ion gauges, Pirani gauges, baratrons, and residual gas analysers. The latter is used to monitor the composition of the base pressure as well as to detect small vacuum leaks and contaminations. The ion gauge and Pirani gauges are shown in Figure 6.15 (middle and right).

Flux control

In an MBE system, thin films of compound materials are formed by the combination of evaporants from different sources on the substrate. Hence it is quite essential to control the evaporation rate of each of the evaporants precisely. This is done by a combination of several techniques each with their



Figure 6.15: Pictures of a liquid nitrogen feed lines coming from a phase separator (left), an ion gauge (middle) and a Pirani gauge filaments (right).

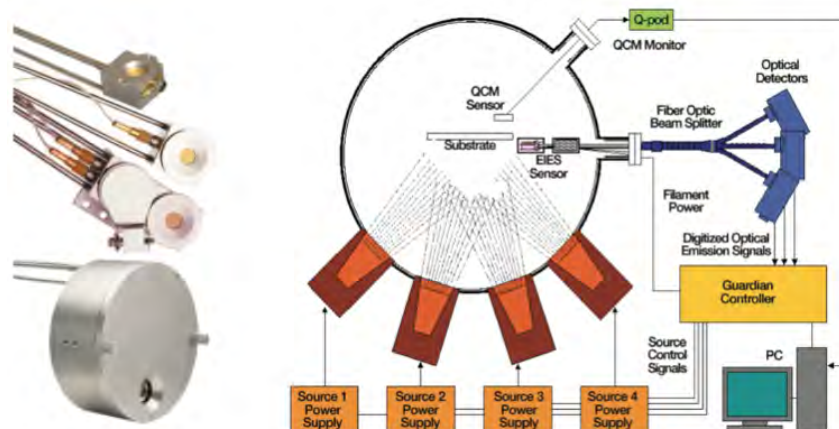


Figure 6.16: Examples of quartz crystal monitors (left) and an EIES system (right).

advantages and disadvantages.

Quartz crystal monitors use the measurement of a resonant frequency of a quartz crystal that shifts when material is added to its surface. Such monitors are used in many deposition processes and provide a good estimation of the flux rate. However since the conditions of deposition on the quartz surface are not the same as on the substrate - difference in temperature, sticking coefficient, oxidation coefficient etc. - it is not always the best technique. Furthermore its sensitivity is a strong function of temperature which can induce additional errors. Some examples of quartz crystal monitors are shown in Figure 6.16 (left).

Hence in most MBE system addition flux monitors are added for instance based on optical spectroscopy. In the case of Electron Impact Emission spectroscopy (EIES), the flux of atoms or molecules is ionised under electron bombardment which results into the emission of light. In this case, different elements will give rise to a different emission spectrum. Using a combination of fiber optic beam splitters and optical detectors, the spectrum can be collected and used to control the deposition process as illustrated in Figure 6.16 (right).

Other optical techniques are based on laser fluorescence or on atomic absorption spectroscopy

(AAS). Both of these methods have the advantage that no equipment - besides optical windows - needs to be added inside the deposition chamber since only interactions with light are important. An example of an implementation using AAs is shown in Figure 6.17 (left).

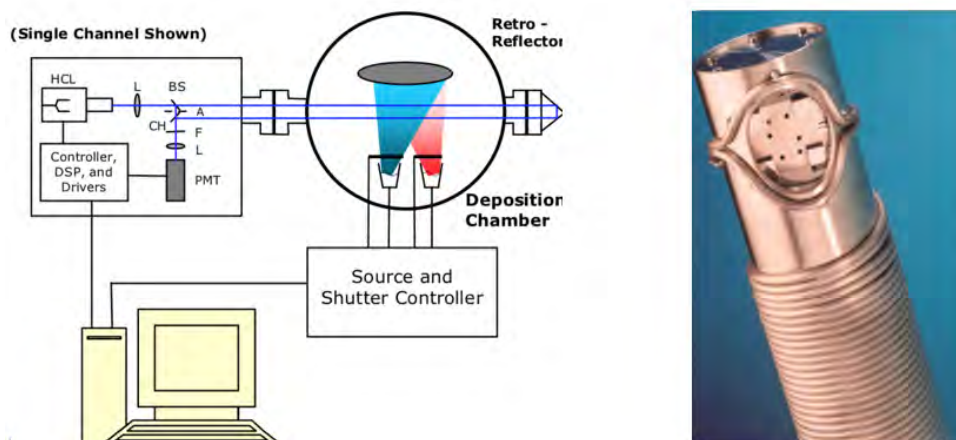


Figure 6.17: An implementation of AAS (left) and a picture of a cross-beam ion source as part of a QMS system (right).

Although optical methods provide quite a flexible implementation, they are not the most sensitive instruments and for instance in the case of growing films with small doping levels, that sensitivity is not sufficient. An additional method is then to use quadrupole mass spectrometry (QMS) systems equipped with specialized ion sources. The ion sources have a cross-beam design to ensure that no evaporants are deposited on the inside of the source. Using special pulse counting techniques, such systems are the most sensitive tools for this application.

In-situ thin film / crystal formation control

While the flux controls mentioned above enable to control the impinging amount of material on the substrate, this does not provide a characterisation of the growing films. Many factors play a role in determining the crystal phases, orientations, roughness, etc. These are a function of the temperature, oxidation coefficients, sticking coefficients, re-evaporation rates, etc. Hence it becomes important to use methods to monitor the growing material on top of the substrate.

There are multiple methods that are being used for this that are based on electron, photon and/or x-ray beams, impinging upon or emitted from the growing films. One technique using electron diffraction (RHEED) is already mentioned and illustrated above in Figure 6.10. This technique enables to control the crystal phases that are formed but does not give direct information about the composition of the films.

Another technique that uses the same electron source to bombard the surface and to collect the emitted element specific x-rays is low angle x-ray spectroscopy (LAXS). This technique is specifically designed to measure the surface chemical composition and to detect in-real time deviations from the overall stoichiometry and is illustrated in Figure 6.18 (left).

The above techniques monitor what happens at or near the surface of the growing film. However during deposition process - certainly at high temperatures - a number of processes can take place

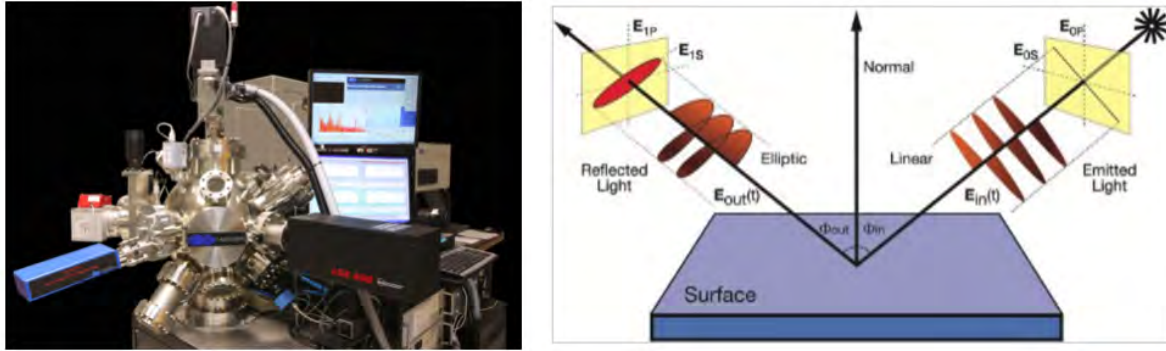


Figure 6.18: An implementation of LAXS (left) and a schematic picture of an ellipsometry measurement configuration. (right).

below the growing surface such as reactions with the substrate or among the different layers or further oxidation processes, etc. To monitor those, one uses optical methods that have a much higher penetration depth than the electron beams from the preceding paragraph.

One such method is spectroscopic ellipsometry (SE), a technique that measures the light polarization rotation as a function of the interaction with a thin film. The principle is illustrated in Figure 6.18 (right) and this method allows to extract and monitor the refractive index and extinction coefficient as a function of the thin film thickness. Both of these quantities are essential parameters in the design of mirror coatings and can thus be accessed in real-time during the growth.

Thin film temperature and strain control

In most thin film deposition system, the substrate and thin film temperature is induced by light radiation for instance from a hot filament or from a laser source. To measure the substrate temperature itself is not as straightforward since in most cases the substrate rotates which makes the use of thermocouples or resistive temperature sensors impossible. The most common method is to make use of light emission or pyrometry. This requires knowledge of the spectral emissivity of the substrate which is known or can be calibrated. One of the issues is that the filament radiation - as a function of wavelength - is partially absorbed and thus can reach the pyrometer and can interfere with the temperature measurement.

As thin films grow, part of the radiation is now also absorbed in the film and the spectral emissivity becomes dominated by the thin film itself instead of the substrate. One method to then monitor the substrate temperature is to measure the band gap of the film, which is also a function of the temperature. In principle this can be done by SE but there are also dedicated tools for this on the market such as the EpiTT from Laytec as depicted in Figure 6.19 (left).

Another critical parameter - certainly for thick films - is that of strain control. A large lattice and thermal expansion coefficient mismatch between film and substrate often leads to films which show cracks and a high density of other defects. To minimize the amount of strain being build up during growth and cooling it is important to be able to measure this in-situ. This is typically done by measuring how the entire wafer (substrate + film) curves up or downwards or in other words to determine the amount of bow. Such an instrument is shown in Figure 6.19. The amount of strain can then be tuned partially for instance through changes in composition.



Figure 6.19: An implementation of a substrate/thin film temperature pyrometer (left) and a substrate bow measurement device (right).

Beam of energetic particles

An alternative method to control the strain and the overall density of thin films is to make use of ion bombardment. For instance in plasma assisted deposition, the properties of the plasma can be used to control the amount and even the sign of strain in the thin films. A part of this is related to the energy transfer from the energetic beam to the film and another part can be due to the implantation of extra species (oxygen, nitrogen, argon, etc.).

A further advantage of using energetic species is that they can improve the density of thin films (amorphous as well as crystalline). This principle is illustrated in Figure 6.20 and is one of the main features of the ion beam assisted deposition (IBAD) technique, which is the standard technique used for GW mirror coatings.

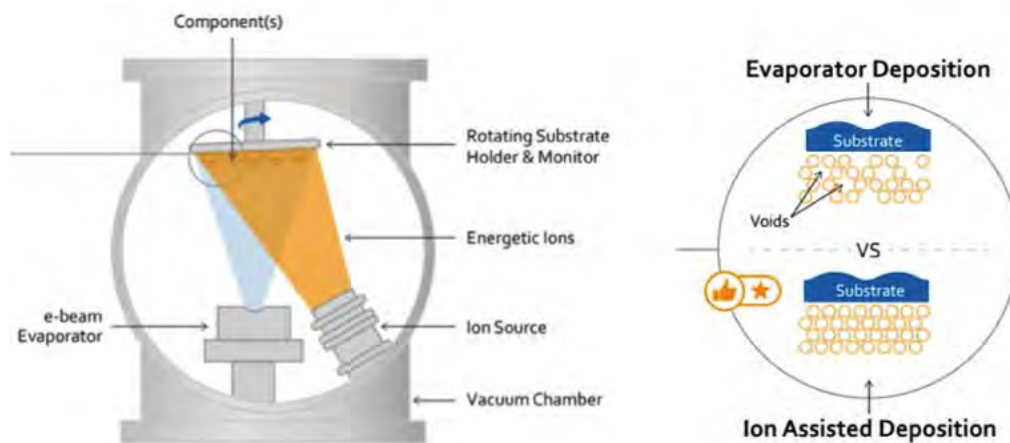


Figure 6.20: An implementation of an ion beam inside an evaporator (left) and the densification process that it induces (right).

In-situ annealing

Crystal growth of thin films in general requires higher temperatures than their amorphous counterparts. This high temperature step can then either be applied during the growth or after the growth is finished. To minimize diffusion and reaction process either among the different layers or with the substrate, the goal is to expose the layers to a high temperature set for an as short a time as possible. Such approaches aiming to minimize the thermal budget to which the films are exposed are commonly called rapid thermal annealing (RTA).

There are a number of different annealing implementations available on the market. One approach uses for instance high intensity pulsed lasers and another uses flash lamps. This variety is necessary to control precisely the annealing duration as well as the photon wavelength that is used. Depending on the band gap and the optical properties of the materials to be annealed light of different wavelengths will be absorbed differently.



Figure 6.21: A rapid thermal annealing chamber with heating lamps (left) and a wet processing unit to clean wafers (right).

The RTA process could in principle be done in the deposition chamber. However, the specifications of the heater and chamber environments for RTA are quite different from those of a typical substrate heater specially since a much higher amount of thermal power needs to be supplied and evacuated. Also the gaseous environment in which the annealing is performed plays a crucial role since it may need to be performed in an oxygen, nitrogen, or an inert ambient pressure for which a deposition system is not designed. As a consequence in most systems, RTA takes place in a separate and optimized chamber. Such a chamber equipped with heating lamps is shown in Figure 6.21 (left).

In-situ substrate cleaning

Before the thin film growth process starts it is important to clean the silicon substrates in order to remove an amorphous silicon oxide surface layer, but also to eliminate organic residues, particles, etc. This is typically done using a series of wet chemistry processes such as dipping in cleaning solvents as well as in a buffered HF solution for a short time. After cleaning the wafer needs to be transferred to the vacuum system as soon as possible to avoid re-oxidation and contamination for instance due to the adsorption of water vapour. The Figure 6.21 (right) shows a wet chemistry processor that can be used for these purposes. Note that these are not optimal solutions since it usually takes quite some

time before the wet solution is removed from the wafer and it is dried. Recently some in-situ dry cleaning processes have been developed and this will be the preferred solution if available.

Load lock, Wafer Transfer and Storage

An ultrahigh vacuum deposition system can never be an isolated chamber otherwise any time a sample is transferred inside the chamber, it would need to be vented then pumped and backed out before the required base pressure is obtained again.

Therefore, the main deposition chamber is connected with a set of chambers that enable to transfer a wafer from the ambient atmosphere through a series of glove boxes, load locks, pumping stages, transfer systems and wafer storage units. Depending on the final system configuration, the transfer systems also connect to the RTA chamber, the in-situ cleaning unit etc.

Note that these wafer transfer requirements can turn out to be quite complicated. For instance in most RTA systems the wafer is facing upwards, while in an MBE system it faces downwards. To transfer the wafer from the RTA to the MBE then requires an 180 degrees flip operation under ultra high vacuum conditions. This can be performed either in a vacuum flipping station or as part of a standard atmospheric robot handler called a front opening universal pod (FOUP).

6.5.3 Experimental setup

There is no final layout available of the experimental setup yet as this will be part of the design process as well as depending on total cost. A draft layout is shown in top view and side view in Figure ??, while the costing is given in Table ??.

6.6 ETpathfinder Auxiliary Optics and related Infrastructure

6.6.1 Optical Tables

Next to each vacuum chamber, we will require an optical table to accomodate

- the main laser system,
- auxiliary laser inputs and outputs, such as optical levers,
- laser beam distribution for readout systems such as auto-alignment systems, spot position monitors, wavefront sensors and cameras.

These tables will have to be installed either directly at beam height, or will require periscopes to bring beams from the tanks onto a suitable working height. In addition, five more optical tables will be required throughout the ETpathfinder hall to test, set up and preinstall components, e.g. for pre-assembly and alignment of suspension systems before they are installed in the main vacuum envelope. A budget for these tables is given in Table ??.

6.6.2 Clean Workspaces

Since the main cleanroom is of only moderate cleanliness level, we will foresee several clean laminar-flow work benches that can be used to prepare and assemble delicate optics in a dust-free environment. They are budgetted in Table ??.

6.6.3 Viewports

The vacuum system requires a sufficient number of viewports to be able to extract beams for sensing, alignment and monitoring purposes. We foresee a total of 8 large CF250 AR-coated viewports, most

of which will be attached to the two input optics chambers. An additional 12 CF100 viewports will be used for additional optical access and/or non-horizontal viewing into the chambers.

Each of the 8 test-mass mirrors will have position sensing via optical levers, of which 3 are required per test-mass. The respective beams will have to enter and exit the vacuum system, which leads to 5 CF100 view-ports (one can be shared by two beams) per test-mass, so 40 view-ports in total. The corresponding budget is listed in Tab. ??.



7. WP7: Controls

7.1 Overview of the Control WP

The Control work package contains the hardware and software that is used to implement the many control loops that are needed to operate ETpathfinder. It also contains some of the development and production of electronics that form the optical and mechanical transducers needed in WP5 and WP6. Finally, it takes care of acquiring and storing all relevant signals for online and offline monitoring.

7.2 Introduction

Gravitational wave interferometers are complex opto-mechanical systems, which only obtain their ultimate sensitivity when several optical path lengths are controlled to within a tiny fraction of a wavelength to keep multiple cavities simultaneously at resonance. The cavities are formed by mirrors that are suspended by complex seismic isolation systems. This seismic isolation is partially passive, but needs an active part as well to avoid excitation of internal resonances. Active feedback control is therefore an integral component of Gravitational Wave interferometers.

In the past, this was mostly done using analog electronics, but these days all but the fastest loops are implemented using *hard real-time* digital systems. In this chapter, we will describe the essential components of such a control system and matching data acquisition system. Although there will be differences in scale and requirements between a km-scale observatory and a 20 m prototype facility, there are large similarities, since the number of cavities and suspensions is about the same. To arrive at an actual implementation of this system we can therefore rely heavily on experience and equipment used for controlling the existing GW observatories and test facilities.

7.3 Control system components and requirements

7.3.1 Control loop hierarchy

To better explain the required control system for a complete interferometer, we will start by looking at a simplified scheme of the control of a single suspended Fabry-Perot cavity, as shown in Fig. 7.1.

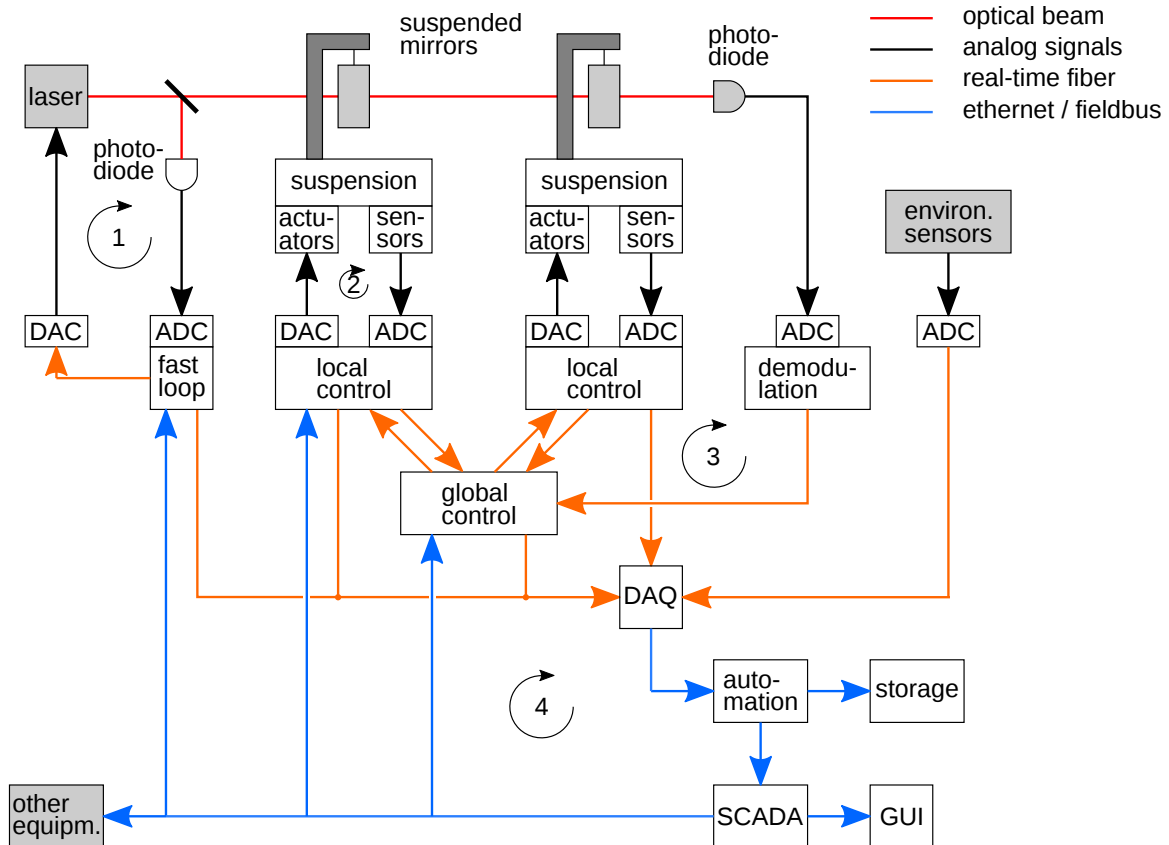


Figure 7.1: cartoon of the typical control of a GW interferometer. 4 types of loops can be recognized: 1) fast dedicated loops; 2) local control; 3) global control; 4) slow automation loops

From this, we can identify 4 types of control loops:

1. fast point-to-point loops: these are simple loops with a single input and single output (SISO) which have a control bandwidth up to 100 kHz, such as the power or frequency stabilization of the laser. These are typically implemented using analog electronics or, more recently, with fast digital loops running at a sample frequency up to 1 MHz.
2. local control: this is the control of a seismic isolation system that suspends a single mirror. As shown in Chapter 5, these are complex systems involving tens of sensors and actuators. This can be considered a multi-input multi-output (MIMO) control problem, which is limited to a small part of the experiment.
3. global control: The length of the cavity is determined by the distance between two separated mirrors, which can be read out using optical interferometry, and can be controlled by pushing against any of the mirrors. For controlling a complete interferometer, you need to control multiple distances, and thus multiple mirrors, by combining the signals of sensors spread around the experiment. This is thus a distributed MIMO control problem.
4. slow automation loops: At an even higher level, there is the need to switch various loops on or off, or slowly tweak e.g. a set-point of the faster loops, based on the state of the interferometer as a whole. This could either be done by a skilled operator who stares at some screens, or by an automation system. The latter typically implements loops at bandwidths of up to 100 mHz. This is typically implemented as a soft real-time system that is embedded in the DAQ-chain, which runs at a sample rate of 1 Hz and a latency of a few seconds.

These loops and other components will be explained in more detail in later sections. The same figure also shows how the signals of all control systems, as well as those from other parts such as environmental sensors, are collected by a data acquisition system (DAQ) for storage on disk.

7.3.2 Local control

The core optics of a GW interferometer are typically suspended by a seismic isolation system, to avoid that the large vibrations of the ground couple into movements of the mirror. This is achieved using a complex mechanical system involving pendula and mass-spring systems, see Chapter 5. This damping cannot be completely passive, since otherwise the mirrors would oscillate too much at the mechanical resonance frequencies. Additionally, since the mirrors are not firmly attached to the ground, but suspended by a very soft system, there is the need to fix the DC positions of the mirrors, especially in tip and tilt. Before any kind of interferometric measurements of the complete instrument can be done, active control is used to damp the resonances and pre-align the mirrors. This pre-damping of a single mirror is done using a large number (30-40) of sensors (LVDTs to measure position, optical levers to measure mirror tilt, seismometers to measure velocities, ...) that are located inside the corresponding suspensions. Feedback to the mirrors can be applied using many (10-20) voice-coil, PZT or electrostatic actuators. Since all of this is happening at the level of a single mirror suspension, it is known as *Local Control*.

Due to the large number of sensors, actuators and resonant modes of a mirror suspension, this is a Multi-Input, Multi-Output (MIMO) control problem, although in practice this can to a large extent be diagonalized by proper mechanical design. Such a system could be controlled at the level of a single rack, which contains all the analog transducers, ADCs, DACs and a controller. This control is *hard real-time* that typically runs at a sample frequency of 10-20 kHz, with a control bandwidth in the range of 5-100 Hz.

7.3.3 Global control

When operating the interferometer as a whole, the control of (some of) the mirrors and the laser is switched from local error signals that correspond to mirror positions with respect to the ground, to global error signals that correspond to cavity lengths formed by mirrors at separate locations. These error signals are obtained using laser interferometry, in which optical powers are converted to electrical signals using photodiodes and quadrant photodiodes, which are read out in DC or demodulated at RF frequencies, see the next section. Typical requirements of a global control system:

- Provide MIMO control. For the control of the longitudinal degrees of freedom (DOF) of a full double-recycled interferometer, this would imply a system with about 5 inputs and 8 outputs.
- Provide hard real-time at sample frequency up to 10-20 kHz, with control bandwidths up to 100 Hz.
- Allow distributed control, in which data is received from and sent to about 10 other systems
- Up to 50 internal signals of the various loops should be forwarded to the DAQ for monitoring.

Apart from longitudinal global control, there is also a need for global alignment control. The number of DOFs to control is much larger (around 16), but the bandwidth is typically slower (e.g. UGF of ~ 10 Hz, sample frequency 2 kHz).

7.3.4 Intermezzo: Photodiode demodulation

One of the main techniques for obtaining error signals to control GW interferometers is an optical heterodyne technique called Pound-Drever-Hall. In this scheme, the laser beam is sent through an Electro-Optic Modulator, which adds optical sidebands at RF frequencies. After reflecting the modulated beam off a Fabry Perot cavity, it is detected with a high bandwidth photodiode, whose signal is demodulated to obtain an error signal that can be used to lock a laser frequency to a cavity length or vice versa [59]. In a similar way, signals from quadrant photodiodes can be demodulated to obtain errors signals for the alignment of cavities [60].

In the past, the demodulation was done using analog mixers. At Virgo, the analog demodulation has recently been substituted by digital demodulation, which uses high-speed ADCs (400 MHz) to acquire the signal, and FPGAs and DSPs to demodulate and decimate the signals to 10 kHz. Although the commissioning of this system has cost a lot of time, the new system has shown great flexibility, and it seems clear that the future will be to go all-digital.

One of the noise sources in PDH comes from phase noise in the demodulation process, which leads to strict requirements on the generation and distribution of the local oscillator signal, and in case of digital demodulation, also on the timing system that synchronizes the ADCs. Three cases are compared in Fig. 7.2:

- A analog demodulation. This poses the lowest requirements on the timing of the ADCs, which can operate at the relatively low frequency used by Global Control, but it needs a low-noise distribution of the analog local oscillator signal. Some disadvantages of this method are the complex and inflexible analog electronics, and the pickup of RF noise on the long local oscillator cables.
- B Digital demodulation, by sending around the local oscillator. This requires small phase noise between the two ADCs that are located on the same PCB, but the global requirements on the timing are similar to the analog case. This scheme was used by Virgo's phase cameras.
- C Digital demodulation by fast sampling of both the local oscillator and the photodiode signal in separate locations. The differences in frequency between the signal generator and the demodulation frequency in the FPGA are sent around via a real-time communication network.

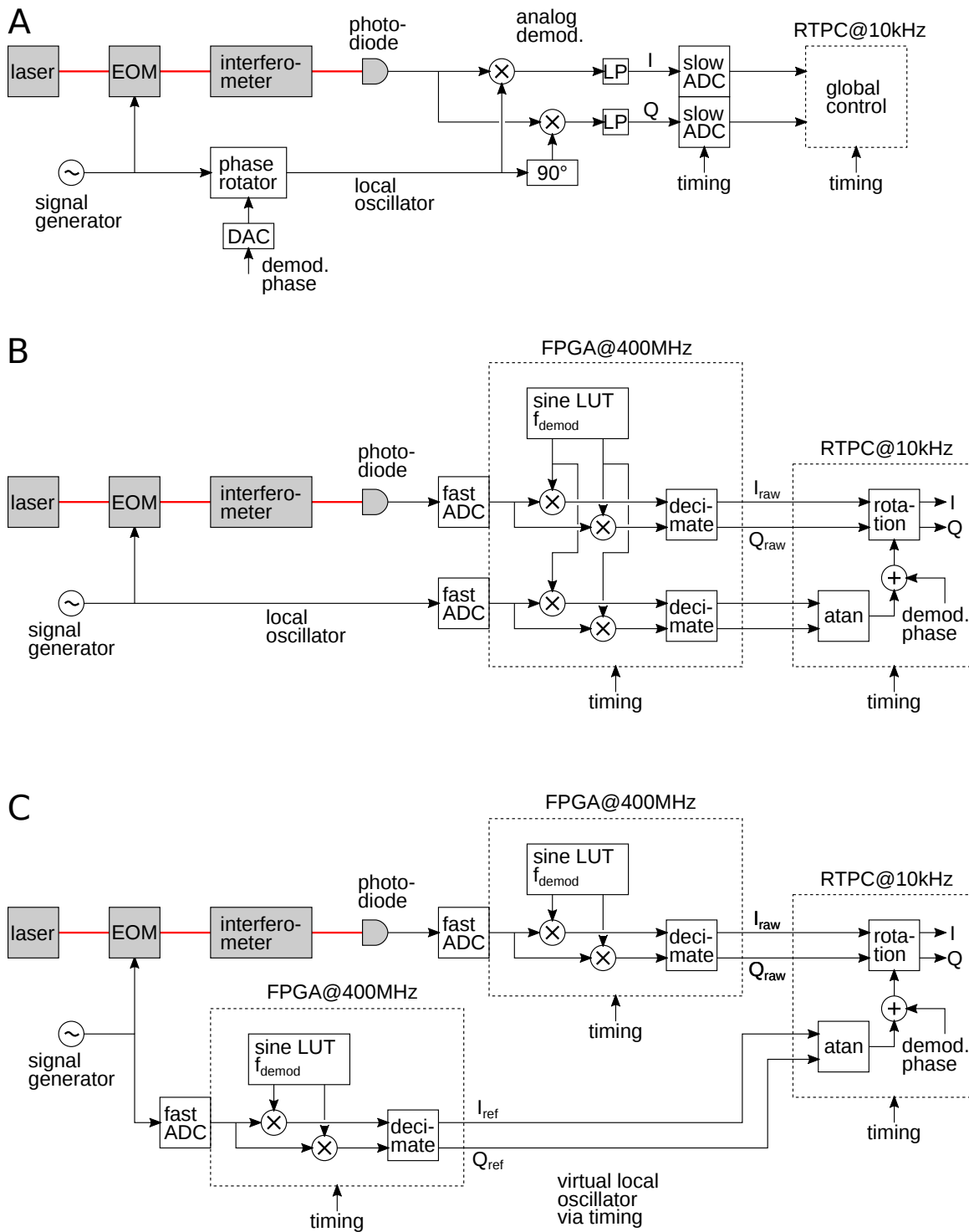


Figure 7.2: demodulation schemes: a) analog demodulation b) digital demodulation by sending around a LO c) digital demodulation by using the timing as a virtual local oscillator.

This means that timing system plays the role of a virtual local oscillator, and the requirements on the timing jitter of the timing system become as strict as requirements of a local oscillator. Not only the relative phase noise is important, but also the starting phase of sine used for the demodulation (which is given by the counter that drives the lookup table in the FPGA) should be perfectly synchronous between the separated systems, since this determines the DC demodulation phase.

We plan to use digital demodulation in the same way as at Virgo (so option C) wherever we can, but might still require analog demodulation for the 1 or 2 very fast loops.

7.3.5 Fast dedicated loops

A small number of the loops (e.g. fast laser frequency and amplitude control) do typically need a higher control bandwidth than 10-20 kHz. In the past, these were typically implemented using analog hardware, but also here a transition has started from analog to digital electronics. Since the photodiode demodulation will likely be all-digital, it seems inevitable that some of these loops are digital as well. Requirements:

- control bandwidth 10-100 kHz
- either analog or digital with sample frequency ~ 1 MHz
- simple SISO loop, either locally (within one rack), or a dedicated point-to-point low-latency digital communication channel (between two racks containing the sensor and actuator), to keep delays as low as possible.
- the error signal can be either a DC signal (e.g. a photodiode power in case of power stabilization) or a demodulated RF signal (e.g. in case of the lock of the Input Mode Cleaner).

7.3.6 Real-time communication

For global control of the interferometer, it is often necessary to use error signals that originate in one place of the instrument to actuate something that is physically far away. This calls for a real time communication network with very strict requirements:

- should be able to send and receive packages containing up to ~ 100 channels between the global control system, the various suspension controllers, the photodiode readout, the injection system and the DAQ system at rates of ~ 10 kHz.
- A small number of dedicated links will require sending of packets with < 10 channels point to point at rates of up to 1 MHz for the fast point-to-point loops described in section 7.3.5.
- since the real time communication is an integral part of the control loops, the propagation delay should be minimized to not limit the achievable bandwidth of the control. Ideally, the delay is just 1 sample, but a delay of up to a few samples might be tolerable for slower loops.
- for reasons of pickup of RF noise and galvanic separation, it is desirable to implement any communication channel that is longer than a few meters using fiber-optics, e.g. with standard SFP modules.

Compared to other experiments (e.g. in particle physics), the challenge is not so much the high data flux, but the low latency, high dynamic range and stringent distortion requirements .

7.3.7 Timing and local oscillator distribution

Gravitational Wave detection is a form of time-domain astronomy that tries to measure short transients to perform *multi-messenger astronomy*. Additionally, all the GW observatories around the world

are operated in a network, which allows to pinpoint a source in the sky using triangulation. These applications create a need for absolute timing with an accuracy at the microsecond level, which is readily achieved with clocks that are synchronized to a GPS receiver.

More critical are requirements on the relative timing between various parts within a single interferometer. Global control of the interferometer requires that real-time systems that are separated by distances up to several kilometers run perfectly in lock-step, with real-time messages arriving in a window that is a small fraction of the sample period. Additional demands come from the fast ADCs with a high number of bits, since a jitter in the sample time will translate to jitter in amplitude for high frequency signals. A special case of this is when digital demodulation of PDH signals is used, which can lead to coupling between signals that are in *quadrature* (typically one quadrature is used to control some degree of freedom, with the other quadrature is uncontrolled and can thus contain a large DC value).

Apart from the distribution of a time-stamp across the experiment, there is a need to generate and distribute one or more RF signals (typically 5-100 MHz) that are used for the PDH technique. The requirements on the phase noise of these signals are very strict. At Virgo the requirement is -120 dBc/Hz above 10 Hz, for a 10 MHz clock. ETpathfinder will likely need something similar.

7.3.8 Slow control and automation

Apart from the fast control loops described above, there is the need for very slow loops (up to 100 mHz bandwidth), such as for the stabilization of some temperature, or as part of cascaded schemes where the set-point of a fast inner loop is slowly moved by a slower outer loop. This is usually a form of *soft real-time control*, meaning that an occasional pause of the system should not have fatal consequences.

At Virgo, these loops are implemented using the PyALP application, which is embedded in the DAQ chain and thus has access to all fast channels in chunks of 1 second, and with a latency of about 2 second. Apart from slow control loops, this was also used for doing slow but complex calculations, such as generating the images of the phase camera or tracking the frequency of payload resonances.

Apart from these applications, which run continuously, there is a need for automation that can send sequences of commands and take decisions based on the state of the interferometer. This is performed using a hierarchical collection of state machines called Guardian [61] (or its Virgo derivative called Metatron). For both PyALP and Guardian, the user algorithm is implemented using Python.

These kind of automation systems typically need to read or modify parameters from all the faster loops. They also need to interact directly with the end user, via the form of graphical user interfaces and real-time plots. This is closely related to the functionality of a Supervisory Control and Data Acquisition system (SCADA) used in industrial control. We will evaluate if we can use any of the open source frameworks that implement such a system, such as EPICS and TANGO.

7.3.9 Safety systems

Apart from the control loops mentioned above, ETpathfinder will also need a different kind of control related to safety critical systems. Examples applications are laser safety (e.g. to switch off a laser if a door is opened), over-temperature protection (e.g. to switch off a laser in case of a chiller failure), the vacuum system (e.g. preventing the opening of a valve which has a non-zero pressure difference), and the cryo-pumps (which might be operated in a strictly timed sequence). These are typically implemented using robust hardware like programmable logic controllers (PLC). The exact

listed in text below:

- a loop to stabilize the length of the pre-mode-cleaner (PMC) on the laser frequency. This is sensed using a standard Pound-Drever-Hall (PDH) scheme using an electro-optical modulator EOM1 and an RF photodiode on its reflected beam (PMC_REFL). The length is actuated using a piezo (PZT) on the curved mirror of the cavity.
- the frequency of the master laser is locked on the Input Mode Cleaner (IMC), which is sensed using a standard PDH scheme using EOM2 and an RF photodiode on its reflected beam (IMC_REFL). The actuation on the laser frequency is divided between several actuators, ranging from the thermal control of the laser (ML_TH) at low frequencies, a PZT acting on the laser cavity at intermediate frequencies (ML_PZT), and, if necessary, on a broadband phase modulator (ML_PM) located directly downstream of the laser. The bandwidth of this loop might be so high that it is implemented using analog demodulation and an analog loop filter. When the interferometer is fully locked, the control of the common arm length (CARM) is added to the error point of this loop. It is still to be decided if some rigid cavity will be used for fixing the absolute frequency of the laser, which could potentially be acted upon using the ETMs.
- The alignment of the IMC, which is sensed using two RF quadrants in the near-field and far-field of its reflection (IMC_REFL). The actuators for this loop are the two steering mirrors located before the IMC, and the suspended mirrors of the IMC itself. The two flat mirrors of the IMC could potentially be connected rigidly to reduce the number of DOFs to control. Additional DC quadrants (e.g. after the IMC end mirror) might be needed.
- A loop to stabilize the overall power sent into the interferometer. This is sensed using a DC photodiode after the IMC, and is actuated by using an amplitude modulator (AM) located after the laser amplifier. This loop might have to be implemented using analog electronics.
- The global longitudinal control of the interferometer will control the 3 main DOFs of the interferometer: the common arm-length (CARM) of the two Fabry Perot cavities, the differential arm-length (DARM) and the difference in the two short paths between the beam-splitter (BS) and the input-test masses (ITMs), known as Michelson (MICH). These DOFs are sensed using 3 RF photodiodes (IFO_REFL, YARM_REFL and IFO_TRA) for which the in-vacuum EOM3 provides the sidebands, as well as the DC power after the Output Mode Cleaner (OMC_TRA). The exact sensing scheme is still to be developed based on simulations. These DOFs will be actuated upon via the laser frequency (CARM), the BS (MICH) and differentially on ETMX and ETMY (DARM).
- The global alignment of the interferometer is sensed using a combination of RF quadrant photodiodes that are placed in the near field and far field on the same beams as the 3 main RF photodiodes. Additionally, dithering techniques could be used for centering the beam on the mirrors. Additional DC quadrants might be needed. Actuation will be done on the two steering mirrors after the IMC, and on the main mirrors of the interferometer itself.
- The alignment of the OMC is sensed using two RF quadrants on its reflection (OMC_REFL) and acted upon using two steering mirrors before it.
- The length of the OMC is locked to the laser frequency, which is sensed either using a PDH technique or by dithering its length, and is acted upon using a PZT on one of its mirrors.

7.4 Implementation details

In this section, we will give a detailed list of all components that make up the control system, electronics and software of ETpathfinder, and estimate their costs.

7.4.1 Choice of control ecosystem

There are several ways to implement a control and data acquisition system that has the functionality described in the previous sections, ranging from fully commercial to custom solutions as implemented at LIGO or Virgo. The choice has a large implication, since different systems cannot be mixed freely. Committing to one system usually means being tied to a single provider for many years to come.

For ETpathfinder, we had a unique and timely opportunity to join the production run for additional control hardware built for the Advanced Virgo+ upgrade. This is a system built by the Virgo group from LAPP in Annecy. This system has several advantages:

- it has been tested for the last few years at Virgo, so it is known to be working
- it was built with GW interferometers in mind, so it has e.g. very high resolution ADCs and DACs, and digital demodulation hardware which does not exist commercially.
- the cost of the system basically consists of hardware costs with just a small overhead, with the added advantage of scale by combining with a large order for Virgo.
- it comes with a complete suite of free software and firmware. This will save many person-years of new development.
- commonality with Virgo hardware and software. This means that students and staff being trained at the ETpathfinder could easily work at Virgo, and vice versa.

Due to the limited time window to join this order, we did already chose to go for this solution before the completion of this report. Based on a preliminary channel count, we ordered the following components:

Description	Amount
DAQ box	43
Demodulation mezzanine	18
ADC2378 mezzanine	68
DAC1955 mezzanine	55
fast DAC mezzanine	10
TOLM-PCie	14
TDBox-v2	12
MuxDemux	5

The number of components already includes spares. Each DAQ box is able to host up to 4 mezzanines, the 'slow' ADC and DAC mezzanines each have 8 channels, the fast demodulation mezzanine has 4 channels, and the fast DAC 1 channel. This should provide enough channels to operate one complete interferometer in the first phase. Some off-the-shelf components will be needed to complete the real-time control system and the complete DAQ chain:

Description	Supplier	Amount
Real-time PCs	Dell or similar	13
Master GPS clock + antenna (10/100MHz, IRIG-B)	Microsemi	1
Networking equipment (routers, cabling, WIFI)	various	-
TOLM and ethernet fibers and SFP modules		60
Powerful PC for DAQ chain	Dell or similar	1
Storage server + disks	Dell or similar	1

7.4.2 Timing and local oscillator distribution

The timing system that synchronizes the whole control system (including the fast ADCs for the digital demodulation) is already included in the LAPP system. Although this system should in principle be adequate, it had and still has some issues:

- In the past, there were some issues with excess phase noise. Most of these have been resolved and at Virgo this is no longer limiting, but lowering the timing noise even further could e.g. relax the requirements on the DC value of out-of-loop signals that are in quadrature of error signals that are used for control loops
- The start of the counter that generates the sine generator in the FPGA of the demodulation board is not perfectly reproducible, which forces a retuning of all demodulation phases when a demodulation system is reset
- it requires manual calibration of propagation delays of long fibers

These issues could potentially be solved by changing to the White Rabbit (WR) timing system [62], which has been developed in the last years for CERN. Using WR was already considered to be used at Virgo in the long term. We plan to test this at the ETpathfinder. As a first step, an existing WR system could be adapted to serve as a drop-in replacement for the LAPP timing system, by generating exactly the same IRIG-B and 10/100 MHz signals as the old system. In a second step, it might be possible to incorporate the WR hardware directly in the DAQ boxes. Both steps will require a close collaboration with LAPP developers. We reserve some costs for testing the first step.

We also need stable frequency generators that are used to drive the EOMs that add the modulation sidebands to the optical beams. We plan on using the same generator that is used at Virgo. Some additional hardware is needed to distribute these signals between the EOMs and monitoring channels.

Description	Supplier	Amount
White Rabbit R & D	-	1
Low Noise Frequency Synthesizer (3 channel)	Spectradynamics	1
RF distribution and monitoring	EGO design?	3

7.4.3 Control and DAQ room

No people are allowed to be inside the experimental hall while doing sensitive experiments. This means that it should be possible to monitor and control everything from remote. Since a GW interferometer is a complex instrument with many parameters to monitor, this calls for a dedicated control room with a decent number of workstations and large screens. Some additional workstations might be needed to monitor parameters while working around the experimental rooms (2 inside the hall, 1 in the DAQ room, 1 in the pump room, 1 near the injection system).

Description	Supplier	Amount
Workstations	Dell or similar	10
Large displays	Dell or similar	3
Software licences	Mathworks and similar	-

7.4.4 Suspension transducers

Some electrical components that could be considered part of the suspensions have been moved into this WP:

Coil drivers basically a current amplifier that takes a standardized 10 V_{pp} input signal and converts it to a current that can be sent to actuation coils. This could be a direct copy of units built in the past.

LVDT readout modules: The seismic attenuators contain many position sensors that are implemented as Linear Variable Differential Transformers (LVDT). These are effectively transformers, of which the primary coil is driven by a high frequency (~ 10 kHz) signal, and the position is obtained by demodulating the signal picked up by the secondary coil. Previous modules employed analog demodulation. This design could be simplified by changing to digital demodulation, which has been successfully at Virgo using the LAPP electronics.

The total cost for all suspension electronics (LVDTs, coil drivers, stepper motors, commercial accelerometers) is estimated at 500 k€ incl. VAT.

7.4.5 Environmental probes and actuators

Apart from signals related to the interferometer itself, GW experiments typically acquire signals from a large number of environmental sensors. This is one area where a prototype can save with respect to an observatory, since they must be able to prove that a claimed signal is astrophysical signal and not environmental. Still, a limited number of (portable) probes are necessary for a prototype facility, since they are needed for noise hunting and can help in debugging other problems.

Several types of devices are needed:

- a small number of fixed and portable microphones, magnetometers, voltage/current 'sniffers' for on the power lines, and seismometers. These will need appropriate signal amplifiers, and fast ADC channels similar to the ones used in the suspension system. These could for example be helpful to discover that a certain line in a spectrum is caused by a noisy fan.
- a bigger number of ~ 1 Hz monitoring signals like temperatures and pressures, which are especially important for monitoring the cryogenic system. These can be implemented with off-the-shelf sensors and transducers, but will need integration with DAQ system. One example use is to find correlations between a drift of interferometer parameters with temperatures.
- a small number of actuators to inject high levels of environmental noise to characterize coupling paths, which is needed to make a noise projection. Examples are a loudspeaker, a big coil to inject magnetic fields and a shaker to vibrate parts of the setup to study coupling of scattered light noise. All of these will need dedicated amplifiers and some free DAC channels to generate arbitrary signals that are synchronous to the timing system.

We foresee the following components:

Description	Supplier	Quantity
Microphones (1 fixed for hall, 1 portable)	Brüel and Kjær	2
Nexus signal amplifier for microphones	Brüel and Kjær	1
Magnetic handheld probe	Stefan Mayer	1
TIRAVIB seismic shaker + power amplifier	Tira	1
Small PZT accelerometers	Meggitt	3
Magnetic coil	home built	1
Big loudspeaker + amplifier	home built	1
Voltage and current 'sniffers' on power line	home built	1
Seismometers	Trillium	3
Temperature sensors and transducers for cryogenics	-	60
Slow temperature, pressure, humidity sensors	-	1

7.4.6 Photodiodes and quadrant photodiodes

As shown in Fig. 7.3, we need a minimum of 5 RF photodiodes for the longitudinal control of one interferometer, in addition to one DC photodiode with a high quantum efficiency. Some additional DC photodiodes are needed for monitoring, but for these we could use cheap ones located outside of the vacuum. For the alignment, we need a pair (with different Gouy phases) of RF quadrant photodiodes in 5 locations around the interferometer, for a total of 10 items.

For the dark port, ETpathfinder requires photodiodes with a high quantum efficiency (HQE) and a large dynamic range, for laser wavelengths of 1550 nm and 2000 nm. For the non-HQE photodiodes at a wavelength of 1550 nm commercial InGaAs sensors will be considered. However, standard InGaAs sensors have a very low efficiency for a wavelength of 2000 nm and hence so called extended InGaAs sensors are required. A survey of commercially available extended InGaAs photodiodes showed that the devices exhibit a large flicker noise contribution [63]. Hence custom developed sensors with optimized quantum efficiency, especially for 2000 nm, might be needed; this development is not budgeted.

The PDs and QPDs will be on the benches inside the vacuum chamber, but in their own air-filled enclosure, similar to the QPDs that are used for Advanced Virgo.

Apart from the high QE photodiode, the main cost drivers are the vacuum tight enclosure and the base board which is special because cooling inside the air-box is challenging.

The overall costs of the photodiodes and quadrant photodiodes is then as follows:

Description	Quantity
PD 1550 nm	6
HQE PD 1550 nm	2
QPD 1550 nm	12
PD 2000 nm	6
HQE PD 2000 nm	2
QPD 2000 nm	12

7.4.7 Small suspensions

Apart from the 4 main mirror payloads of the ITMs and ETMs, additional actuated mirrors will be located on the two suspended benches. We need two versions of these, a single stage and double stage. These will each have 4 and 8 pairs of actuators and shadow sensors respectively, which are co-located

in a single unit called a Birmingham Optical Sensor and Electro-Magnetic actuator (BOSEM) [64]. Total cost for a single unit including in-vacuum part and readout electronics is about 2000 €.

For a single interferometer, we might need double stage suspensions for the beam-splitter and the 3 mirrors of the IMC. Single stage suspensions might be needed for the various steering mirrors. For mirrors that only need to be actuated occasionally, we could use vacuum compatible picomotors, which cost about 2500 € per mirror.

The exact number of the various small suspensions will depend on the detailed optical design. For now, we reserve a total of 300 k€ incl. VAT.

7.4.8 Beam monitoring cameras

A number of cameras will be needed that monitor the shape of the optical beams exiting the interferometer in various places. These are useful for (pre-)aligning the interferometer and for general monitoring of the system. In some cases, they can also be used to measure the position of a spot, so they can serve a role similar to a DC quadrant detector. Ideally, there are cameras on the beams in reflection and transmission of the PMC, IMC and OMC cavities, on the 3 main beams of the interferometer as well as the beam transmitted by both end mirrors, totaling 11 cameras per interferometer.

Standard CCD or CMOS cameras are not sensitive above a wavelength of 1100 nm. At 1550 nm, there is much less choice, but available technology includes phosphor-coated conventional chips (with models available at 2.5 k€), or InGaAs pixel detectors (which cost more than 10 k€). Availability of affordable cameras at 2 micron is still uncertain. Due to the thick cables, all of these can probably only be used outside of the vacuum. For now, we reserve 40 k€ incl. VAT.

7.4.9 Racks

The control electronics and other small transducers need to be mounted in standard 19 inch racks. To reduce the heat load on the clean room air conditioning, we intend to use water-cooled racks for all electronics that dissipates significant heat. We envision 2 of these per suspension tower, plus an additional 2 for the injection system. Additionally, we will need a number of open racks for other things that don't consume a lot of powers, like cable breakout boards, or for electronics that are located in areas outside of the cleanroom with their own air-conditioning (e.g. DAQ and pump rooms).

We foresee additional costs for the installation of mains cables to supply the racks and cable trays to route cabling around the hall. We also foresee some DC power supplies to power sensitive electronics in the hall. To reduce the heat load in the cleanroom, these can be located outside.

Description	Supplier	Amount
Water cooled rack (up to 10 kW cooling)	?	14
Open racks	?	10
Mains cabling and cable trays	?	-
Low noise DC power supplies	?	-

7.4.10 Cabling

The in-vacuum cabling for the suspensions for 2 complete interferometers was estimated as 300 k€. For in-air cabling (e.g. between ADCs/DACs and transducers, or between transducers and vacuum flanges), we reserve 50 k€.

7.5 Interfaces

The Control working package has interfaces with almost all the other working packages, since it deals with (some of) the electronics that are embedded in other systems, with the (digital) signals received from many sensors and sent to many actuators, and will take care of the overall acquisition of all signals.

Infrastructure/cleanroom: the main interface with infrastructure is related to the need for rack space, electrical power and cooling capacity. The control of environmental parameters like temperature and humidity is considered part of the infrastructure/cleanroom itself, but some slow signals to monitor these systems will have to be acquired and stored.

Vacuum and cryogenics: many control systems related to the vacuum and cryogenics systems are safety critical and tightly integrated with those systems, so their implementation belongs in that WP itself. There will however be the need to acquire many slow signals to monitor the correct operation of these systems (e.g. track the cool-down of mirrors over timescales of weeks).

Seismic isolation: the control WP will take care of the digital electronics for controlling the seismic isolation systems, as well as the electronic transducers for various sensors and actuators.

Optics: the control system will use the signals from the various photodiodes and quadrants as error signals for the global control of the interferometer, and will connect to various sensors/actuators of the laser/injection system. The control WP is also responsible for developing various optical sensors (photodiodes, quadrants, cameras).

7.6 Planning and Work Break Down structure

The exact planning of this work package and the work break down structure is still to be worked out. There still is some time to do this, since first parts of the control system will only have to become operational once the first parts of the mirror suspensions are ready to be commissioned. Before that time, we plan on doing stand-alone tests with the control hardware, and will set up the complete software chain.

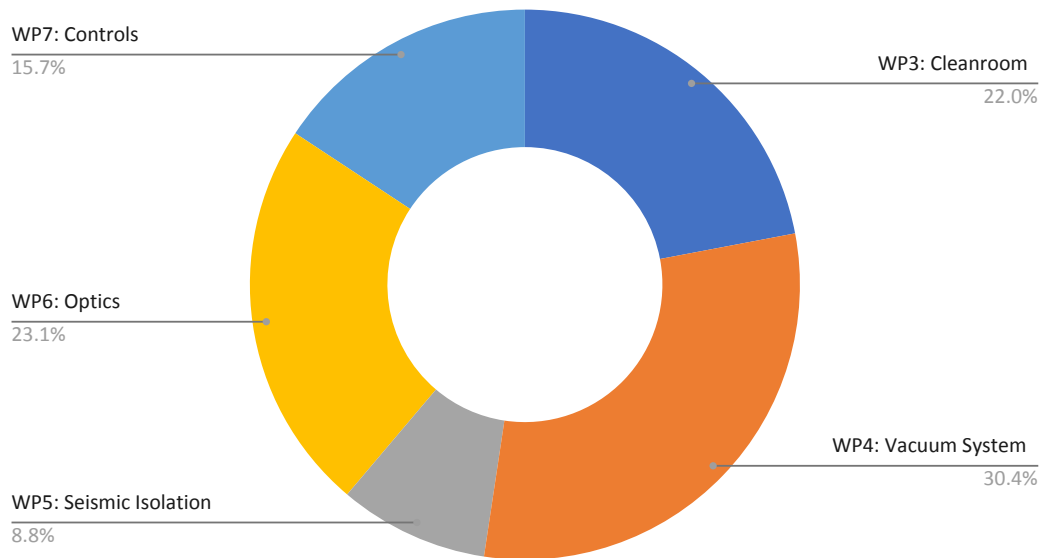


8. Budget Summary

The overall equipment budget of the ETpathfinder phase 1a/b project is composed of the individual budgets of work packages WP3 to WP7 as follows. We additionally list a budget contingency of 10%, which is foreseen to cover unexpected expenses, especially for items that have to go through a tendering process and thus precise costings cannot be given in advance.

Work Package	Budget in €, incl VAT	Budget in €, excl VAT
WP3: Cleanroom	3 250 000	2 685 950
WP4: Vacuum System	4 481 840	3 704 000
WP5: Seismic Isolation	1 300 000	1 074 380
WP6: Optics	3 408 320	2 816 793
WP7: Controls	2 321 108	1 918 271
Subtotal	14 761 268	12 199 395
Contingency 10%	1 476 127	1 219 940
Total	16 237 394	13 419 335

The subtotal without contingency (14.76 MEuro) matches pretty well the earlier cost estimates of the proposal (14.50 MEuro) and we assume the deviation of less than 2 % is well within the noise of the accuracy of our knowledge of the costs and hence no cause for major concern. However, the Interreg grant did not consider any contingency. If an contingency is found to be necessary, additional funds have to be found.

BUDGET (incl. VAT)

In order to operate the circuit and using the unit. Failure to



- This circuit has the possibility of high voltage. Operate with caution that live parts are exposed. Use only qualified personnel. Before connecting and all in the circuit, check the polarity immediately.
- Operate with caution that live parts are exposed.
 - Use only qualified personnel.
 - Before connecting and all in the circuit, check the polarity immediately.



- This circuit has hot surfaces. Do not touch the hot surfaces. Give the unit time to cool down before touching.
- Do not touch the hot surfaces.
 - Give the unit time to cool down before touching.



This circuit has high voltage and qualified personnel are required for safety reasons.



The unit does not operate without reading the *Manual*.

9. Health and Safety

9.1 Health and Safety Overview for ETpathfinder

Occupational Health and Safety is obviously a vital element of any project and it needs to be considered already during the design phase of the critical aspects, like the vacuum system, cryogenics, laser safety, lifting of heavy objects. etc.

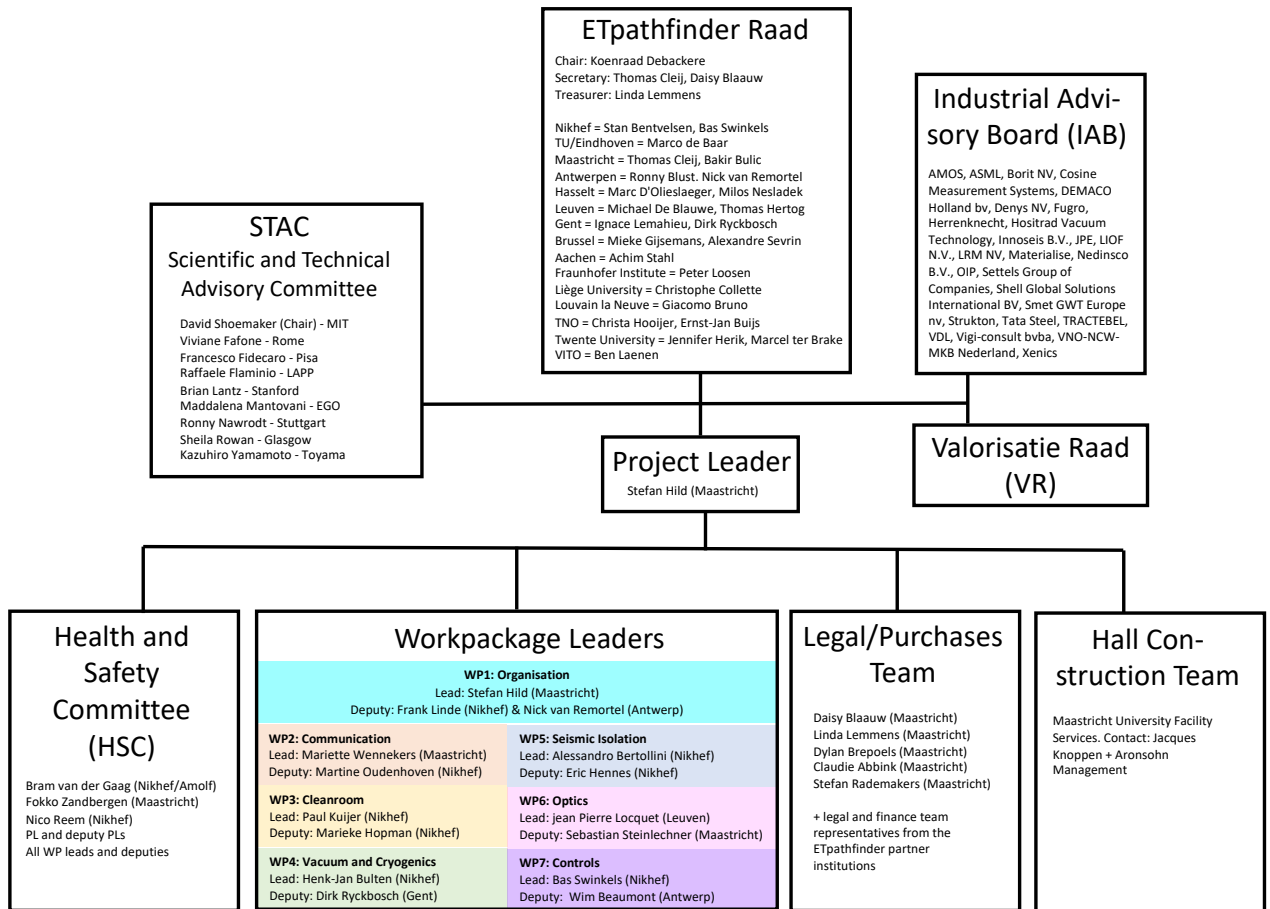
Within ETpathfinder we have agreed to follow the usual hierarchy of occupational health and safety control:

- **Source measures:** An employer must first remove the cause of the problem. Example: replace harmful substance for a safer alternative.
- **Collective measures:** If source measures do not offer possibilities, the employer must take collective measures to reduce risks. Example: placing a screen or a suction system.
- **Individual measures:** If collective measures cannot or do not (yet) offer a satisfactory solution, the employer must take individual measures. Example: organize the work in such a way that employees run less risk (task rotation).
- **Personal protective equipment** If the top three measures have no effect, the employer must provide the employee with personal protective equipment free of charge. Example: ear protectors and welding goggles.

In the first health and safety workshop on ETpathfinder it was decided to establish a ETpathfinder Health and Safety committee (HSC), including members with professional background in health and safety (mainly from Nikhef and Maastricht University) as well as a representative from each workpackage.

The ETpathfinder team will bring any health and safety related issues to the attention of the HSC. After detailed consideration (with input from the relevant workpackages) the HSC will provide written recommendation to the project leadership for consideration. Written responses including decision taken and reasoning will be provided to HSC by the project leadership.

10. Organisational Overview of Etpathfinder





Bibliography

- [1] S. Whitcomb and M. Zucker, "Measurement of Optical Path Fluctuations due to Residual Gas in the LIGO 40 Meter Interferometer," *Proceedings of the the Seventh Marcel Grossman Meeting on General Relativity, July 1994, Stanford University*, pp. 1434–1436, 1994.
- [2] A. Cavalleri and *et al.*, "Increased Brownian Force Noise from Molecular Impacts in a Constrained Volume," *Phys. Rev. Lett.*, vol. 103, pp. 140601–4, 2009.
- [3] A. Cavalleri and *et al.*, "Gas damping force noise on a macroscopic test body in an infinite gas reservoir," *Physics Letters A*, vol. 374, pp. 3365–3374, 2010.
- [4] F. Acernese, *et al.*, and "Einstein Telescope Science Team", "Einstein gravitational wave Telescope Conceptual Design Study," "https://tds.virgo-gw.eu/?call_file=ET-0106C-10.pdf", 2011.
- [5] t. LIGO collaboration, *LIGO TDS*, vol. 040001-00-D, 1994.
- [6] J. F. O'Hanlon, *A users guide to vacuum technology*, John Wiley and sons, 2005.
- [7] M. Ortina, "STICKING COEFFICIENTS FOR TECHNICAL MATERIALS IN VACUUM TECHNOLOGY, (CERN thesis)," "<https://www.politesi.polimi.it/bitstream/10589/131905/1/MattiaOrtinoMasterThesis.pdf>", 2016.
- [8] Y. Tuzi and *et al.*, *Vacuum*, vol. 47, pp. 705–708, 1996.
- [9] K. Hasegawa and *et al.*, "Molecular adsorbed layer formation on cooled mirrors and its impacts on cryogenic gravitational wave telescopes," *Phys. Rev. D*, vol. 99, p. 022003, 2019.
- [10] theVirgo Collaboration, "AdV VAC FDR," "https://workarea.ego-gw.it/ego2/virgo/advanced-virgo/vac/cryotrap/fdr-cryotrap-jun2010/AdV__FDR_VAC_rev12.pdf", 2010.

- [11] T. Akutsu and *et al.*, *Clas. Quan. Grav.*, vol. 36, p. 165008, 2019.
- [12] T. Ushiba and *et al.*, “Development of cryogenic system in KAGRA,” vol. workshop on gravitational wave activities in Taiwan, 2015.
- [13] T. Tomaru and *et al.*, *Cryocoolers*, vol. 13, pp. 695–702, 2005.
- [14] C. Tokoku and *et al.*, *AIP Conf. Proc.*, vol. 1573, p. 1254, 2014.
- [15] Y. Sakabibara and *et al.*, “Progress on the cryogenic system for the KAGRA cryogenic interferometric gravitational wave telescope,” *Clas. Quan. Grav.*, vol. 31, p. 224003, 2014.
- [16] H. F. Burger and *et al.*, *AIP conf. proc.*, vol. 985, p. 1613, 2008.
- [17] Y. Wu and *et al.*, *Cryocoolers*, vol. 17, p. 377, 2012.
- [18] Y. Wu and *et al.*, *Physics Procedia*, vol. 67, p. 411, 2015.
- [19] H. J. M. ter Brake and *et al.*, “Sorption Cooling,” *5th Einstein Telescope Symposium, Oct 2013, Hannover*.
- [20] N. Tzabar and H. J. M. ter Brake, *Adsorption*, vol. 24, pp. 325–332, 2018.
- [21] J. Peterson, “Observation and modeling of seismic background noise,” *U.S. Geol. Surv. Open-file Rept.*, vol. 93–322.
- [22] T. Accadia, “The seismic Superattenuators of the Virgo Gravitational Waves Interferometer,” *Journal of Low frequency noise, vibration and active control*, vol. 30.
- [23] T. Sekiguchi, “Study of a low frequency vibration isolation system for large–scale gravitational waves detectors,” *PhD Thesis*.
- [24] K. Venkateswara, “A high–precision mechanical absolute–rotation sensor,” *Rev.Sci. Instrum.*, vol. 85 (1), p. 015005, 2014.
- [25] M. Bantel and R. Newman, “High precision measurement of torsion fiber internal friction at cryogenic temperatures,” *J.Alloys Comp.*, vol. 310.
- [26] E. Y.S.Touloukian, R.K.Kirby and T.Y.R.Lee, *Thermophysical Properties of Matter—the TPRC Data Series*, IFI/Plenum, New York, 1970.
- [27] A. Inyushkin, “Ultrahigh thermal conductivity of isotopically enriched silicon,” *J.App.Phys.*, vol. 123.
- [28] C.Kittel, *Introduction to Solid State Physics*, John Wiley & Sons, Inc., New York, 6th edn., 1986.
- [29] J. Van Heijningen, “A multistage vibration isolation system for Advanced Virgo suspended optical benches,” *Class.Quantum Grav.*, vol. 36 (7), p. 075007, 2019.
- [30] R. Schnabel *et al.*, “Building blocks for future detectors: Silicon test masses and 1550 nm laser light,” *Journal of Physics: Conference Series*, vol. 228, p. 012029, 2010.

-
- [31] S. Rowan et al., “Test mass materials for a new generation of gravitational wave detectors,” in P. Saulson and A. M. Cruise, eds., “Gravitational-Wave Detection,” vol. 4856, pp. 292 – 297, International Society for Optics and Photonics, SPIE, 2003.
- [32] M. J. Keevers and M. A. Green, “Absorption edge of silicon from solar cell spectral response measurements,” *Applied Physics Letters*, vol. 66 (2), pp. 174–176, 1995.
- [33] J. Degallaix et al., “Bulk optical absorption of high resistivity silicon at 1550 nm,” *Opt. Lett.*, vol. 38 (12), pp. 2047–2049, 2013.
- [34] Anshot Markosyan, Angus Bell, “Optical properties of a float-zone rectified and Czochralski grown in a steady magnetic field crystalline Si,” dcc.ligo.org/LIGO-G1700480, 2017.
- [35] A. V. Cumming et al., “Silicon mirror suspensions for gravitational wave detectors,” *Classical and Quantum Gravity*, vol. 31 (2), p. 025017, 2013.
- [36] A. Bell.
- [37] A. Khalaidovski, J. Steinlechner, and R. Schnabel, “Indication for dominating surface absorption in crystalline silicon test masses at 1550 nm,” *Classical and Quantum Gravity*, vol. 30 (16), p. 165001, 2013.
- [38] A. S. Bell et al., “Anomalous optical surface absorption in nominally pure silicon samples at 1550 nm,” *Classical and Quantum Gravity*, vol. 34 (20), p. 205013, 2017.
- [39] R. Nawrodt et al., “High mechanical Q-factor measurements on silicon bulk samples,” *Journal of Physics: Conference Series*, vol. 122, p. 012008, 2008.
- [40] C. Krüger et al., “Birefringence measurements on crystalline silicon,” *Classical and Quantum Gravity*, vol. 33 (1), p. 015012, 2015.
- [41] R. Birney et al., “Amorphous Silicon with Extremely Low Absorption: Beating Thermal Noise in Gravitational Astronomy,” *Phys. Rev. Lett.*, vol. 121, p. 191101, 2018.
- [42] H.-W. Pan et al., “Silicon nitride and silica quarter-wave stacks for low-thermal-noise mirror coatings,” *Phys. Rev. D*, vol. 98, p. 102001, 2018.
- [43] A. Amato et al., “High-Reflection Coatings for Gravitational-Wave Detectors: State of The Art and Future Developments,” *Journal of Physics: Conference Series*, vol. 957, p. 012006, 2018.
- [44] K. Craig et al., “Mirror coating solution for the cryogenic Einstein Telescope,” *Physical Review Letters*, 2019.
- [45] R. Flaminio et al., “A study of coating mechanical and optical losses in view of reducing mirror thermal noise in gravitational wave detectors,” *Classical and Quantum Gravity*, vol. 27 (8), p. 084030, 2010.
- [46] H.-W. Pan et al., “Thickness-dependent crystallization on thermal anneal for titania/silica nm-layer composites deposited by ion beam sputter method,” *Opt. Express*, vol. 22 (24), pp. 29847–29854, 2014.

- [47] M. Magnozzi et al., “Optical properties of amorphous SiO₂-TiO₂ multi-nanolayered coatings for 1064-nm mirror technology,” *Optical Materials*, vol. 75, pp. 94 – 101, 2018.
- [48] J. Steinlechner et al., “Thermal noise reduction and absorption optimization via multimaterial coatings,” *Phys. Rev. D*, vol. 91, p. 042001, 2015.
- [49] W. Yam, S. Gras, and M. Evans, “Multimaterial coatings with reduced thermal noise,” *Phys. Rev. D*, vol. 91, p. 042002, 2015.
- [50] G. D. Cole et al., “High-performance near- and mid-infrared crystalline coatings,” *Optica*, vol. 3 (6), pp. 647–656, 2016.
- [51] L. Pinard et al., “Mirrors used in the LIGO interferometers for first detection of gravitational waves,” *Appl. Opt.*, vol. 56 (4), pp. C11–C15, 2017.
- [52] P. K. et al., “in preparation,” 2019.
- [53] J. Locquet et al., “Doubling the critical temperature of La_{1.9}Sr_{0.1}CuO₄ using epitaxial strain,” *NATURE*, vol. 394 (6692), pp. 453–456, 1998.
- [54] Z. Rittersma et al., “Characterization of field-effect transistors with La₂Hf₂O₇ and HfO₂ gate dielectric layers deposited by molecular-beam epitaxy,” *JOURNAL OF APPLIED PHYSICS*, vol. 99 (2), 2006.
- [55] G. Norga et al., “Phase of reflection high-energy electron diffraction oscillations during (Ba,Sr)O epitaxy on Si(100): A marker of Sr barrier integrity,” *APPLIED PHYSICS LETTERS*, vol. 87 (26), 2005.
- [56] G. Norga et al., “Solid phase epitaxy of SrTiO₃ on (Ba,Sr)O/Si(100): The relationship between oxygen stoichiometry and interface stability,” *JOURNAL OF APPLIED PHYSICS*, vol. 99 (8), 2006.
- [57] C. Marchiori et al., “Thermal stability of the SrTiO₃/(Ba,Sr)O stacks epitaxially grown on Si,” *APPLIED PHYSICS LETTERS*, vol. 88 (7), 2006.
- [58] C. Rossel et al., “Field-effect transistors with SrHfO₃ as gate oxide,” *APPLIED PHYSICS LETTERS*, vol. 89 (5), 2006.
- [59] E. D. Black, “An introduction to Pound–Drever–Hall laser frequency stabilization,” *American Journal of Physics*, vol. 69 (1), pp. 79–87, 2001.
- [60] E. Morrison, B. J. Meers, D. I. Robertson, and H. Ward, “Automatic alignment of optical interferometers,” *Appl. Opt.*, vol. 33 (22), pp. 5041–5049, 1994.
- [61] J. G. Rollins, “Distributed state machine supervision for long-baseline gravitational-wave detectors,” *Review of Scientific Instruments*, vol. 87 (9), p. 094502, 2016.
- [62] M. Lipiński, T. Włostowski, J. Serrano, and P. Alvarez, “White rabbit: a PTP application for robust sub-nanosecond synchronization,” in “2011 IEEE International Symposium on Precision Clock Synchronization for Measurement, Control and Communication,” pp. 25–30, 2011.

-
- [63] J. Briggs et al., “Using Extended InGaAs Photodiodes for the Detection of Gravitational Waves,” ["https://dcc.ligo.org/LIGO-P1900325"](https://dcc.ligo.org/LIGO-P1900325), 2019.
- [64] L. Carbone et al., “Sensors and actuators for the Advanced LIGO mirror suspensions,” *Classical and Quantum Gravity*, vol. 29 (11), p. 115005, 2012.



Nomenclature

Abbreviations

AAS	Atomic Absorption Spectroscopy
ADC	Analog-to-Digital Converter
AR	Anti-Reflecting
BS	Beam Splitter
CARM	Common length of arm cavities
CARM	Common Mode Arm Length
CF	ConFlat standard flanges
CH	Carbohydrates
CPU	Central Processing Unit
CTE	Coefficient of Thermal Expansion
CZ	Czochralski
DAC	Digital-to-Analog Converter
DAQ	Data Acquisition
DARM	Differential Arm Length
DLC	Diamond-like Carbon
DOF	Degree(s) Of Freedom

DSP	Digital-Signal Processor
ECR	Electron Cyclotron Resonance
EDM	Electrical Discharge Machining
EIES	Electron Impact Emission
EOM	Electro-Optic Modulator
ET	Einstein Telescope
ETM	End Test Mass
FEM	Finite Element Analysis
FFT	Fast Fourier Transform
FI	Faraday Isolator
FP	Folded Pendulum
FPGA	Field-Programmable Gate Array
FS	Fused Silica
FS	Fused Silica
FTE	Full time equivalent
FZ	Float Zone
FZ-Si	Float Zone crystalline silicon
GAS	Geometric Anti-Spring
GWD	Gravitational Wave Detector
GW	Gravitational Wave
HCB	Hydroxide Catalysis Bonding
He	Helium
HR	Highly-Reflecting
IBAD	Ion Beam-Assisted Deposition
IBS	Ion Beam Sputtering
IFO	Interferometer
IMC	Input Mode Cleaner
IO	Input Optics

IO	Input/Output
IP	Inverted Pendulum
IR	Infrared
ISO	International Organization for Standardization
ITM	Input Test Mass
LAXS	Low angle X-ray Spectroscopy
KAGRA	Kamioka Gravitational wave detector
LIGO	Laser Interferometer Gravitational wave Observatory
LN2	Liquid Nitrogen
LVDT	Linear Variable Differential Transformer
MBE	Molecular Beam Epitaxy
MFC	Mass Flow Controller
MICH	Michelson short arm length
FPMI	Fabry-Perot Michelson Interferometer
MI	Michelson Interferometer
MIMO	Multiple-Input, Multiple-Output
MLI	Multi-Layer Isolation
MultiSAS	Multistage seismic attenuation system
NPRO	Non-Planar Ring Oscillator
NTE	Negative Thermal Expansion Coefficient
OMC	Output Mode Cleaner
OPA	Optical Parametric Amplification
OPL	Optical Path Length
PCB	Printed Circuit Board
PLC	Programmable Logic controllers
PLC	Programmable Logic Controller
PMC	Pre-mode cleaner
ppm	Parts per million

PRCL	Power Recycling Cavity Length
PRC	Power Recycling Cavity
PRM	Power Recycling Mirror
PR	Power Recycling
PSD	Power Spectral Density and Position Sensitive Device [seen in 5.4.2]
PSL	Prestabilized Laser
PTE	Positive Thermal Expansion Coefficient
PT	Pulse Tube cryogenic refrigerator
PZT	Piezoelectric Transducer
QMS	Quadrupole Mass Spectroscopy
QND	Quantum Non-Demolition
R&D	Research and Development
RF	Radio Frequency
RHEED	Reflection High-Energy Electron Diffraction
RIN	Relative Intensity Noise
ROC	Radius Of Curvature
RTA	Rapid Thermal Annealing
RTPC	Real Time Parameter Controller
SE	Spectroscopic Ellipsometry
SFP	Small Form-factor Pluggable
SISO	Single Input, Single Output
SmCo	Samarium-Cobalt
SNR	Signal to Noise Ratio
SQL	Standard Quantum Limit
SRCL	Signal Recycling Cavity Length
SRC	Signal Recycling Cavity
SR	Signal Recycling
TEM	Transverse Electromagnetic

TE	Thermo-Elastic
TPA	Two-Photon Absorption
UHV	Ultra-high vacuum
VAT	Value Added Tax

Symbols

Please note that some symbols might stand for more than one quantity depending on the context

A	Effective area of the mirror [used in 4.2.1] and cross-sectional area [used in 4.3.5]
c	Speed of light
c_{11}	Elastic Stiffness Coefficient
D	Mirror Dimension
d	Coating Thickness [used in 6.4.2], Viton ring thickness [used in 4.3.2] and aperture diameter [used in 4.3.3]
E	Young-modulus of blade spring material
E_b	Binding Energy per molecule
f	Wave frequency
f_{res}	Resonance frequency
g	Gravitational acceleration
h	Mirror Thickness
i	Imaginary unit
J	Impingement rate and Joules as S.I unit
k	Heat conductivity coefficient and flexure cumulative stiffness [used in 5.2.1]
k_b	Boltzmann constant
L	Geometric length
l	Geometrical length
λ	Wavelength
Φ_{sub}	Substrate mechanical loss

m	Mass of the particle [used in 4.2.1] and pendulum load [used in 5.2.1]
N	Number of gas molecules
P	Laser Power
P_{in}	Input cooling power
Q	Leaking rate [used in 4.3.2], thermal energy [used in 4.3.3] and mechanical quality factor [used in 5.4.1]
R	Mirror Radius
ρ	Density of gas unit [used in 4.2.1], material density [used in 6.5.1]
S_f	Amplitude spectral density
$\langle v \rangle$	Mean molecular speed
V	Volume of gas [used in 4.2.1] and Variance
v	Sound Velocity
w	Radius of laser beam on mirror coating
Z_m	Mechanical Impedance